Supercontinuum Generation by Chirped Pulse Compression for Ultrafast Spectroscopy and Broadband Near-field Microscopy

Thomas Ganz

Dissertation
an der Fakultät für Physik
der Ludwig–Maximilians–Universität
München

vorgelegt von
Thomas Ganz
aus Basel

München 27. Juli 2011

Contents

Zusammenfassung

Schon seit längerer Zeit versucht man auf dem Gebiet der Optik mit ultrakurzen Pulsen die gängigen Hz und kHz Wiederholungsraten Experimente auf MHz zu bringen. Dabei würde man von einem stark verbesserten Signal-zu-Rausch-Verhältnis wie auch von einer reduzierten Messzeit profitieren. Sofortige Anwendungen finden sich in der ultraschnellen Spektroskopie, der Erzeugung höherer Harmonischen wie auch in der Materialbearbeitung. Zurzeit gibt es aber keine zufriedenstellende Lasersysteme mit MHz Wiederholungsrate für diese Experimente. Die bisherigen Aufbauten sind entweder zu komplex und zu instabil, oder die Ausgangspulse sind zu lang. Im letzteren Falle könnte man mit einer Pulskomprimierungstechnik basierend auf optischen Fasern und dem nichtlinearen Prozess der Selbstphasenmodulation kurze Pulse erzeugen, doch der nichtlineare Prozess der Selbstfokussierung beschränkt die maximale Energie, welche man in die Fasern einkoppeln kann, auf einen Bruchteil der vorhandenen.

Mit der hier entwickelten Methode der ”Pulskompression mit linear frequenzmodulierten Eingangspulsen”, sprich verlängerten Eingangspulsen, konnten wir diese Beschränkung umgehen. Zur Demonstration benützten wir einen energiereichen Ti:Saphir Oszillator auf 5MHz Wiederholungsrate mit 400nJ und 55fs Eingangspulsen. Mit unserer Methode erzeugten wir vierfach verkürzte Pulse (15fs) mit 350nJ Ausgangsenergie. Dies entspricht etwa einer vierfach höheren Ausgangsenergie verglichen mit der bisherigen Pulskomprimierungstechnik. Wir untersuchten auch den Transfer der linearen Frequenzmodulation des Eingangspulses zum Ausgangspulses nach der spektralen Verbreiterung, und entdeckten dabei, ein überraschendes Verhältnis der beiden Frequenzmodulationen zueinander. Der Einfluss der Frequenzmodulation ist anscheinend grösser, als man in simplen Modellen angenommen hat. Unsere Methode ist nicht beschränkt auf ein spezielles Lasersystem und kann auf eine Vielzahl von Komprimierungstechniken, die auf Selbstphasenmodulation basieren, angewendet werden. Der experimentelle Aufbau ist einfach, kompakt und stellt dank seiner hervorragenden Stabilität und Benutzerfreundlichkeit eine interessante Möglichkeit für viele Forschungsgruppen dar. Weiterhin demonstrierten wir Pulskompressionsexperimente mit einer Komprimierung bis in den Bereich weniger Schwingungzyklen des Pulses (6fs), wie auch die Komprimierung mit Eingangsleistungen von über 100W, beziehungsweise Pulsenenergien grösser als 2μJ. Dabei stellten wir fest, dass thermische Effekte noch keine limitierende Rolle spielen. Für die Komprimierung der Pulse untersuchten wir zum ersten Mal systematisch die verwendeten Breitbandkomprimierungsspiegel und stellten dabei fest, dass jeder Spiegel eine unterschiedliche spektrale Verschiebung der Gruppenverzögerungsdispersion aufweist. Wir empfehlen nachdrücklich jeden einzelnen Spiegel zu vermessen damit man die geeigneten Spiegel für die Kompression selektieren kann.

In einem zweiten Teil meiner Thesis untersuchten wir das Thema der Breitbandnahfeldmikroskopie. Wir entwickelten dabei eine Methode, mit der die Nahfeldmikroskopie nicht

mehr nur einzelne Wellenlängen nacheinander messen kann, sondern ein durchgehendes Spektrum während einem Messvorgang aufzuzeichnen vermag. Dadurch verkürzt sich die Messzeit und verringert sich auch die Anzahl der Messartefakten. Vorallem aber hat sich das Nahfeldmikroskop damit zu einem vollwertigen spektroskopischen Gerät für die Nanowissenschaften weiterentwickelt. Wir demonstrieren erstmals kontinuierliche Nahfeld-Breitbandspektren im mittel-infraroten Spektralbereich von Gold und Siliziumkarbid, gemessen in Amplitude und Phase.

Abstract

For a long time the ultrafast optics community desires to rise their experiments at Hz or kHz repetition rates to the MHz scale to benefit from the increased signal-to-noise ratio, total flux and reduced measurement time. Immediate applications can be found in ultrafast spectroscopy, high harmonic generation or material processing. But currently no satisfying laser-system at MHz repetition rates exists. Either they are very complex and unstable or the output pulses are too long. In the later case one could use a pulse compression technique based on self-phase modulation in fibers to achieve shorter pulses but due to the nonlinear process of self-focusing the energy coupled into the fiber will be limited to only a fraction of the available one as the fiber gets damaged.

We have overcome this essential limitation by the here developed and demonstrated concept of chirped pulse compression. Using a commercial long-cavity Ti:sapphire oscillator with 55fs, 400nJ pulses at 5MHz, we generated 15fs and 350nJ pulses. This is a factor of four more energy than possible with current pulse compression techniques using fibers. Investigating the chirp transfer between the input and the output chirp after the fiber, respectively after spectral broadening, we discovered a surprising chirp transfer ratio which revealed clearly a more significant influence of the chirp than assumed to date. The chirped pulse compression concept is not limited to a special laser-system and can be transferred to any pulse compression method using self-phase modulation. Our setup is simple and compact. It represents an interesting option for many research groups due to its excellent stability properties and user-friendliness. We also demonstrated pulse compression into the few-cycle regime (6fs). Additionally, we used high-average power ($>$100W) and higher energy ($>2\mu$J) laser systems and showed that thermal aspects do not represent a fundamental limitation. For proper pulse compression we systematically analyzed for the first time our broadband chirped mirrors and found a different spectral group delay dispersion shift on each mirror. We therefore recommend emphatically to measure each chirped mirror to find the correct chirped mirrors which allows successful compression.

In a second part of my thesis we investigated the subject of continuous broadband near-field microscopy. Thereby we developed a method for recording continuous spectra in one measurement run instead of recording several different wavelengths after each other. Thus, we did not only decreased the measurement time and with it the amount of measurement artefact, but also raised the near-field microscopy to a true spectroscopic tool for nanoscience. We demonstrate continuous mid-infrared near-field spectra in amplitude and phase of gold and silicon carbide.

Publications

T. Ganz, V.Pervak, A. Apolonski and P. Baum
16-fs, 350-nJ pulses at 5 MHz repetition rate delivered by chirped pulse compression in fibers
Optic Letters, Vol. 36, Issue 7, pp. 1107-1109 (2011)

S. Amarie, **T. Ganz** and F. Keilmann
Mid-infrared near-field spectroscopy
Optics Express, Vol. 17, Issue 24, pp. 21794-21801 (2009)

T. Ganz, M. Brehm, H.G. von Ribbeck, D.W. van der Weide, and F. Keilmann
Vector frequency-comb Fourier-transform spectroscopy for characterizing metamaterials
New Journal of Physics 10 123007
Awarded as "Best of 2008" in the section of optics and imaging of NJP

T. Ganz, H.G. von Ribbeck, M. Brehm and F. Keilmann
Compact frequency-comb Fourier-transform infrared spectrometer
Optics Communications Volume 281, Issue 14, 15 July 2008, Pages 3827-3830

Reprints of the publications are added at the end of this thesis (Appendix B).

Chapter 1

Introduction

The thesis is divided into two parts: the first part handles about a new method of pulse compression for MHz repetition rate high energy lasers, the second part demonstrates for the first time how one can record continuous broadband near-field signals in phase and amplitude by near-field microscopy.

The first part is described in the chapters 1 to 4 and the second part in chapter 5. The results from the pulse compression part can be used as well in future for a new coherent broadband laser-system for near-field microscopy.

1.0.1 Outline of the thesis

Chapter 1 ... presents the motivation and fundamentals necessary to understand the successive chapter 1-4. We focus especially on the relevant case of self-phase modulation (SPM), including the influence of group velocity dispersion (GVD). We also discuss the properties of photonic crystal fibers (PCF) and the effect of self-focusing. Finally, we present a brief overview about the current status of other pulse compression experiments at MHz repetition rates.

Chapter 2 ... introduces the concept of chirped pulse compression. This concept allows us to increase the energy coupled into the fiber at MHz repetition rates without destroying it by self-focusing. We demonstrated chirped pulse compression using a 50fs, 500nJ, 5MHz commercial Ti:Sapphire oscillator, compressing it to 16fs with 400nJ, and showing its potential for sub-10fs pulses. We investigated also the group delay dispersion transfer from the input pulse chirp to the spectrally broadened output pulse, which surprisingly had to be compensated only partially. This has not been addressed in the optics community yet.

Chapter 3 ... describes the characterization of chirped pulse compression for further applications on a daily basis (long term stability, pulse-to-pulse fluctuation, polarization ratio and fiber damages). Furthermore, we investigate several physical aspects like circular polarization with respect to SPM and spectral broadening expansion. In a proof-of-principle experiment, we pushed spectral broadening and compression into the few-cycle regime, namely to 6fs with potential for even shorter pulses. We also provide details on the group dispersion delay curve of our applied chirped mirrors for pulse compression, and discuss the importance of individual measurements.

Chapter 4 ...addresses pulse compression in a different regime, namely with infrared high-average-power lasers at MHz repetition rates, like thin disk Yb:YAG lasers or Innoslab amplifiers. We present for the first time the successful spectral broadening in the μJ regime and demonstrate pulse compression with over 100W of input average power.

Chapter 5 ...discusses the experiment and results achieved in the field of nano-optics during the first part of my time as a graduate student. By combining Fourier-transform spectroscopy with scattering scanning near-field optical microscopy (s-SNOM), we developed a technique which allows to record a continuous broadband near-field spectrum in amplitude and phase in one single measurement run, instead of successively recording different single frequency wavelengths to a spectrum as currently done. We present near-field spectra of gold and silicon carbide and approach curves proving the functionality of our technique. Additionally, recording the novel type of "near-field interferograms" opens up a new way to investigate the near-field interaction and sample response.

Chapter 6 ...summarizes the presented results and conclusions of this thesis.

1.1   Motivation

The generation of few-cycle laser pulses represents a challenging task and is still a topic of active research. Having 20fs or even shorter pulses is important and desirable for many applications in the fields of physics, chemistry and biology. Furthermore, various fundamental experiments, in which the carrier envelope phase plays an essential role, rely on the generation of high-peak-power few-cycle pulses. For example, the growing field of attosecond spectroscopy requires isolated attosecond pulses, generated by high harmonic generation with few-cycle pulses. But just since the end of the nineties, intense few-cycle pulses usable for a broad range of experiments have been generated by self-phase modulation in a gas filled hollow core fiber. With this technique, 5fs short pulses with hundreds of μJ can be generated, but with the drawback of only Hz and kHz repetition rate. For pump-probe experiments this is very uncomfortable, as high repetition rates provide a better signal-to-noise ratio and less measurement time. Therefore, efforts have been undertaken to build high-energy, few-cycle laser systems at MHz repetition rates. One route is the idea of MHz noncollinear optical parametric amplification (NOPA) which has lead to promising results; but all the different MHz-NOPA approaches suffer from a certain degree of complexity, making it difficult and expensive to use for applications. Another route are high energy oscillators (thin disk lasers, chirped pulse oscillators) or new kinds of amplifiers like fiber, or Innoslab amplifiers. However, this route suffers from not delivering sub-20fs pulses, but rather between 50fs and 1ps, depending on the laser-system. A pulse compression stage is therefore unavoidable for reaching sub-20fs. Unfortunately, the hollow-core-fiber or filamentation techniques used in the kHz regime are not working in the MHz regime due to the smaller energy (only μJ) and the very high average power of today's existing laser systems. This forces us to use bulk materials, e.g. solid core fibers for pulse compression. But solid materials have the disadvantage that self-focusing can already be reached at low energies destroying the material and therefore disabling the energy scaling. It is therefore important to find a way to overcome the limitation of self-focusing, opening the few-cycle regime at MHz for experiments. This challenge has led us to the development, experimental demonstration and characterization of the concept of chirped pulse compression, overcoming the limitation set by self-focusing. The concept of

chirped pulse compression presents the most essential part of this thesis. Another important aspect of our research was addressed to the experimental setup and its applicability for daily use. Even though pulse compression with solid core fibers has been pursued since the seventies, there was so far no implementation of this technique into existing experiments on a daily use. Our experimental setup is simple, robust and space-saving. It has already been integrated into several experiments and can be easily rebuild by other groups. Currently, FEMTOLASERS Produktions GmbH in Vienna, Austria, is overtaking our developed and here presented technique of chirped pulse compression.

1.2 Fundamentals

For generating short pulses after an oscillator or amplifier one has to spectrally broaden the pulses and afterwards to compress them in time. The relevant spectral broadening processes in our experiments at MHz repetition rate is self-phase modulation in the normal dispersion regime. In this section we restrict ourselves to the most relevant physical processes concerning our experiments. Section 1.2.1, introduces first the case of self-phase modulation neglecting the influence of dispersion. The consequences of dispersion for self-phase modulation are covered in section 1.2.2 which is an essential aspect of our experiments. In section 1.2.3 we review the self-focusing process, as this one represents the main limitation concerning energy coupling into the fiber at MHz. So-called photonic crystal fibers (PCF) are introduced in section 1.2.4, which we use as waveguide for the spectral broadening process. Finally, section 1.2.5 gives a brief overview of the current status of other pulse compression experiments. The following discussion is oriented on [1–4], which also contain further detailed information concerning nonlinear processes and other spectral broadening processes.

1.2.1 Dispersionless self-phase modulation

Self-phase modulation is a third-order nonlinear process of light-matter interaction. It refers to the phenomena in which an intense laser pulse transiently modifies the refractive index through the optical Kerr effect and therefore imposes itself a temporal phase shift, leading to a change of the pulse's frequency spectrum.

As a consequence of third-order nonlinearity, the refractive index of most optical materials depends on the intensity propagating through the material (optical Kerr-effect):

$$n(I) = n_0 + n_2 I, \tag{1.1}$$

where n_0 is the refractive index of the medium in the absence of light and n_2 is the nonlinear refractive index [5]. For a sufficiently intense laser pulse, the refractive index will be a function of time, following the temporal shape of the intensity. This temporarily changing refractive index will affect the light wavelength in the material and thus produce a shift in the instantaneous phase of the pulse:

$$\phi(t) = \omega_o t - \frac{2\pi}{\lambda_0} n(I) z, \tag{1.2}$$

with w_0 and λ_0 as the vacuum carrier frequency and wavelength of the pulse, and z is the propagated distance of the pulse in the medium. The time-dependent nonlinear phase shift results in a frequency shift of the pulse. The instantaneous frequency follows as:

$$\omega(t) = \frac{d\phi(t)}{dt} = \omega_0 - \frac{2\pi}{\lambda_0} z \frac{dn(I)}{dt} \qquad \text{with} \qquad \frac{dn(I)}{dt} = n_2 \frac{dI(t)}{dt}. \tag{1.3}$$

Assuming a Gaussian pulse we derive:

$$\omega(t) = \omega_0 + \frac{4\pi z n_2 I_0}{\lambda_0 \tau^2} t e^{-\frac{t^2}{\tau^2}}. \tag{1.4}$$

The maximal spectral broadening for a Gaussian pulse can be estimated in the following way:

$$\Delta\omega = \frac{2\pi}{\lambda_0} z n_2 \frac{I_0}{\tau}. \tag{1.5}$$

Plotting $\omega(t)$ reveals the frequency shift of each part of the pulse whereas the leading (trailing) edge shifts to the lower (higher) frequencies (Fig.1.1). Note that the very peak of the pulse
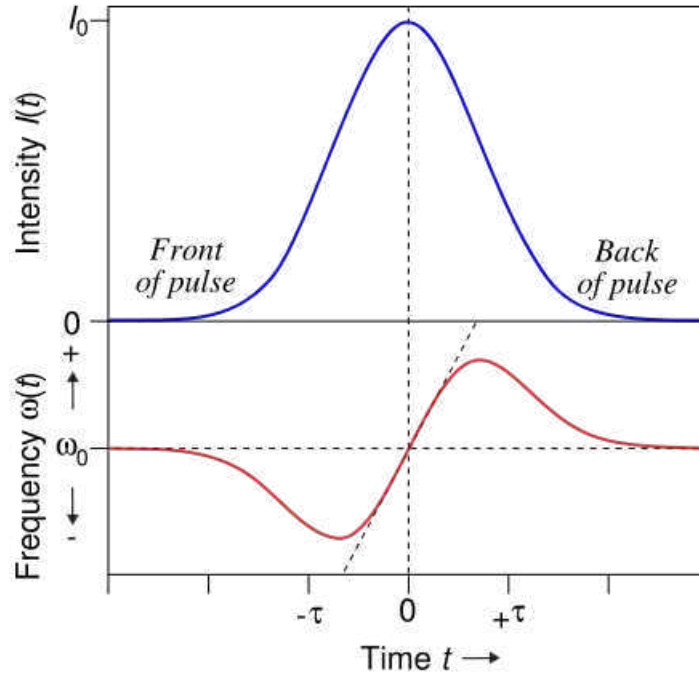
Figure 1.1: Pulse undergoes a self-frequency shift due self-phase modulation, picture from [4]

is not shifted. As can clearly be seen, a linear frequency shift (chirp) develops between the center of the pulse (t=$\pm$t/2):

$$\omega(t) = \omega_0 + \alpha t, \tag{1.6}$$

where α is the linear chirp coefficient:

$$\alpha = \frac{d\omega}{dt}\bigg|_0 = \frac{4\pi z n_2 I_0}{\lambda_0 \tau^2}. \tag{1.7}$$

It is important to notice that the proper chirp for linear pulse compression exists only in the central region of the pulse, whereas the opposite chirp on the wings of the pulse will lead to a temporal broadening. The non-linear chirp at the bending points of the instantaneous

frequency, which generates temporal side-pulses, can be removed by spectral windowing. Self-phase modulation without dispersion allows a compression of only around 60% of the total energy [6]. Including dispersion one can find an optimal fiber length which includes over 90% of the pulse's energy. This is sometimes called enhanced self-phase modulation or enhanced frequency chirping and will be discussed in the next section. Fig.1.2 shows a typical self-phase modulated spectrum. The spectrum is accompanied by a modulation structure covering the
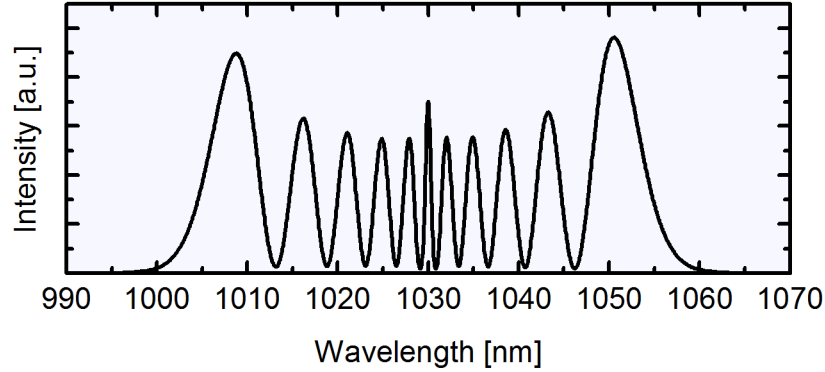

Figure 1.2: Typical self-phase modulated spectrum, simulated using [7]

entire frequency range with the outermost peaks as the most intense ones. The multipeak structure is an interference effect and has its origin in the time-dependency of the SPM induced frequency chirp (Fig.1.1). Namely, the same chirp occurs at two values of t, showing that the pulse has the same instantaneous frequency at two different times. Qualitatively speaking, these two time points represent two waves of the same frequency but different phases that can interfere constructively or destructively depending on their relative phase difference. At the frequency extrema, the phase difference is always zero. These peaks are stronger in power because a relatively broad range of times contributes to the same instantaneous frequency. The modulation period is given by

$$\delta\omega \approx \frac{4\pi}{t}.$$
(1.8)

This formula will help to clearly identify self-phase modulation spectra, as sometimes every spectral modulation is wrongly assigned to self-phase modulation. Counting the number of peaks M, one can estimate the maximum phase shift by [1]

$$\phi_{max} \approx (M - \frac{1}{2}\pi).$$
(1.9)

Together with equation

$$\Delta\omega_{max} = 0.86\Delta\omega_0\phi_{max},$$
(1.10)

one can estimate initial bandwidth or pulse width if the pulses are unchirped. Note that the spectral bandwidths are defined as the at 1/e. Further information and derivations can be found in [1, 3], especially about the nonlinear propagation equation which we have left out here.

1.2.2   Self-phase modulation including normal dispersion

Using sub-100fs input pulses, one cannot anymore neglect the influence of the material (normal) dispersion during self-phase modulation. The normal dispersion will significantly change the pulse properties of the SPM broadened pulse, essential for the successive compression. Most relevant is the reshaping of the pulse duration into a flat-topped intensity profile after a certain distance in the medium. Thereby the entire pulse will become nearly positive linearly chirped, which enables a large fraction of the input energy to be in the compressed pulse. The reshaping by combined SPM and GVD is sometimes called "dispersive self-phase modulation" and the linearization of the chirp over the entire pulse is called "enhanced frequency chirping". Fig.1.3 compares the dispersionless SPM to the case of SPM and GVD combined. Comparing
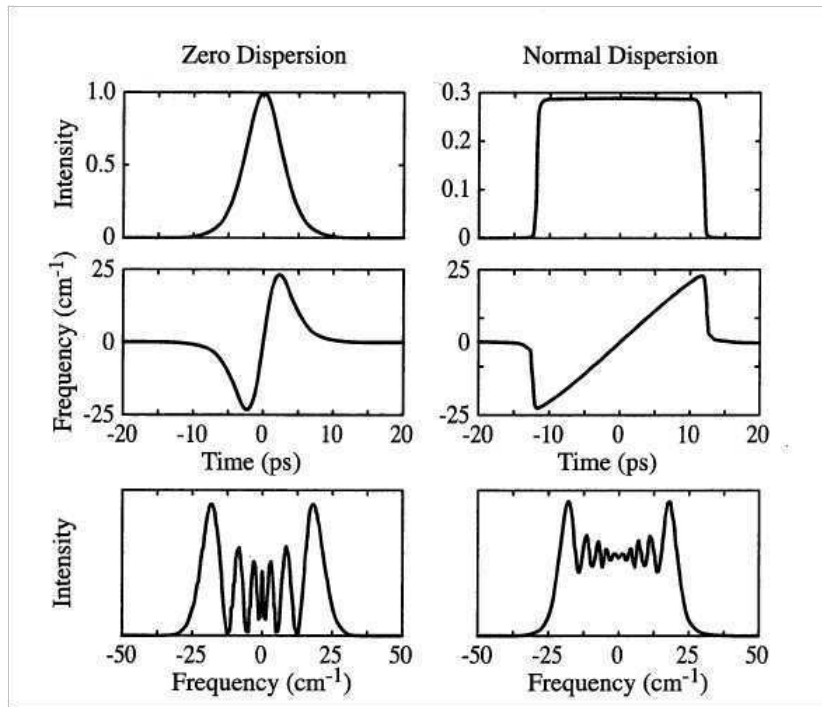
Figure 1.3: Comparison of SPM without dispersion (left column) and with dispersion (right). Picture taken from [6].

the two columns we clearly see that if dispersion is included (right column), the pulse duration spreads and develops a rectangular profile with steep leading and trailing edges. As the new frequencies are primarily generated at the leading and trailing edges, which move gradually in time, the pulse develops a mostly linear frequency chirp. For maximal energy in the compressed pulse, an optimal fiber length z_{opt} has to be chosen, depending on the input laser parameters as well as the fiber's characteristic. It is also important to know that the combined interaction of SPM and normal dispersion leads to an enhanced pulse broadening compared with the pule duration one expected of normal dispersion alone to the pulse [1]. An uncompressed pulse, leaving a fiber with length z_{opt}, is roughly 3 times longer as if only normal dispersion would have acted on it [8], independent of the input laser and fiber parameters (in first approximation). Numerical simulations [8] have found for z_{opt}:

$$z_{opt} \approx 2.5\sqrt{L_D L_{NL}}. \tag{1.11}$$

With the dispersion length L_D and the nonlinear length L_{NL} defined by

$$L_D = 4\ln(2)\frac{\tau^2}{|\beta_2|} \qquad \text{and} \qquad L_{NL} = \frac{1}{\gamma P_0}. \tag{1.12}$$

Note that t_0 is the full width at half maximum (FWHM) pulse width and P_0 the peak power of the incident pulse. β_2 is the GVD of the fiber value at the given wavelength and γ the nonlinearity parameter of the fiber:

$$\gamma = \frac{n_2\omega_0}{cA_{eff}} = \frac{2\pi n_2}{\lambda_0 A_{eff}}. \tag{1.13}$$

As we see, the optimal length depends on the input pulse duration and peak power as well as on the nonlinearity parameter. Changing one of them will change the optimal length. Optimum compression ratio is reached at the same fiber length and has been numerically found as [8]

$$\frac{\Delta t_{compressed}}{\Delta t_{in}} \approx 1.6\sqrt{\frac{L_{NL}}{L_D}}. \tag{1.14}$$

Comparing the spectra in Fig.1.3, we notice that the spectrum of SPM and normal dispersion is smoother and the depth of the modulation is washed out compared with the dispersionless SPM. This is explained by the relative strength of the contributions from the two time points, that are now very unbalanced. Hence the modulation depth is reduced. Other effects which can appear by the combined action of SPM and normal dispersion are described in [1,3], but with exception of optical wave breaking [9], they are negligible in our measurements. We draw your attention again that for an efficient pulse compression the optimal fiber length should be chosen. For a more detailed discussion and mathematical derivations we refer to [3,6,8].

1.2.3 Self-focusing

Self-focusing is based on the Kerr effect and occurs in any material which has a positive $\chi^{(3)}$. Thereby, the spatial intensity distribution of the beam generates an increased refractive index for the inner part compared to the outer part of the beam. This modified refractive index distribution then acts like a focusing lens. The beam size will be reduced leading to an even stronger intensity, which will change again the refractive index, increasing the self-focusing effect. A run-away effect can occur, if the power is larger as the critical power P_{cr}, given by the material (for a Gaussian beam):

$$P_{cr} = \frac{3.77\lambda_0^2}{8\pi n_0 n_2}. \tag{1.15}$$

Remarkably, the critical power P_{cr} is approximately independent of the original beam area. Self-focusing can result in very high intensities which can lead to a collapse of the beam, destroying the fiber. This collapse distance z depends on the critical power as well as on the focus beam radius:

$$z = \frac{0.367\frac{2\pi}{\lambda_0}r^2}{\sqrt{(\sqrt{\frac{P}{P_{\mathrm{cr}}}} - 0.852)^2 - 0.0219}}.$$ (1.16)

The self-focusing collapse presents a severe limitation for many fiber applications with ultra-short pulses. For pulsed laser systems the critical power is determined by the peak power and not by the average power.

1.2.4   Photonic crystal fibers

Using a waveguide respectively a single mode fiber for self-phase modulation has two main advantages compared to bulk or gas mediums: First, the waveguide enables a high intensity over a long interaction length, allowing an efficient spectral broadening. And second, because of the single mode propagation in the fiber, the chirp is independent of the transverse position on the output beam (the entire output beam has the same chirp). Therefore, self-phase modulation experiments with fibers, e.g. step-index fibers, have been started already in the 70's. However, step-index fibers have some limitations:

1. Step-index single mode fibers for 800nm wavelength have due the cut-off frequency of the fiber a limited single mode spectral range from ∼630-850nm.

2. Single mode operation is only sufficiently achieved with core diameters smaller then 10μm.

3. Exact fiber mode matching for single mode operation is necessary.

All these limitations mentioned above have been overcome by photonic crystal fibers (PCF), pioneered by P. St. J. Russell in 1996 [10, 11]. Therefore, in our experiments we decided to use these PCFs. A photonic crystal fiber is based on a two-dimensional photonic crystal but infinite in the third dimension, hence forming a fiber. Contrary to a normal step-index fiber, the waveguide properties of a PCF are not coming from a spatially varying glass composition but rather from the photonic crystal design which is an arrangement of very tiny and closely spaced air holes going through the whole length of the fiber. The simplest (and most often used) type of photonic crystal fiber has a triangular pattern of air holes, with one hole missing (see Fig. 1.4), i.e. with a solid core surrounded by an array of air holes. The guiding properties
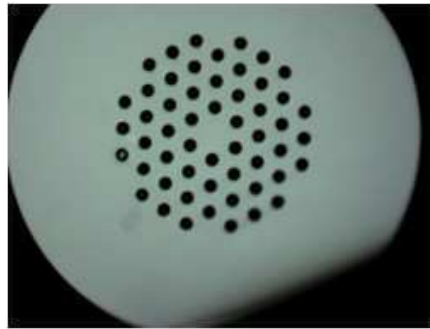

Figure 1.4: Fiber surface of a photonic crystal fiber with a core diameter of 25μm (LMA-25), self-taken picture.

of this type of PCF operate on the same principle as the step-index fibers. Respectively, the core has a higher refractive index as the microstructured cladding. The effective refractive index contrast between core and cladding can be much higher as in step-index fibers. Another type of PCFs are so called photonic band-gap fibers, in which the light is confined by a photonic band-gap created by the photonic crystal. Such a band-gap can confine the light in a lower index core or even in a hollow core [12].[1] However, in our experiments we didn't use photonic band-gap fibers; therefore we will not go into further details. PCFs attracted a lot of attention during the last years as they offer many degrees of freedom in their design to achieve a variety of peculiar properties. Compared to a step-index fiber, a PCF has the following advantages:

1. Engineering the dispersion waveguide: depending on the photonic crystal structure the zero dispersion wavelength can be shifted far into the visible.

2. Endlessly single mode: Over the full spectral range single mode operation is achieved [11].

3. Single mode operation with large mode area fibers: the photonic crystal structure allows increasing the core to over 100μm in diameter but still being truly single mode.

4. Exciting the fundamental fiber mode does not require perfect numerical aperture matching.[2]

For the optic community the first point is very essential, as the zero dispersion wavelength (ZDW) can be shifted to below the laser wavelength. The laser wavelength is then in the anomalous dispersion regime of the waveguide which allows the generation of solitons. However, for our purpose we have to stay always with the spectrum in the normal dispersion regime to avoid soliton fission, see the next subsection below. To avoid the anomalous dispersion regime we have to take so called large mode area photonic crystal fibers (LMA) for our experiments. As their core diameter is 5μm and larger, the waveguide dispersion can be neglected. Hence there is no shift of the zero dispersion wavelength which is approximately the same as the one of the fiber material. Our PCFs consist of quartz with a ZDW at 1.3μm. Fig.1.5 shows the near-, and far-field of a PCF. As can be clearly seen, the near-, and far-field
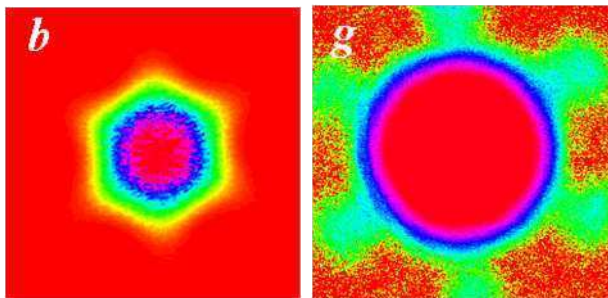

Figure 1.5: Near-field (b) and far-field mode (g, in dB scale) of a PCF, picture from [13].

of a PCF exhibits a hexagonal shape which is different from the well-known single mode of a

---

[1]Not to be confused with hollow core fibers which are used for pulse compression at kHz repetition rate.
[2]We are not aware of a publication which mentions this characteristic.

step-index fiber. The near-field rotates twice by $\frac{\pi}{6}$ when transforming into the far-field and six satellites form around a nearly Gaussian far-field pattern. Therefore, sometimes the single mode of the PCF is described as the "fundamental mode of the PCF". However, if we write "single mode" we refer here to the fundamental mode of the PCF, as it is commonly done.

PCFs are overcoming the described limitations of step-index fibers and present itself as a very suitable alternative for our experiments. Today, PCF are commercially available with a sufficiently good quality and reproducibility.

Supercontinuum generation by soliton fission in photonic crystal fibers

We clearly have to distinguish between supercontinuum generation by soliton fission [14] in photonic crystal fibers and the one by self-phase modulation [1]. Because, supercontinuum generation by soliton fission is not suitable for our high-energy pulse compression experiments due the complicated pulse structure and the very limited amount of energy which can be coupled into the fiber. Soliton fission is generated if the incoming laser wavelength lies in the anomalous dispersion regime of the waveguide, contrary to self-phase modulation which requires the normal dispersion regime. Using large mode area fibers with a ZDW around 1.3μm we can avoid any kind of soliton fission.
PCF allows to engineer the zero dispersion wavelength beneath 600nm, enabling Ti:Sapphire oscillators to generate extremely large supercontinuum spectra by soliton fission. Nowadays, such supercontinuum are well-known in optics and used for many applications in spectroscopy and metrology. Unfortunately, due to the very small core diameter ($<3\mu$m) necessary for the ZDW engineering, one cannot couple much energy into such a fiber (maximally few nJs). Nevertheless, the question arises if such a over octave spanning supercontinuum can be compressed. Using short enough input pulses (<100fs) these spectra are fully coherent. Compression is theoretically possible but practically very complicated. Fig.1.6 points this clearly out. The spectrum consists of several solitons with different spectral parts and pulse durations, distributed over a duration of several picoseconds. Compression of soliton spectra has been demonstrated by either choosing a correct fiber length (only a few mm) for self-compression of the soliton [15] or by adding the solitons together [16], which has been currently done with only 2 solitons, not stable over longer time. A very good review article is presented in [14].

1.2.5   Overview of state-of-the art pulse compression experiments

Depending on the used laser-system and desired output values one can choose between different pulse compression schemes. We briefly present an overview of frequently used pulse compression techniques and their latest status.

For laser systems with Hz and few kHz repetition rate one uses often gas filled hollow core fibers (HCF) [17, 18] which can handle up to 1mJ of input energy. Thereby, self-phase modulation is the dominant spectral broadening process. Using the technique of gradient gas pressure in HCFs one was able to couple 5mJ [19] into the HCF. New approaches like cross-phase modulation [20] or hollow planar waveguides [21] with even 8mJ of output energy are currently under development. HCFs have been shown working up to 100kHz [22, 23], and also with an input energy of only 4μJ [22]. Normally, several tens of μJs are used as minimum input energy. A good review is given in [24]. Another technique in the same repetition rate regime is spectral broadening in gases through filamentation [25]. Pulse compression down
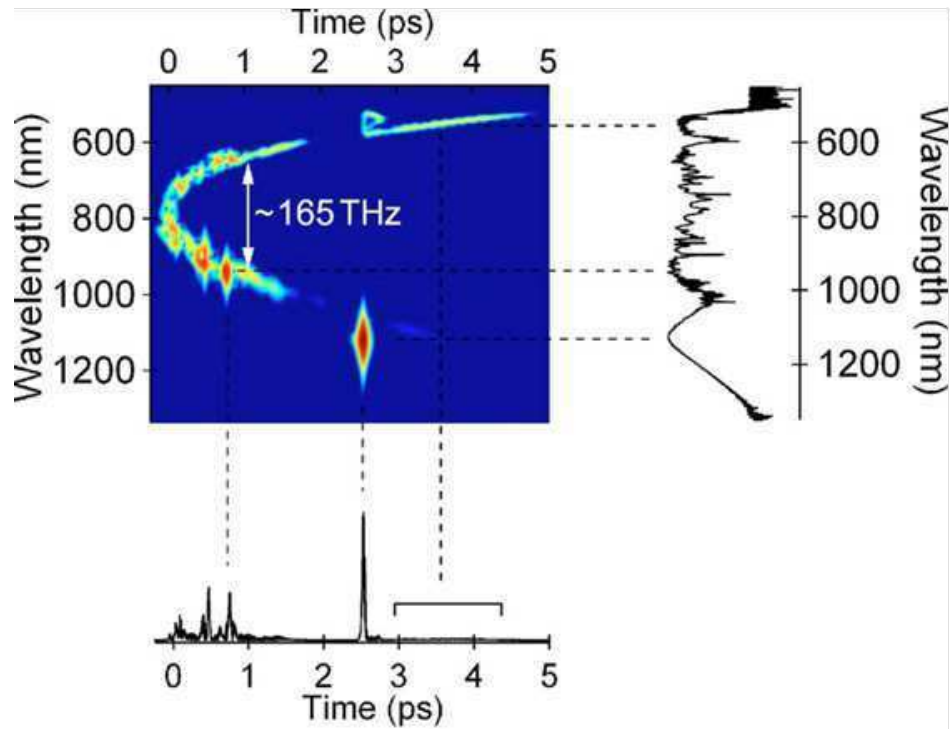
Figure 1.6: Simulated supercontinuum spectrogram projected onto the temporal intensity and spectrum for input pulses at 835nm of 10kW peak power and 50fs FWHM propagating in 15cm of PCF. Picture from [14].

to 4fs has been demonstrated [26] but the technique suffers on a small useable transmission and of a beam break-up into many filamentations at high input energies (>mJ). Recently, filamentation with chirped input pulses has been published [27]. Thereby, one has surprisingly found for several special input chirps the phenomena of self-compression [27, 28]. Efforts are underway to scale this approach into the high mJ input energy regime.[3] The hollow core fiber and filamentation technique cannot currently be scaled to the MHz repetition rate regime, due too less input energy of the available MHz laser systems and more essential, damage problems of the materials.

At MHz repetition rate, one so far uses mainly solid core single mode fibers for spectral broadening through self-phase modulation. During the 70's and 80's, fundamental experiments have proven the concept using step-index fibers but it has not found widespread applications in research. One reason may have been the development of few-cycle oscillators at the beginning of the 90's. First in 2003, with the up-coming of photonic crystal fiber, respectively their large mode area fibers, the potential for high energy pulse compression at MHz repetition rate has been demonstrated [29]. Thereby, a 800fs pulse has been compressed down to 33fs with 0.5μJ of output energy at 34MHz repetition rate. Few experiments have followed but not surpassing the first one [30–33]. During the last years laser systems [34–36] at MHz repetition rate have been developed with output values above the self-focusing threshold of the fiber's material. This limits the available energy in a compressed pulse using such a laser-system but has been overcome through the technique of chirped pulse compression

---

[3]private communication, Salamanca optics group

(see chapter 2). Currently, pulse compression experiments concerning >100W laser systems and >μJ input energies at 1030nm are underway. Another pulse compression technique is the white-light generation, amplification and successive compression, respectively the amplification of a few-cycle laser at MHz repetition rate. Though some experiments [37–39] have demonstrated promising results, the whole setup suffers on a certain complexity and stability which currently does not support its application for daily research. Furthermore, only MHz repetition rates up to 2MHz have been shown.

The commercial availability of high energy laser systems at MHz repetition rate, but with slightly too long pulses for many desired applications, makes (chirped) pulse compression a very interesting alternative for short pulse generation.

Chapter 2

Chirped pulse compression

There is an increased interest of the optic community to have laser systems at MHz repetition rate with short pulses and high energies for daily applications, but even the generation of sub-15fs laser pulses with hundreds of nJ pulse energy represents a challenging task today. Nevertheless, a variety of applications like high harmonic generation [40], resonant plasmonic field enhancement [41], material processing [42], ultrafast spectroscopy, respectively femto-chemistry, as well as biophysics would strongly profit from the increased signal to noise ratio, total flux, or reduced measurement and processing time. One approach for generating short and intense pulses at MHz repetition rates is the use of noncollinear optical parametric amplifiers (NOPAs) with typical achievements at 800nm of 400nJ, 15fs at 1-2MHz [37–39]. Unfortunately these MHz-NOPAs suffer from a certain complexity in size and stability due several nonlinear conversions to be combined. Duplicating and managing these laser systems for other groups is currently not that attractive. Alternatively, intense pulses at MHz repetition rates can be produced by long-cavity oscillators [34, 43, 44], fiber- [35, 45], or Innoslab amplifiers [36], but the pulse duration is so far only around 40fs to 1ps in these systems. Directly reaching shorter pulse durations seems currently not feasible. An external pulse compression stage is therefore required.

At MHz repetition rate, successful and efficient pulse compression can be only achieved using a bulk material for spectral broadening, respectively a solid waveguide. Techniques like hollow core fibers or filamentations, which are routinely applied at kHz repetition rate, will not work at MHz because the available input energy is insufficient (at least several μJs are needed). Also, the high average power at MHz repetition rate can lead to thermal effects and damages. Currently, the only real option for spectral broadening at MHz repetition rate is using single-mode fibers. Several experiments during the last years have proved, with different input conditions, that in general this approach works fine [29, 32, 46–48]. However, all these experiments had quite low input energies, respectively the peak power of the input laser beam stayed under the self-focusing threshold of the material. Nowadays, laser systems at MHz exist [34–36, 49] which surpass several times this self-focusing threshold. Therefore, self-focusing will destroy the front part of the fiber and thereby limits the energy coupled into the fiber to a fraction of the available one.

Here we demonstrate how to overcome this fundamental limitation by using the well-known technique of chirping the input pulses to decrease the input peak power. This allows to couple significantly more energy into the fiber and we demonstrate that the additional energy restores again the same spectral broadening, respectively compressed pulse duration

as using unchirped input pulses. We call this approach chirped pulse compression. In section 2.1 we introduce in detail the chirped pulse compression approach and we demonstrate it experimentally in section 2.2 with emphasis on its scalability [50]. In section 2.3 we consider the influence, respectively transfer, of the input chirp to the pulse after spectral broadening, with some surprising results. A summary and conclusion is presented in section 2.4.

2.1 The concept of chirped pulse compression

Current laser systems at MHz deliver a peak power that lies above the self-focusing threshold of common optical materials. Therefore the maximally coupled energy into a material, respectively a fiber, is less than what is available. To overcome this limitation we use the fact that self-focusing depends to first approximation only on the peak power of the beam, but not on the focal area. Simply chirping the input beam allows us to couple more energy into the fiber before the threshold peak power for self-focusing is reached. This concept has been developed in the 60's for radar technology and applied since the 80's for laser pulse amplification [51] with mostly a negative input chirp. For pulse compression one has to consider additionally two more important points. First, how do we have to chirp our input beam (positively or negatively) and second, does the additional coupled energy allow to restore the spectral broadening back to its original spectral bandwidth of the unchirped case as well as to compress the pulses? Theory tells that this should be indeed the case. Because the spectral broadening by (pure) self-phase modulation is proportional to I/t, respectively to E/t for a fixed repetition rate, as well as the self-focusing threshold is given by the peak power which is proportional to E/t. We recognize that a 5 times longer pulse will allow to couple 5 times more energy while achieving the same spectral bandwidth. However, the derived conclusion is based on formulas assuming long Fourier-limited pulses and not heavily chirped pulses. Furthermore, we do not know if these approximately formulas are still valid concerning our (extreme) input parameters. Only through the experiment we can find out to what extent the additional energy can restore the spectral broadening concerning chirped input pulses. This subject will be handled during the next section. Thereby we found that the additional energy completely restores the spectral broadening. Concerning the input chirping, our approach requires positive chirp as negative chirp will result in spectral narrowing. Respectively if all negative chirp of the input pulse can be compensated by the positive chirp of the fiber's material, one achieves a compressed pulse in the fiber which afterwards undergoes spectral broadening or if the peak power is to high, collapses due self-focusing.

The describe concept of positively chirping the input pulses and restoring the bandwidth and compressed pulse duration through the additional coupled energy we call chirped pulse compression and is stated as follows:

> "Stretching the input pulse duration through positive chirp will decrease its peak power under the self-focusing threshold and allows to couple more energy into the fiber until the threshold is reached again. The maximally additional coupled energy restores the spectral broadening back to its original bandwidth of the unchirped case as well as we can compress the broaden pulse to the same pulse duration."

2.2   Demonstration of the chirped pulse compression concept

We used a commercial chirped pulse Ti:Sapphire oscillator (Scientific XL, Femtolasers Produktions GmbH) with an output of 500nJ, 55fs and 5MHz at 800nm central wavelength. The high intracavity energy requires to operate the oscillator in the positive dispersion regime [34], hence the pulses are positively chirped at the output coupler. An extracavity prism compressor is already included in the commercial laser-system. Translation of these prisms enables us to positively or negatively chirp the system's output pulses. The experimental setup is shown in Fig.2.1. A Faraday isolator is placed directly after the prism compressor to protect the
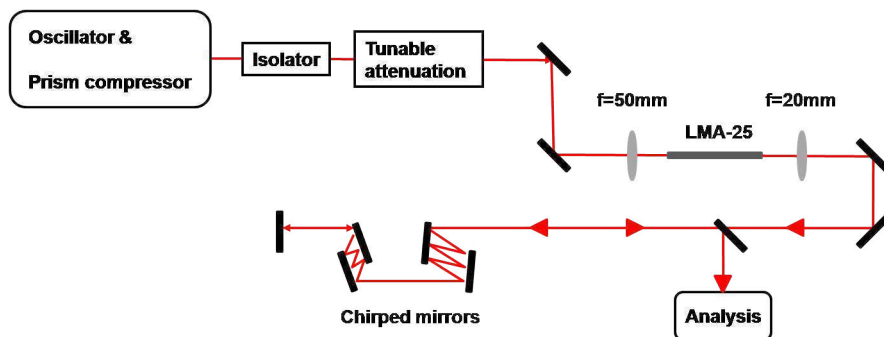

Figure 2.1: Experimental setup

laser's mode-locking from back-reflections from the fiber's input surface. A tunable attenuation stage follows, consisting of an achromatic half-wave plate and a polarizer. By rotating the half-wave plate, an adjustable energy range of 0 - 400nJ is thus provided without changing the chirp. For spectral broadening, we selected a commercial large-mode-area photonic crystal fiber from NKTPhotonics (LMA-25, Thorlabs) with a mode-field diameter of $20\mu m$, and a zero-dispersion wavelength of $\sim 1.3\mu m$. The LMA-25 fiber lies freely in a self-made V-groove holder which is placed onto a 3-axis translation stage. A fiber length of 30mm was used [6,8]. For our beam diameter of about 3mm, we selected antireflection-coated aspherical lenses with f≈50mm for focusing and with f≈20mm for collimation. Optimizing the single-mode excitation, we used the lever arm placed before the focusing lens. With the extracavity prism compressor of the laser system we set the input pulses to its desired pulse duration after the focusing lens before the fiber. Compression of the spectrally broadened pulses is achieved by using double-angle chirped mirrors [52], which were designed for a bandwidth from 680nm to 890nm and for -100fs^2 per reflection, without compensation of higher-order dispersion (see 3.6.1). We used 24 reflections in combination with several mm of quartz blocks and wedges for fine tuning. The compressed pulses are characterized by interferometric autocorrelation (Femtometer, Femtolasers Produktions GmbH). The total setup of spectral broadening and compression covers a space of only 35 x 65 cm.

The results of the proof-of-principle experiment for chirped pulse compression is presented in Fig.2.2. The upper row of Fig.2.2 shows the spectral broadening of Fourier-limited pulses and its compression. We adjusted the input energy to around 75% of the self-focusing threshold, resulting in an input energy of $\sim$90nJ with 55fs. Figure 2.2a shows the input spectrum (dotted) and the broadened spectrum (solid); note the linear scale. The transmission efficiency was 87% ($\sim$78nJ after the collimating lens). The spectrum's Fourier limit was 12.0fs and the autocorrelation (Fig.2.2b) indicated a pulse duration of 14.5fs. Thereby we had to
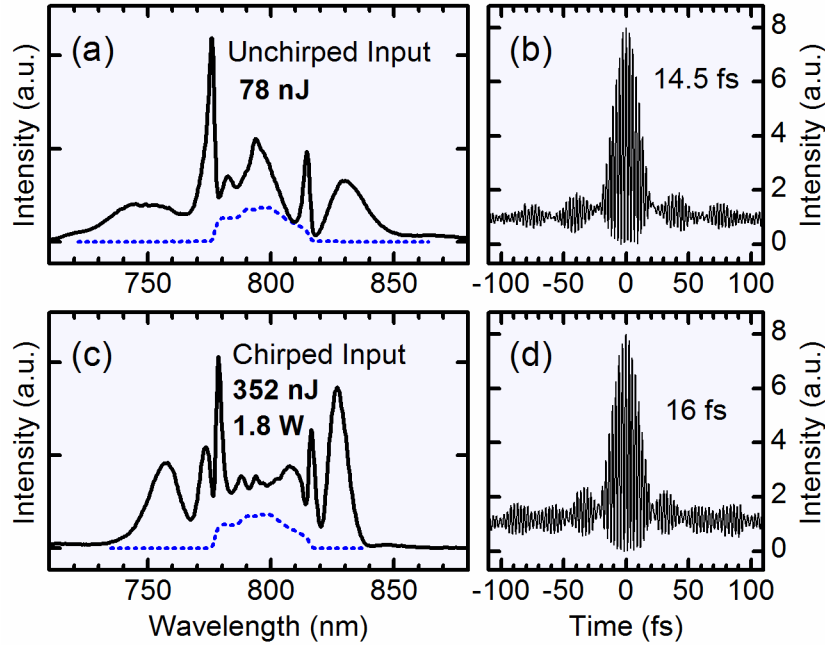
Figure 2.2: Unchirped (a,b) and chirped (c,d) spectral broadening and pulse compression

add 26.9mm of quartz additionally to the chirped mirrors. The lower row of Fig.2.2 shows the results for a positively chirped input pulse. With the laser system's prism sequence, we positively chirped the pulses to a duration of ∼215fs (full width at half maximum of the intensity). This made it possible to couple in and broaden the full available pulse energy of ∼402nJ without damage. Output pulses with ∼352nJ (average power 1.76W) were measured directly after the fiber, which corresponds to a transmission of 88%, similar to the unchirped case. This represents a factor of four more energy as when using Fourier-limited input pulses. The spectrum (Fig.2.2c) had a Fourier-limit of 14.5fs and the measured pulse duration was 16fs (Fig.2.2d). Only 10mm of quartz, corresponding to 400fs^2, had to be added for best compression.

The similarity of the two spectra and autocorrelations shows that chirped input pulses provide a comparable broadening and compression, but at higher energies. In both cases, chirped and Fourier-limited, the dominant process for spectral broadening is self-phase modulation influenced by group velocity dispersion [1], which is evident from the typical spectral shapes. Comparing the autocorrelations with the calculated Fourier-limited autocorrelation of the respective spectra we found a very good agreement. This means that the shown side maxima of Fig.2.2b and d are an inevitable result of the spectral shape. The positions and shapes of all side maxima in the range of ±150fs have been reproduced by calculation (see also 3.1). We attribute the residual deviations to the missing third-order-dispersion correction of the fiber and quartz material. However, not much more higher-order chirp seems to be induced by the chirped case as compared to the Fourier-limited case. Using better chirped mirrors we expect to compress the pulses to their Fourier-limit.[1]

Fig.2.2 represents a conceptual proof of the concept of chirped pulse compression. In order to further clarify our concept we investigated its behavior. We measured the achieved output

---

[1]In section 3.1we show a nearly Fourier-limited pulse compression of ∼6fs.

energy using different input pulse durations, when the spectral width of the Fourier-limited case was maintained. For unchirped pulses, the input peak power was set to around 75% of the self-focusing threshold, which resulted in a spectrum extending from about 730 - 860nm (Fourier-limit ~14fs). For each input chirp value, we increased the input power until a similar spectral broadening was reached. At constant broadening (Fourier-limit of ~14fs), the achievable output energy (triangles) increased directly with the input pulse duration, shown in Fig.2.3. The calculated resulting input peak power, plotted in Fig.2.3b, stayed always in
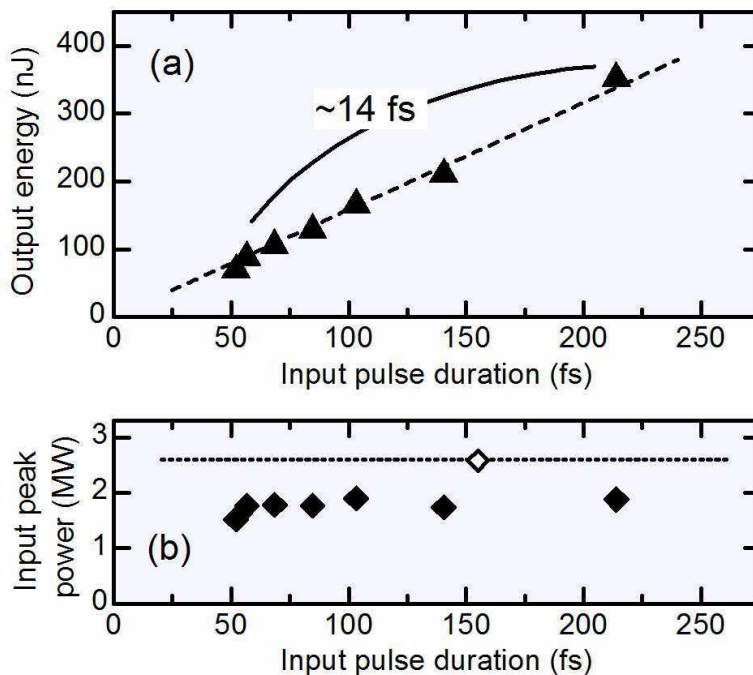

Figure 2.3: Energy scaling

the same range of 75% below the self-focusing threshold for fused silica (dotted line) as set at the beginning for the unchirped pulses. This observation indicates that self-focusing is currently, under these input conditions of our laser system, the only limiting process concerning the input energy. Therefore we believe that our concept of chirped pulse compression can be further extended into the μJ regime, by using chirped pulse oscillators with a higher input energy in combination with a stronger chirp. The concept of chirped pulse compression is general for broadening schemes where self-phase modulation and self-focusing presents the dominant nonlinear processes. Hence, it should be also applicable to different laser systems like e.g. Yb:KGW or Yb:YAG based lasers.

For this proof-of-principle experiment the input peak power was always set to around 75% of the self-focusing damage threshold which has resulted in a final pulse duration of approximately 14fs. Setting the input peak power closer to the threshold, in combination with lesser chirping, generates a larger spectral broadening, which allows us to reach 10fs with the full available energy of our laser-system. In Fig.2.4, with an input energy of ~400nJ, we adjusted the peak power closely to the damage threshold (open diamond in Fig.2.3b), achieving a spectral broadening corresponding to 11fs with a transmission of 88% (354nJ) in a LMA-25 fiber of 29mm fiber length. The input pulse duration was around 155fs which is

significantly less as the earlier used 215fs. We expect that the sub-10fs regime can be reached
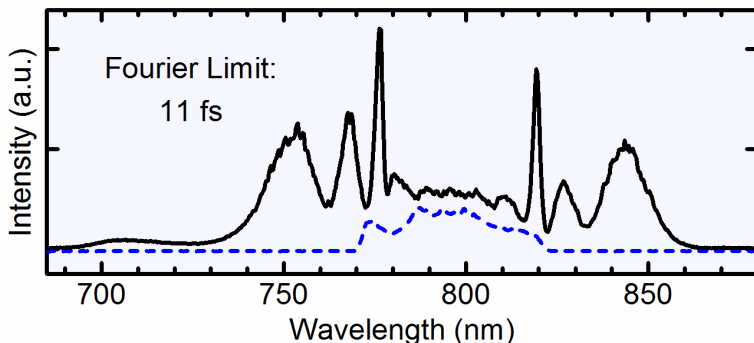

Figure 2.4: Spectral broadening corresponding to 11fs with 350nJ of output energy at 5MHz

at our oscillator's full energy by using a fiber with a somewhat smaller mode field diameter. The higher intensity should lead to an increased broadening at constant peak power. At the very beginning of our measurement series we even achieved spectral broadening for sub-10fs pulses as the laser's output pulses were 50fs long instead of 55fs. Fig.2.5 shows the spectrum, corresponding to a Fourier-limited pulse of 9.0fs with an input energy of 214nJ, respectively 175nJ of output energy, in a LMA-25 fiber of 21mm fiber length. All the shown spectra were
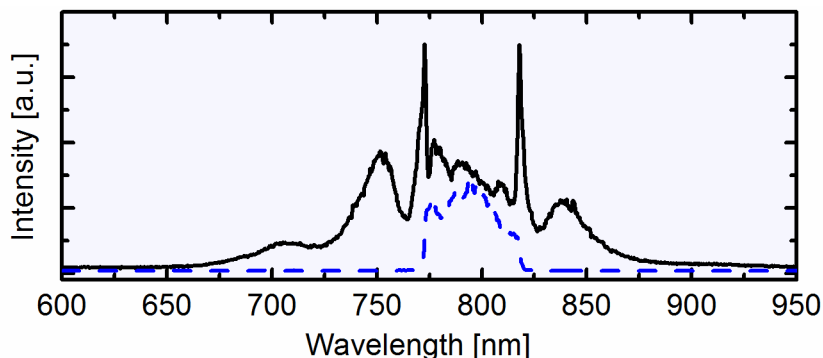

Figure 2.5: Toward sub-10fs pulses: spectral broadening corresponding to a 9.0fs pulse with 175nJ of output energy at 5MHz.

stable for at least one hour. Detailed information to stability and polarization aspects are presented in chapter 3.

We have demonstrated the concept of chirped pulse compression and shown its scalability to higher energies respectively into the sub-10fs range using a chirped pulse oscillator. Because of the setup's simplicity, the combination of a commercial chirped pulse oscillator with our simple chirped pulse compression scheme will be a convenient source of shortest pulses for applications.

2.3   Dispersion transfer in chirped pulse compression

We introduced and demonstrated the concept of chirped pulse compression for high energy pulses at MHz repetition rate. But an essential aspect we have not yet addressed. Namely,

how the added input dispersion affects the output dispersion after spectral broadening. We restrict the following discussion to the group delay dispersion as we were not able to quantify higher order dispersion.

The importance of this aspect gets clear if one consider that for stretching a pulse from 55fs to 200fs, as done in our experiments, one needs a group delay dispersion (GDD) of ∼2000fs^2 which can be easily achieved using glasses or changing the prism compressor of the laser-system. Compensating a chirp of 2000fs^2 is much more difficult especially if the spectral bandwidth is large because the maximally GDD compensation per reflection on the chirped mirror decreases with larger bandwidth. In principle one could apply chirped mirrors but in practice one is forced to use many reflections which would lead quickly to a certain pulse distortion as the chirped mirrors are not perfect compensating (see section 3.6). A combination of chirped mirrors and prism compressor respectively grism would be necessary to compensate this amount of GDD which comes additionally to the GDD of the waveguide. The increase of complexity in the setup would be large, especially for the sub-10fs case. Therefore it is important to know how the input dispersion adds to the output dispersion after spectral broadening. Analyzing the chirped pulse compression we surprisingly observed that the added input dispersion, respectively GDD, has to be compensated only to a fraction of its original value. We found that this observation cannot be explained only by the increased spectral bandwidth. However, the observed behavior supports essentially the manageability and scalability of the concept of chirped pulse compression. We are not aware of any detailed measurement series published concerning this observation.

In the following subsection, we present first detailed measurements of the dispersion transfer during chirped broadening. First we define a GDD ratio which we introduce for a better understanding and analyzing of our measurements. After, we present GDD ratio measurements taken under different experimental conditions, and finally we give a first outlook concerning possible explanations.

2.3.1   GDD ratio

The GDD transfer has been measured in the way shown in Fig.2.6. With Fourier-limit input
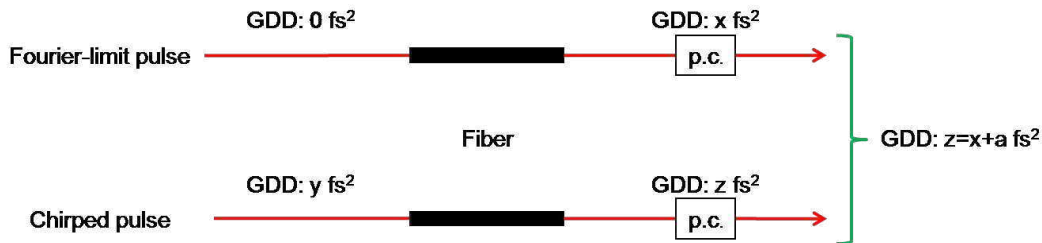
Figure 2.6: Measurement of the GDD ratio, see text for explanation.

pulses, hence 0 fs^2 of input GDD, we have to compensate x fs^2 after spectral broadening. Using chirped input pulses with an input GDD of y fs^2 and maintaining the spectral bandwidth (or the input energy) of the Fourier-limit case, we have to compensate now z fs^2 for best pulse compression. The difference $a=z\text{-}x$ represents the additional GDD which has to be compensated in the chirped case. With that we define the GDD ratio g as follow:

$$g = \frac{y}{a} = \frac{\Delta \quad \text{input GDD}}{\Delta \quad \text{output GDD}} \qquad (2.1)$$

In the following graphs we name $a = \Delta$ output GDD and $y = \Delta$ input GDD. Note, that the way how we measure the output GDD and the definition of the GDD ratio are very convenient to recognize how much additional GDD has to be compensated in the chirped case, which is the essential point for using chirped pulse compression in applications. During the next subsections we investigate the GDD ratio under different experimental situations.

2.3.2   GDD ratio under maintaining the spectral bandwidth

In this first experiment we investigate the GDD ratio when increasing the input chirp but in parallel maintaining the broaden spectral bandwidth. Thereby, the spectral broadening and pulse compression using Fourier-limited input pulses serve as the reference point for the chirped case. Increasing now the input chirp reduces the spectral bandwidth of the output spectral broadening due a longer input pulse duration. Therefore we have to increase the input energy to restore back, respectively to maintain, its original broadened spectral bandwidth. Measuring the additional output GDD as defined above allows us to calculate the GDD ratio. In Fig.2.7(a) we plotted the measured output chirp in relation to the input chirped. We used a 15.25mm long LMA-25 fiber. The blue/ red curve corresponds to a chirping with prism/ bk7 blocks. Fig.2.7(b) shows the calculated Fourier-limit of the corresponding spectra, which is around 12.7fs. Especially for the red curve it stays constant whereas for the very strong chirping (blue curve) it slightly decreases.[2] It is obviously from Fig.2.7(a) that only a fraction
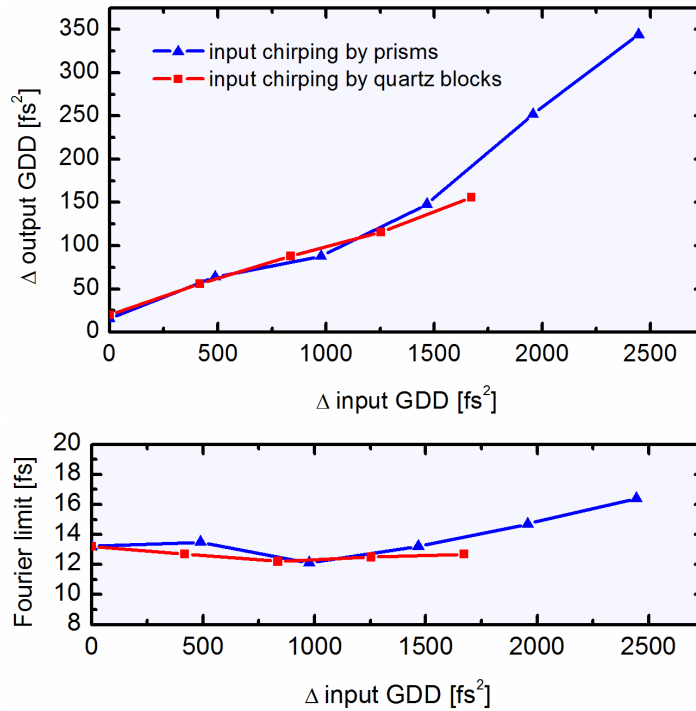

Figure 2.7: (a) output GDD measured by maintaining the spectral bandwidth (b)

---

[2]Calculating the Fourier-limit in parallel during the measurement one can avoid such deviations.

of the input chirp appears in the chirp of the output pulse. The calculated GDD ratio, see Fig.2.8, shows that only around the 9th part of it has to be compensated and that this ratio stays constant over the input chirping range. Shown too in Fig.2.8 are two further GDD ratios
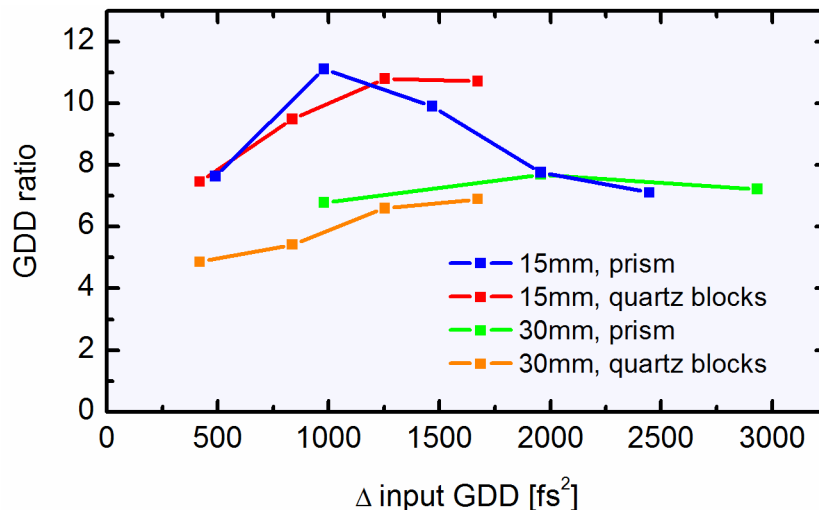

Figure 2.8: GDD ratio measured by maintaining the spectral bandwidth, see text for details.

(orange and green) using a 30mm long LMA-25 with a Fourier-limit between 11fs and 12fs. The comparison between the 15mm and 30mm case is interesting as 30mm is slightly longer than the optimal fiber length for our pulse compression. Because one could have expected some saturation effects (see section 3.3) in the spectral broadening which could have shown up in the GDD transfer. However we notice from Fig.2.8 that the GDD transfer stays constant as well. Probably we have not yet entered the saturation regime with our input parameters (see section 3.3). The GDD ratios of the 30mm case is slightly under the 15mm case as we didn't got the Sellmeier coefficients for calculating the GDD of one lens (material EC0550) even contacting several companies. In reality these two curves would be slightly higher.

The presented results are very important for the concept of chirped pulse compression, where one couples, under maintaining the spectral bandwidth, more energy into the fiber due chirping the input pulses. Fig.2.8 facilitates strongly now the compression part of our concept. In addition, the presented results allows to predict the amount of GDD to compensate for.

2.3.3   GDD ratio under constant input energy

In a second experiment we investigated the GDD ratio when the input chirp was increased but the input energy was kept constant. As in the last experiment, the spectral broadening and pulse compression of the Fourier-limited input pulses serve as reference point. Increasing now the input chirp leads to a decrease of the broaden spectral bandwidth as we due not compensate the longer input pulses with more energy to keep the spectral bandwidth. In Fig.2.9 we plotted the measured GDD ratio (black line) and compared it directly with the measurements presented in the last subsection. As fiber we used a 15mm long LMA-25. A clear decrease of the GDD ratio is observed, contrary to the above presented results. It would be interesting to see the behavior of the GDD ratio when using even a stronger input chirp. If it would stay at the measured constant GDD ratio value or falling beneath it.
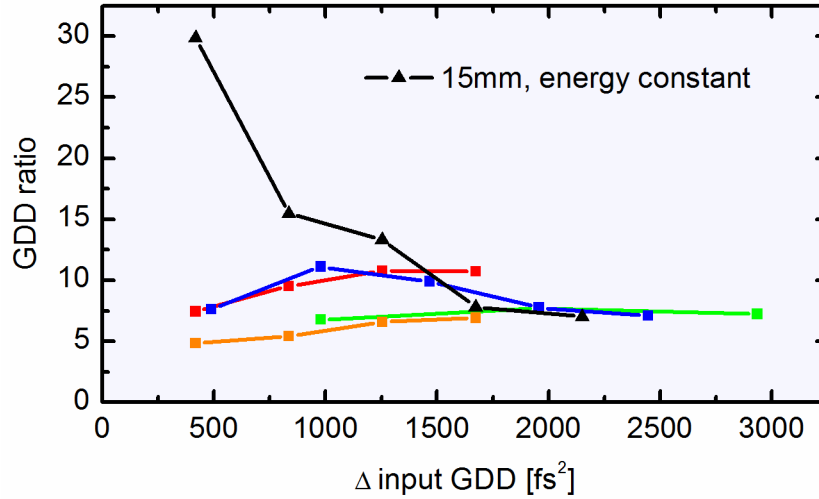
Figure 2.9: GDD transfer under maintaining the input energy (black line); other lines from Fig.2.8 for comparison

2.3.4 Ongoing considerations about the GDD transfer

We are not aware of any publication which mentioned this issue of dispersion transfer, respectively GDD ratio, in detail, either by experiments, theory or simulations. Our preliminary measurements show some trends but for a satisfactory explanation we would require more experimental data. Thereby, one important experiment is the GDD compensation when increasing the input energy (and therewith the spectral broadening) for Fourier limited input pulses and chirped ones. Our measurements are presented in Fig.2.3.4, with (a) the Fourier limited case and (b) the chirped case, twice using a 2.9cm long LMA-25 fiber with a transmission of approximately 87%. Note that the pulse durations is the measured one and not the calculated Fourier-limit. As clearly seen in both cases, the GDD amount to be compensated
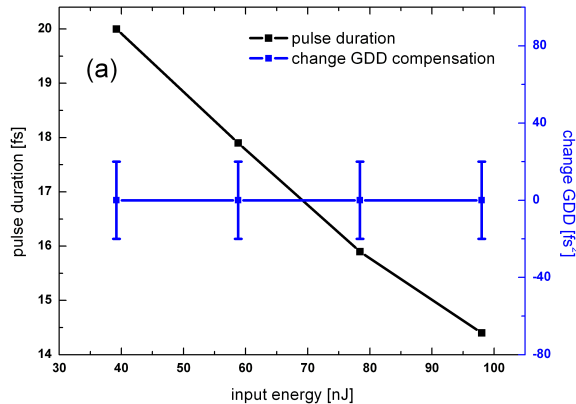
stays constant when the input energy, and therefore the spectral bandwidth, is increased. Furthermore, it is interesting that the amount of GDD to compensate was approximately the

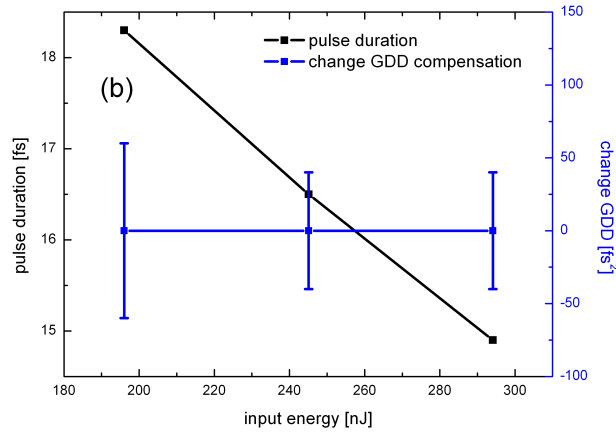Figure 2.10: Change of GDD compensation if the energy is increased for (a) the Fourier limited case and (b) the chirped case.

one of the material's GDD of the fiber ($\pm 3\%$). These measurements have been confirmed too in [32] using a fiber amplifier at 1030nm wavelength as laser systems.

It is to early and beyond the scope of this subsection to present a satisfactory explanation of the GDD transfer. Nevertheless, we will discuss an often suggested explanation, namely that the increased spectral bandwidth is responsible for the GDD transfer. Thereby, one assumes that the input pulse maintains its pulse duration but will be spectrally broaden. The chirp will than be spread over this larger spectral bandwidth resulting in a smaller GDD value to compensate. However, this model does not fit to the experimental data. According to this model, a different strong spectral broadening will lead to a different amount of GDD compensation. But this is in contradiction to the data shown above and in [32]. Furthermore, in respect to our experimental data this model results in a GDD ratio of 3, but we have measured a GDD ration between 7 to 10. It is also not clear how this model can explain the presented data measured in 2.3.3.

Current data do not allowed a final explanation, but there is a tendency that only the increased spectral bandwidth is not sufficient to explain the GDD transfer, respectively GDD ratio. Other, not yet clear identified, mechanisms seem to be significant too. Input chirp, spectral bandwidth and input energy, they all seem to be related to explain the GDD transfer.

2.4   Conclusions

With the introduced concept of chirped pulse compression we demonstrated successfully how to overcome the self-focusing threshold, by maintaining spectral broadening and compressed pulse duration with significantly more output energy. Increasing the input energy we found no indications of other effects that could limit chirped pulse compression. Therefore, we believe that our concept can be scaled into the μJ range when using improved chirped pulse oscillators [44]. Furthermore, reaching the sub-10fs regime by optimizing all parameters should be very feasible. Thereby, the pulse compression is supported through the surprising observation that only a small fraction of the input chirp has to be compensated in the output. This enables us

to chirp the input pulses extremely without significantly changing the compression setup. Our concept should be applicable to all such pulse compression schemes where self-focusing poses the current limitation. We expect for example direct benefits for Yb based laser systems [36,49] or hollow core fiber compression setups [17,18]. With the presented output values for chirped pulse oscillator we are in the same range as current MHz-NOPAs experiments [37–39], but with a much less complex setup and better stability. The combination of chirp pulse compression with a chirped pulse Ti:Sapphire oscillator presents a very interesting alternative for scientists in ultrafast spectroscopy, high harmonic generation or material processing.

Chapter 3

Characterization and few-cycle pulse compression

With a proof-of-principle experiment we have demonstrated the concept of chirped pulse compression. This chapter addresses on the one hand some physically interesting issues and on the other hand aspects relevant for daily applications in further experiments. We first explore the possibility to extend the spectral broadening and compression into the few-cycle regime (section 3.1) as well as investigations about the spectral broadening expansion (section 3.2) and circular polarization (section 3.3). Afterwards, we address the issues of polarization ratio (section 3.3), stability (section 3.4) and fiber damages (section 3.5) relevant for daily operation. Section 3.6 is devoted to the group delay dispersion characterization of chirped mirrors by white-light interferometry, which is essential for successful pulse compression. A brief summary and conclusion are given in section 3.7.

3.1   Pulse compression to 6fs and beyond

Chirped pulse compression is able to reach 10fs with the full available energy of a chirped pulse oscillator. Even 9fs spectral broadening has been demonstrated. But for experiments concerning carrier envelope phase effects, or isolated attosecond pulse generation, it is preferable to have few-cycle pulses. At kHz repetition rate such, pulse durations are routinely achieved with several hundreds of μJ pulse energy by self-phase modulation in gas filled hollow core fibers and input pulse durations of around 25fs [17, 18]. At MHz, experiments have demonstrated sub-6fs pulse compression in solid core fibers [47, 48], even 4fs pulses have been shown [48]. But in all these experiments the input pulse duration was already very short, 13fs respectively 9fs, which is currently not accessible directly from a Ti:Sa chirped pulse oscillator. The compressed pulse energies were not higher than 3nJs and the pulse compression setup stayed on a proof-of-principle level, even though an application is shown in [53]. In 1988, a pulse compression from 45fs down to 6fs in fibers on kHz has been shown [46], but with a central wavelength of 600nm which supports stronger spectral broadening as on 800nm (see section 1.2). Hence, the first critical question for us is if one can reach the 6fs scale at 800nm with 55fs long input pulses in one pulse compression stage, or if two fiber and compression stages are necessary. And secondly, how much output energy will be available, respectively is sufficient for further applications.

In our experiment we used a commercial LMA-5 fiber from (www.nktphotonics.com) with

a mode field diameter (MDF) of 4.2μm and a zero dispersion wavelength at 1.2μm. The smaller MDF generates a higher intensity compared with the LMA-25 earlier used, which results in a larger spectral broadening. The fiber is not polarization maintaining and is loosely placed in a V-groove of the fiber holder. After the fiber, the compression is done by home-made complementary double chirped mirrors (see 3.6), quartz plates and quartz wedges for fine tuning. The chirped mirrors are designed for an angle of incidence of 7° and a bandwidth from 550nm to 1200nm with -30fs^2 per reflection. Third order dispersion compensation is included in the design. The pulse duration was measured by interferometric autocorrelation with a commercial 5fs autocorrelator from Femtolasers Produktions GmbH.

In a first proof-of principle experiment we used a 1.95cm long LMA-5 with 30nJ of input energy and 55fs input pulse duration. Fig.3.1 shows the achieved spectral broadening (a) and compression (b). With a transmission of 60% corresponding to 18nJ we compressed the pulses to 6.1fs which is close to the spectrum's calculated Fourier-limit of 5.8fs. For com-
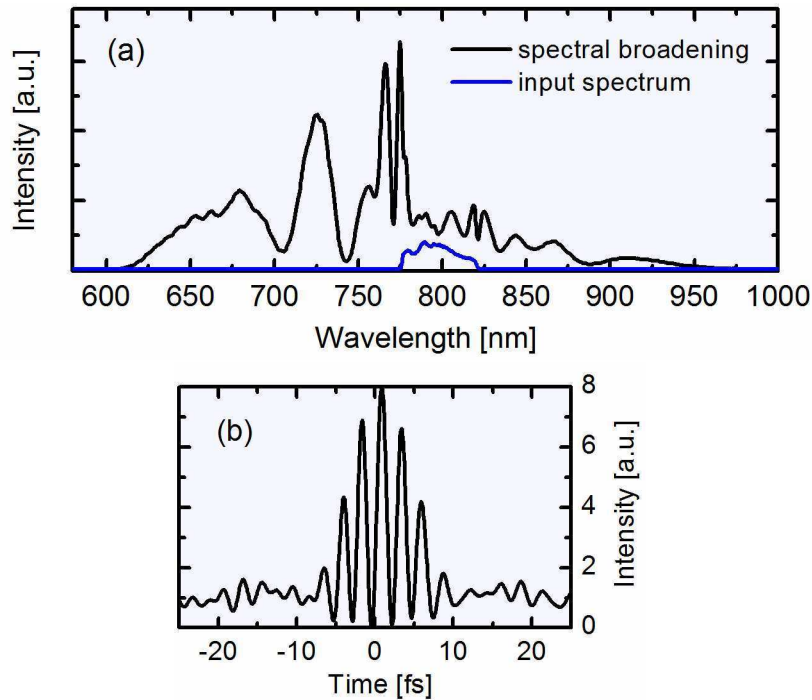

Figure 3.1: (a) 6fs spectral broadening and (b) measured autocorrelation

pression we used 24 reflections on the chirped mirrors and 45mm of quartz as well as 4.5m of air path (=95fs^2 GDD) have to be considered. Measured and calculated autocorrelation show good agreement, see Fig.3.2. The side maxima are an inevitable result of the spectral shape. Evident from the typical spectral shape, the dominant process for spectral broadening is self-phase modulation influenced by group velocity dispersion. Optical wave breaking [9] appears between 600 and 700nm. The large peak between 700 and 750nm is not yet fully understood and can also disappear if other conditions are used (see Fig. 2). The transmission can be probably increased by a more suitable focusing onto the mode field area, which was not optimized in our case. The spectrum was stable over several hours.

This proof-of-principle experiment demonstrates that it is possible to reach 6fs pulse duration starting with 55fs input pulses from a commercial chirped-pulse oscillator with a compact
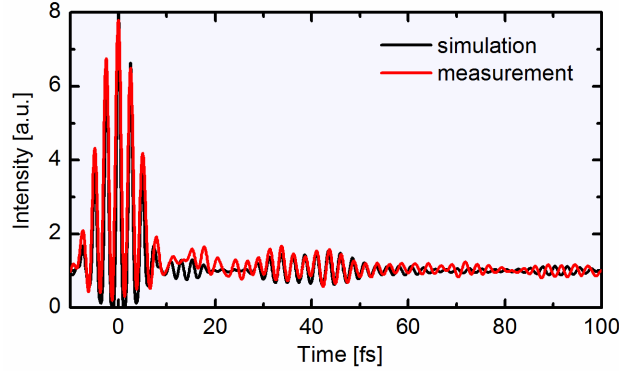
Figure 3.2: Comparison of the measured and simulated 6fs autocorrelation

setup. We restricted the input energy to only 30nJ to be on the safe side during our measurements. Nevertheless, 15nJ of pulse energy was finally available, which is already 3 times more than in ref [47] using chirped mirrors (at 1MHz). However, we can still increase the energy. In Fig.3.3 we present spectral broadening in a 2.7 cm long LMA-5 with an input energy of 76nJ, resulting in 40nJ of output energy. The Fourier-limit was calculated to 5.3fs. The spectral broadening shows the same shape as shown in Fig.3.1 which makes compression straightforward. Focusing the pulses down to a $\sim 3\mu$m diameter spot will result in a
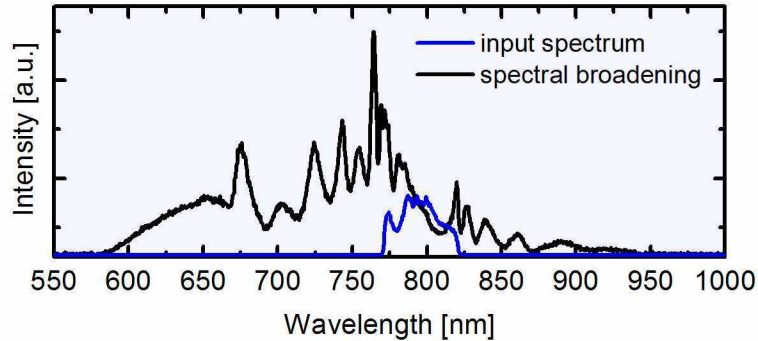
Figure 3.3: Approaching 5fs with 40nJ of output energy

peak intensity of $10^{14}\frac{\text{W}}{\text{cm}^2}$ which would allow high harmonic generation. More energy can be coupled if one uses the concept of chirped pulse compression [50]. Furthermore, using larger mode field diameter fibers like LMA-8 or -10, more energy can be coupled into the fiber before self-focusing starts. The reason is that self-focusing is to a certain degree dependent of the numerial aperture of the beam. Changing the core diameter or the beam diameter of the input beam will change the numerical aperture. The spectral broadening will be slightly smaller but still allows Fourier-limits of 6fs. The optimal combination of core diameter, output energy and pulse duration has not yet been investigated but also depends on the desired further application field.

3.1.1   Near-future applications: Ultrafast spectroscopy at MHz for solar cells

An interesting application of our 6fs laser system at MHz repetition rate could be ultrafast pump-probe spectroscopy of photoinduced electron transfer samples, respectively solar-cells. These kinds of samples require an energy density of only $1\mu J/cm^2$ [1]. Current setups are using commercial kHz laser systems with around 30fs pulses [54]. In order to resolve certain physical processes [55], it would be desirable to have 6fs pulses. Furthermore, to reduce the measurement time and to increase the signal to noise ratio one would like to have the laser system operating at MHz repetition rate. From our 500nJ chirped pulse oscillator we can generate a 6fs probe beam with a sufficient energy density as well as the probe by white light generation in a YAG crystal, directly from the 55fs long output laser beam. One point which is not yet clearly answered is the damage threshold of these samples concerning the average power density. Solar-cells are made for the intensity of the sun, respectively a power density of 1366 W/m^2. Quite often the damage threshold of the solar-cell is at least a factor 10 higher. Working at 5MHz with a focus generating $1\mu J/cm^2$ will result in a power density slightly above the damage threshold. However, setting down the repetition rate to 1MHz using a pulse picker and optimizing the focus diameter, respectively decreasing the energy density one should come below the sample's damage threshold. Ultrafast spectroscopy with solar-cells is a very interesting and important research field. Therefore we drew your attention to the benefits which our laser system with pulse compression offers to this research field.

Other direct applications can be high harmonic generation (HHG) [40], HHG with resonant plasmonic field enhancement [41], material processing and waveguide writting [56], as high energy seed for succeeding OPCPA schemes, or ultrafast single electron diffraction experiments [57]. The current technique should also be able to compress the chirped pulse oscillator presented in Ref [58] which works at 70MHz with 62nJ and approximately 30fs pulse duration to (hopefully) 6fs. If we assume a final transmission of (only) 50% we still would have 30nJ of useable output energy for further experiments, which is around 6 times more as commercial oscillators currently generate at the same repetition rate. We believe that the combination of a commercial oscillator with such a simple pulse compression setup for 6fs makes it attractive for many research groups.

3.2   Evolution of spectral broadening

Spectral broadening with 55fs input pulses is on the border between pure self-phase-modulated spectra and beginning influences of other effects [1]. Furthermore the strong peak intensity will lead to saturation effects which was not yet reached in earlier experiments. Analyzing the spectral broadening expansion when increasing the input energy should allow us conclusions about such effects and therefore an optimization of our setup. We are not aware of a published systematical investigation addressing these points.

In the following experiments we recorded the spectral broadening of a LMA-25 when increasing the input energy. We used two different fiber lengths, 2.5cm and 4.0cm. For each length we recorded the spectral broadening for input pulse durations of 110fs respectively 190fs, measured using a GRENOUILLE (Model 8-9 USB; Swamp optics). We have chosen the chirped case to detect a possible influence of the average power more explicitly. For a

---

[1]a higher energy density leads to unwanted effects

clear visualization of the spectral broadening we plot the analysis curves as shown in Fig.3.4. The difference between the FWHM points of the broadened spectrum one minus those of the original one plotted against the input power. In doing so, we differentiate between the visible part (VIS) and near-infrared (NIR) part. In Fig.3.5 we show the spectral broadening
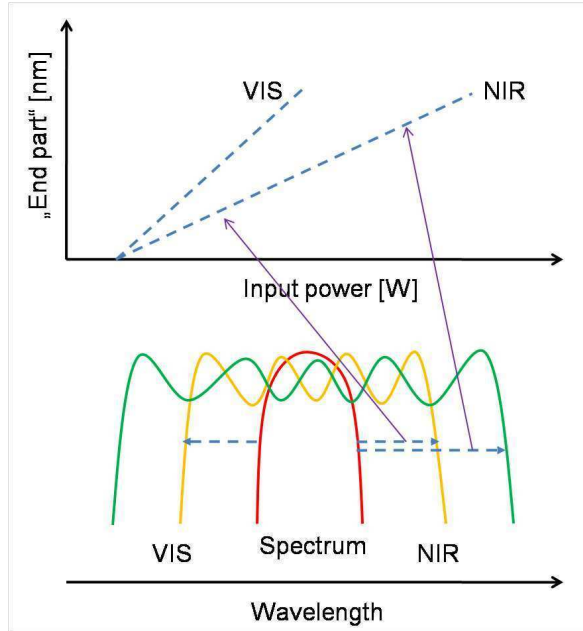

Figure 3.4: principle

expansion (VIS and NIR) of a 4.0cm long LMA-25 with 110fs long input pulses. Both develop approximately linear with the same slope but later the VIS part starts saturating. A weak saturation in the NIR is observed as well. Interestingly, the VIS always shows a bend whereas the NIR stays clearly linear for longer time. It seems that two different regimes of the spectral evolution exist. Furthermore, at a higher input power, oscillations appear which are present in both parts. In all measurements these oscillations never show up in the linear part. Therefore we do not attribute these oscillations to external reasons (laser) but to a combination of fiber, saturation and self-phase modulation behavior which is not yet fully understood. The average power (and with it thermal reasons) can be excluded as the oscillations do not appear at the same input power when using 190fs input pulses. The shown behavior in Fig.3.5 is typical for the other experimental conditions as well. Comparing the development when using different fiber lengths we noted a surprising fact, shown in Fig.3.6. The shorter fiber results in a stronger spectral broadening concerning the VIS. This behavior is reproducible and was observed for the 190fs case too. For the NIR part (Fig.3.7, 110fs input pulse duration) we do not observe such a behavior. Concerning the VIS part this is a quite surprising observation as it is contrary to the outcome predicted by (simplified) theory. This indicates that one has to use already a more accurate theoretical description [1]. Searching the effect behind this saturation process in Fig.3.8, we compare the spectra generated by input pulses of 240nJ and 110fs, using a LMA-25 fiber length of 2.5cm respectively 4.0cm. The spectra are similar. Comparing the VIS and NIR part we notice that the NIR does not exhibit a spectral feature seen in the VIS part (A). The effect behind is called optical wave-breaking (OB) [9] and happens if frequency-shifted light in the leading and trailing edges of a pulse overtakes unshifted light
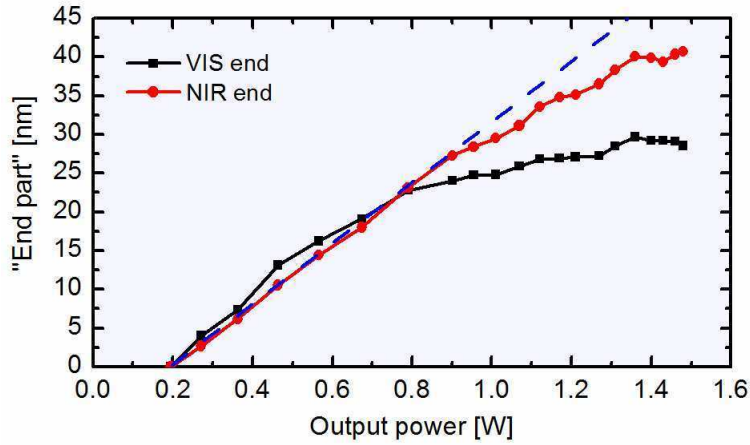
Figure 3.5: Spectral broadening expansion with saturation in the VIS for 110fs long input pulses in a 4.0cm long LMA-25
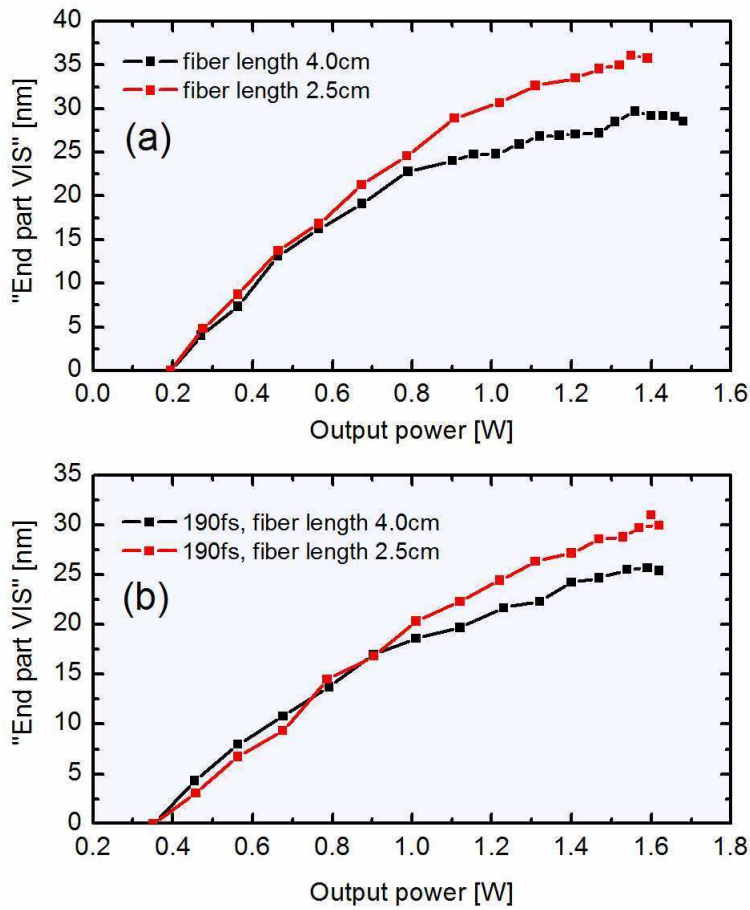

Figure 3.6: Comparing the VIS spectral expansion using different fiber lengths with (a) 110fs and (b) 190fs input pulse duration.
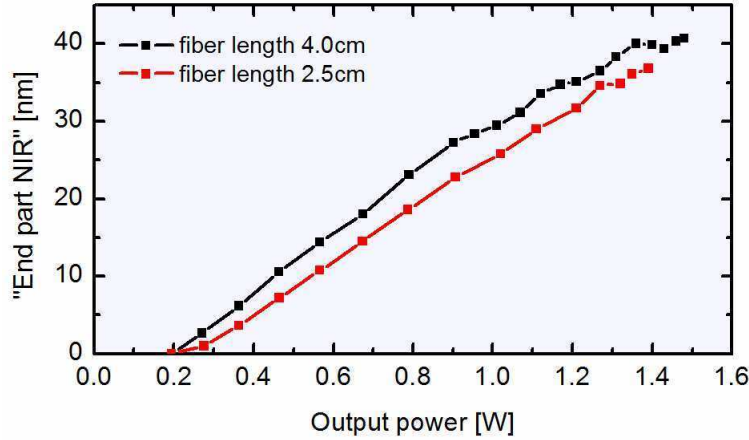
Figure 3.7: Linear spectral expansion for the NIR part with 110fs input pulse duration
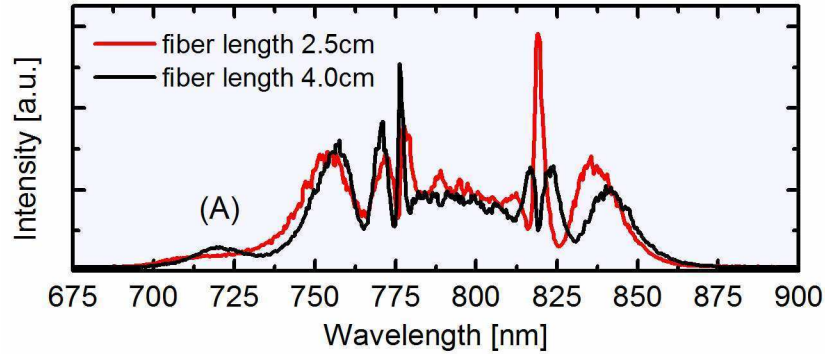

Figure 3.8: Comparison of spectra using different fiber lengths but same input energy

in the pulse tails. Mixing of these overlapping frequency components generates sidelobes on the pulse spectrum. Normally it appears on both ends simultaneously. Optical wave-breaking can be described by the nonlinear Schrödinger equation. Comparing the OB of the different fiber lengths we notice that the OB of the longer fiber is much further advanced as the one of the shorter fiber. Therefore we assume that the OB process is responsible for the shorter VIS part. Consequently, the VIS should be larger before OB appears and later decreasing back. A simulation should confirm this. In Fig.3.9 we simulated the spectral evolution using a 4.0cm long LMA-25 with 240nJ of input energy and 77fs long input pulses. The simulation has been done with the program used in [7]. The shown spectra are taken at different lengths in the fiber, namely after 5, 10, 25 and 40mm. To stress the effect more clearly, we have chosen input pulse duration of 77fs instead of 110fs. One clearly observes how the self-phase modulation spectrum decreases as soon as the OB starts. With the simulation we have identified the process behind our observation. But why it starts to decrease has not been fully understood. We are not aware of a publication addressing this question even there are some articles published on OB [59]. We notice that optical wave-breaking stops respectively decreases the spectral bandwidth generated by the pure self-phase modulation process. Nevertheless, in total, the spectral broadening still grows due the contribution by OB which results then again in a shorter Fourier-limit of the pulse. The question is now if
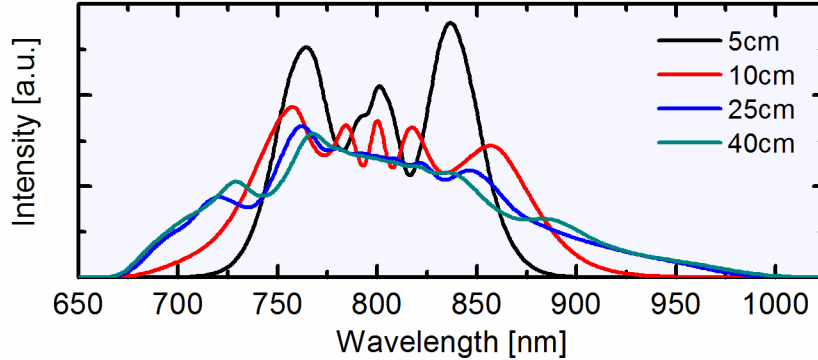
Figure 3.9: Spectrum simulation using different fiber lengths

we still can compress such a pulse dominated by OB. To avoid long discussions we refer to section 3.1 where the 6fs spectral broadening is also strongly influenced by OB but we were able to compress the pulse close to its Fourier-limit.

A detailed analysis of the spectral broadening can help to identify and to understand many ongoing processes. We have shown only one example of optical wave breaking which dominates over the self-phase modulation. Another interesting aspect would be to clarify why we do not yet see OB in the NIR part. This would allow to draw conclusions about the input pulse shape which strongly influences the spectral broadening [59].

3.3 Comparison of linear and circular polarization

Circular input polarization will change differently the refractive index compared to the linear case [60]. In an isotropic material, depending upon the nature of the physical mechanism leading to the nonlinear refractive index, the ratios are given, with $\Delta n = n_2 I$, by

$$\frac{\Delta n_{\text{linear}}}{\Delta n_{\text{circular}}} = \left\{ \begin{array}{cl} 4 & \text{for molecular orientation} \\ 3/2 & \text{for nonresonant electronic nonlinearity} \\ 1 & \text{for electrostriction} \end{array} \right.$$

. The relevant physical mechanism in our experiment is the nonresonant electronic nonlinearity. Therefore, circular input polarization should generate a 33% weaker change in the refractive index change as compared with linear input polarization. Consequently, one should be able to couple 33% more energy into the fiber before the material undergoes self-focusing. Detailed discussions and calculations are presented in [60]. With a 1.9cm long LMA-25 fiber we increased the coupled energy around 31% using circular input polarization. This is close to the theoretical limit. However, essential for further use of the beam is the aspect of how good the circular polarization can be transferred back to the linear polarization after spectral broadening. To do so, we measured the polarization ratio, after the circular polarization has been changed back to linear one, using a polarizer and recording the maximal and minimal transmission. The polarization ratio is then calculated by maximal transmission divided by minimal transmission. Fig. 3.10 shows the results, including the polarization ratio of the linear input polarization after the fiber (black curve). The ratios are only measured for the unchirped case. However, one point for the chirped case with linear input polarization is presented too. It is obviously that both ratios decrease with higher power but still with a
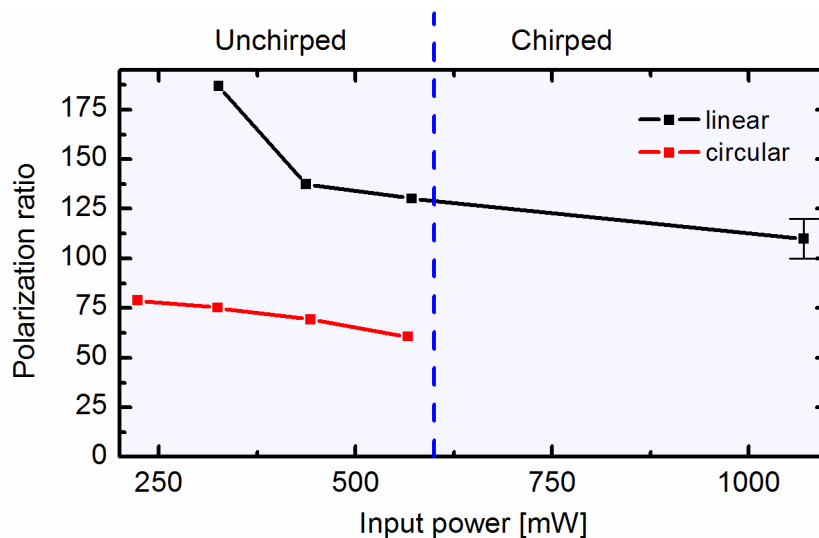
Figure 3.10: Linear and circular polarization ratio

ratio of around 65 for circular and 130 for the linear case, good enough for further applications. At higher average input power we think that the ratio will drop slightly further but from our experiments we know that it does not do so dramatically. Note that we used non-polarization-maintaining LMA fibers. The circular ratio probably increases slightly if $\lambda/4$ plates designed for the full spectral bandwidth are used. Recording the spectrum after the polarizer we observed that all spectral parts have the same polarization. The same fiber transmission for both cases was achieved.

Using the small core LMA-5, we observed a rotation of the linear output polarization depending of the azimuthal orientation of the fiber's photonic structure to the linear input polarization. No significant influence to the spectral broadening, transmission or polarization ratio decrease was observed. We didn't had the time to perform a detailed measurement with a precision fiber rotation setup. However we found that the maximal shift is around $30°$, which is the half of $60°$ of the angles in the hexagon. The correct input polarization for the chirped mirrors can be simply set by placing a $\lambda/2$ plate in the input beam.[2] With an LMA-25 we have not observed a similar behavior. This can be explained by the fact that for LMA-25 the mode field area is much closer to a circular, compared with the LMA-5 which has a hexagon mode-field area.

In summary we have shown that circular input polarization is a suitable method to increase the coupled energy by about 33% and that back-transformation to linear polarization is possible with a good polarization ration of 65, which is usually enough for further experiments.

3.4 Long term stability and pulse-to-pulse fluctuations

The stability of the laser system presents an essential issue for ultrafast spectroscopy and time resolved pump-probe experiments. Depending on the experimental conditions, the laser system has to be stable from seconds to days. Concerning our planned application of chirped

---

[2]Due the smaller bandwidth of the input beam it is preferable to place the $\lambda/2$ plate there, to assure the same linear polarization over the full spectral bandwidth.

pulse compression for ultrafast single electron diffraction at MHz repetition rate, the laser system has to be stable for at least a day. The diffraction pictures typical exposure times are in the order of tens of seconds. Therefore, a full time resolved characterization of a sample requires several hours or even days. Note that the demand on the stability depends on the sample requirement, as well as of the pump-probe setup. Quantifying the stability of the laser system we have to measure the long term behavior of the spectral broadening respectively compressed pulse duration, pulse-to-pulse energy fluctuations and beampointing.

The long term stability we express by recording the Fourier-limit calculated of the spectra taken every 30 seconds (exposure time 100ms). This is a more representative way as recording the output power. Because small changes in the spectrum will change the compressed pulse duration but the changes in the measured output power are to small to detect it. Consequently, we wouldn't record any pulse duration changes when the output power is recorded. Therefore it is more suitable to monitor the spectral broadening, respectively the Fourier-limit. In Fig.3.11 we measured over one hour the spectral broadening of chirped pulses with an input energy of 286nJ (1.43W) in a 3 cm long LMA-25 with a transmission of 88%. The LMA-25 was lying freely in the homemade V-groove fiber holder. No kind of cover, fiber stabilization or input beam alignment system was used. An excellent stability over at least one hour is
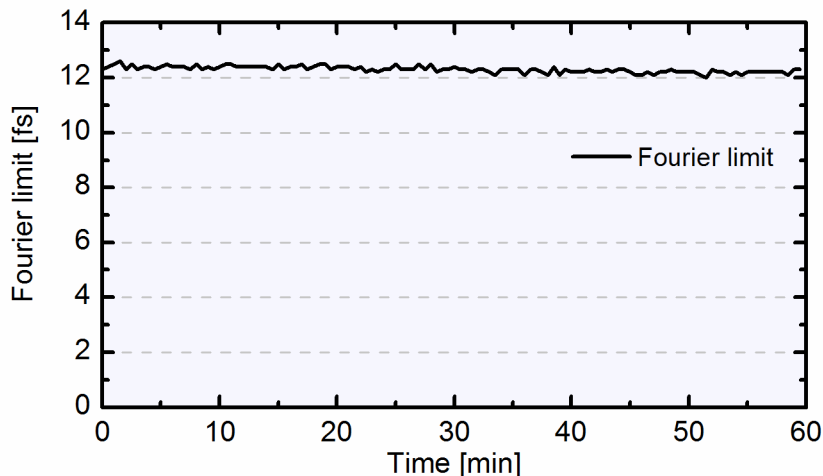
Figure 3.11: Long term stability over 1 hour

shown with a Fourier-limit stable at 12.3fs ±0.1fs. We have found that the fiber will show no degradation, ablation or other kind of damages if the input power is set 10% under the self-focusing threshold. Furthermore, Fig.3.11 demonstrates the mechanical stability of the fiber holder, because any drift would have changed the input coupling and therefore the spectral broadening. The same argument holds for thermal aspects. We will see later in chapter 4.2 that a much higher average power is required for thermal effects.

The spectra were recorded for only 1 hour, but also we didn't observed a significant spectral change over hours. For a measurement over one day one should in parallel monitor the temperature and pulse duration of the laser to identify artifacts through a change of the laser input pulse duration. Fig.3.12 shows a measurement of the temperature at the laser case and the SHG power. The change of the SHG power corresponds directly to a change of the input pulse duration. Not shown is the fundamental power (approximately constant). Small temperature changes, caused by the air-conditioner, influence the pulse duration of
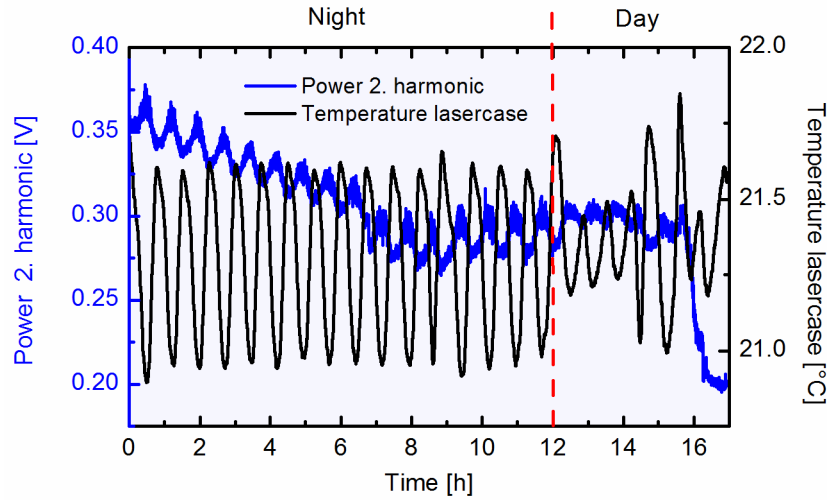
Figure 3.12: Temperature stability at the laser case

the chirped pulse oscillator (note that the cavity length is 48m, folded in a Herriott-cell). Furthermore, day and night time can be clearly distinguished. Such fluctuations will disturb the laser´s operation. For a correct one day measurement of the spectral broadening one has to consider these influences as well. Note that in the meantime the temperature stability has been improved.

Considering the pulse-to-pulse energy fluctuations of the fundamental and the spectral broadened beam were recorded using a UPD-300-SP (from Alphalas) and a ET-4000F (from Electro-Optics Technology, Inc.) photodiode. After this, we integrated over the red marked pulse area in Fig 3.14. The standard derivation (SD) over 1000 shots has been found as 1.48%
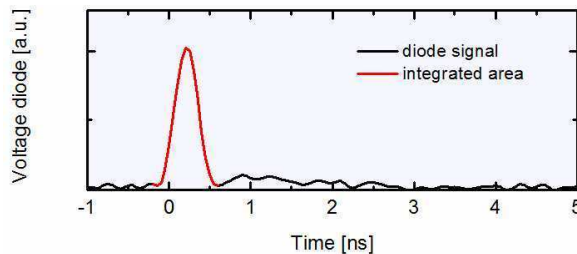
Figure 3.13: Photodiode signal

for the laser and 1.25% for the spectral broadening. The SD after the spectral broadening is comparable with the laser and guaranties a stable pulse train. The observed small dip at count 400 in the figure does not coincidence with the laser. Probably the coupling has slightly changed due external influences. Fixing the fiber (currently it is just lying) and a small cover box against airflow might avoid such dips and improve the pulse-to-pulse fluctuation further.

For the spatial stability we recorded the beampointing with a beamcamera (WincamD-U) before and after the fiber in the same distance and beam diameter to compare directly. We took 1200 points, 1 point every second. Fig.3.15 compares the beampointing of the laser (A), after the fiber (B) and after the glued fiber (instant adhesive) onto the fiber holder (C). All
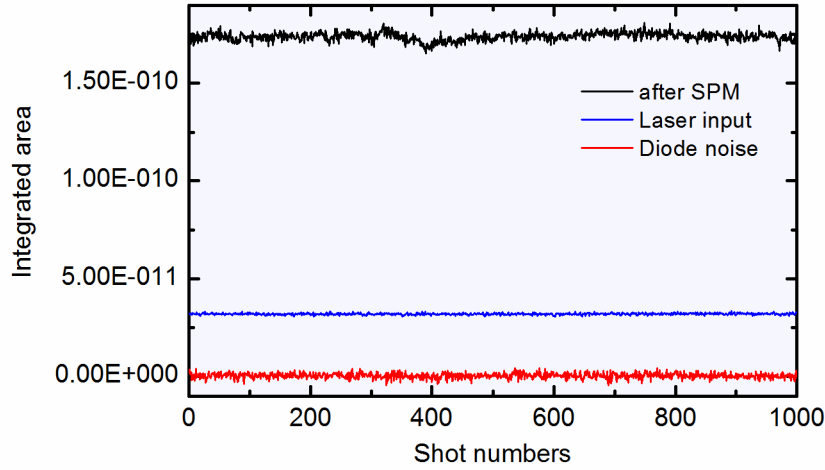
Figure 3.14: Pulse-to-pulse fluctuations

given data points corresponds to the centroid of the beam profile. Note that the large lateral displacement in all cases results from the oscillator due temperature fluctuations which have deformed the cavity. This problem has been solved in the meantime. It is interesting to see that the laser beampointing has been maintained to a certain fraction after the fiber. The small rotation of the beampointing can be explained by a small angle of the output surface resulting from the cleave, which deflects the beam always a bit. Changes of the transmission during the measurements were negligible. Analyzing the beampointing one recognizes that
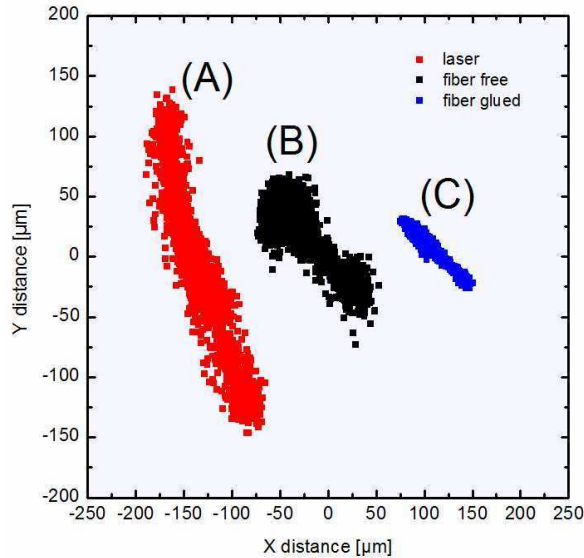
Figure 3.15: Beampointing comparison of the laser (A), after the unfixed fiber (B) and glued fiber (C)

(A) and (B) are staying in the same range but the glued case (C) is smaller by approximately a factor 4. We assume that the pulse-to-pulse fluctuations in case (C) will be improved too as one avoids small external perturbations acting to the input coupling. Note that a beam

alignment system after the fiber can correct all drifts. Depending on the path length from the fiber to the sample chamber, such a system will be necessary.

Finally we briefly address the topics of reproducibility and dirt concerning the fiber's surfaces. Replacing the fiber through a new one, one may think that the quality of the surface given through the cleave is a critical point for achieving again the original spectral broadening and transmission. We found that this is not the case. The fiber surface does not require any high demands to the cleaving process. Therefore a high reproducibility is achievable. Note that changing the fiber including alignment can be done in less than 15 minutes. Concerning dirt particles of the air we didn't protected the fiber surface by a case or flushed it continuously with cleaned air [47]. In none of our experiments we observed a damage which we would attribute to dirt particles from the air. Contrarily, the same piece of fiber has been used for 2, 3 weeks without any kind of notable degradations. We believe that the fiber can be used for even much longer times.

3.5 Kinds of fiber damages

Even we can operate in a power regime where no damages occur, it is helpful and necessary to briefly address the topic of damages of the fiber. Self-focusing represents the most frequently observed damage in our case as simply the input peak power was too high. The transmission drops dramatically to around 25% of its original value and a bright scattering point is observed few millimeters away from the input surface. The distance is in agreement with the self-focusing length. Cutting away this small piece of fiber, we have again a self-phase modulated spectrum with its original transmission. This shows that only the input region got damaged by self-focusing. Examining the damaged spot with an optical microscope we couldn't see any damages in the waveguide or cladding. Using a differential interference contrast modus of an optical microscope one can probably reveal some damages.[3]

During our chirped pulse compression measurements we have observed that if the input power is slightly set under the self-focusing threshold (-5%), the fiber sometimes undergoes self-focusing after a certain time. This can happen in minutes or hours. The mechanism behind is not fully understand but probably it is an interaction of different factors like thermal properties, jacket removing, cleaving, air-condition, laser pulse duration stability, etc. However, we didn't analyzed it in detail as staying around 10% under the self-focusing threshold will avoid this problem.

A different kind of damage to the fiber surface happens through the use of aceton, which was long time not recognized. Aceton is used for removing the jacket of the fiber, which can be also done by mechanical stripping or warming up the fiber with a hairdryer. Normally, the fiber lies in an aceton bath for not more than five minutes as otherwise the core and cladding will change their properties (e.g. a more soft stiffness). During this time, the fiber's cladding holes act like a capillary and the aceton gets sucked into the holes, sometimes distributed over the whole fiber length and evaporating only very slowly (staying for days if not used). If we couple now into the fiber, the aceton tends to come out of the fiber, covering continuously the input and output surface. One can see this as the beamprofil gets blurred out. We noticed that the transmission is around 2% less if the jacket was removed with aceton, compared to the mechanical stripping. Furthermore we noticed that the long term behavior of the fiber seems to be different as well. Working close to the self-focusing threshold the fiber undergoes

---

[3]private communication with the Fraunhofer-Institute of Lasertechniques ILT

faster self-focusing. It is therefore recommended to remove the jacket mechanically.

A frequently asked question concerns the fiber surface quality after the cleave process in regards to the input damages. Therefore, we inspected the surface with an optical microscope and noted its transmission in the experiment. We observed that as long as the core is not covered with flinders from the cleaving process the fiber will work fine. Such a cleave does not require any special preparation, making it reproducible and feasible for everyone.

Finally, we have to clarify if ablation has to be considered or not. Following [61] we approximate a damage fluence of 3 J/cm^2 for fused silica with 50fs pulses. Calculating the fluence of a LMA-25 fiber with 500nJ and 50fs we find a fluence around 20 times less than required for ablation, for a 100nJ pulse it is 100 times less. Concerning the LMA-5, used in the 6fs experiment we calculated for 100nJ and 50fs a fluence which is only 4 times less. Hence for 500nJ we are approximately around the damage fluence. In our 6fs experiments we stayed always under 100nJ of input energy. Therefore we assume that ablation has not yet appeared.

Chirped pulse compression with μJ input energies should be feasible, concerning the mentioned kinds of damages. Other damages like multi-photon absorption will only appear on much higher input energies.

3.6   GDD characterization of sub-10fs chirped mirrors

Accurate dispersion engineering is an essential part for the generation of sub-15fs pulses. Thanks to the concept of chirped mirrors the possibilities of the dispersion management for arbitrarily shaped higher-order dispersion have been increased significantly. In parallel, the complexity of the compression setup was reduced dramatically. The basic idea of a chirped mirror is its wavelength dependent penetration depth. To do so, a chirped mirror consists of dielectric multilayers, structured in the way that the reflections at the index discontinuities add up constructively for the Bragg wavelength. If the optical thickness of the layers along the mirror structure is varied, then the Bragg wavelength depends on the penetration depth. Any imperfections of the impedance matching, mainly between the first layers and the ambient medium (normally air), results in a periodic spectral phase modulation (called dispersion ripples) which leads to pulse distortion [62]. With the development of so called double chirped mirrors (DCM) [63], in combination with a broadband antireflection coating, the pulse distortion has been significantly decreased and enabled numerous applications in research. Unfortunately, DCM only allow a bandwidth of 300nm in the Ti:sapphire region. Extending the bandwidth to an optical octave has lead to new concepts like the complementary DCM [64], and double angle chirped mirrors [52], where one has designed a mirror pair with cancelling dispersion ripples. Another approach is the concept of Brewster angle chirped mirrors [65]. Nowadays, the different concepts of chirped mirrors have lead routinely to 5-7fs oscillators as well as sub-5fs pulses using different pulse compression techniques. Further details about chirp mirrors and their different concepts are given in [62].

During the manufacturing process the demands to the layer coating accuracy are very high. Therefore, an efficient dispersion management requires to measure the used chirped mirrors, to avoid any irregularities in the produced group delay dispersion (GDD) curve of the chirped mirror. In this section we present our results of the GDD curves of our chirped mirrors, which have been characterized concerning following points:

- Dispersion ripples of different chirped mirrors concepts

- Input parameters accuracy (angle of incidence and polarization) for correct handling

To our knowledge no systematical study has been published, even of course GDD measurements of several chirped mirrors were presented in earlier publications. For characterization we used a white-light interferometer together with a Fourier-transform spectral interferometry algorithm to analyze the data [66]. We have measured the 10fs double angle chirped mirrors, used in section 2.2, as well as the 5fs complementary chirped mirrors from section 3.1. These chirped mirrors have been produced in our group by Dr. Volodymyr Pervak. Furthermore, as a unique occasion we could measure octave spanning Brewster angle chirped mirrors. In the following subsections we present our results which have helped and improved already several other pulse compression experiments.

3.6.1 Double angle chirped mirrors

For the chirped pulse compression and GDD transfer experiments we used so called double angle chirped mirrors (DACM) [52]. DACM are based on the concept of canceling dispersion ripples but not having two mirror designs which cancel each other but only one design applied under two different angles which leads to a shift of the dispersion ripple and therefore cancels each others. The bandwidth of our DACMs were designed from 680nm to 890nm, supporting nearly 10fs pulses with p polarization. Per reflection, a GDD of -100fs^2 is compensated but third order dispersion was not included in the design. A general reflectivity of 99.97% was measured. The angle of incidence is 5° respectively 20°. Fig.3.16 (a) shows the mirror designs and its net GDD and (b)compares the calculated net GDD with the measured one. As
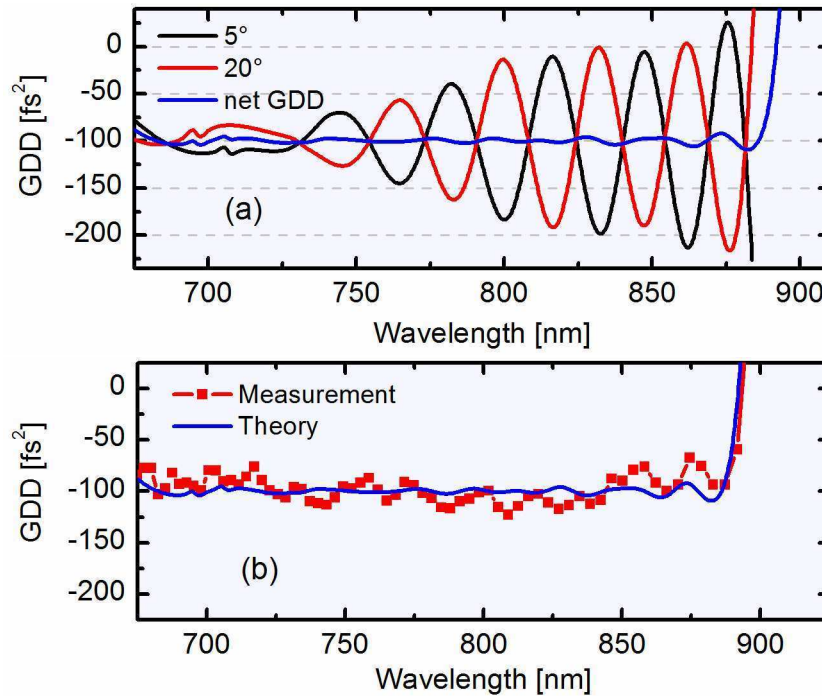

Figure 3.16: Net GDD of double angle chirped mirrors.

obviously, the canceling is very good for such a large bandwidth and provides small dispersion ripples with an amplitude of only 10fs^2. Such mirrors allow more than 100 reflections before

significant pulse distortion appears. The angle of incidence accuracy is shown in Fig.3.17 concerning the angle of incidence of 20°. A clear spectral shift of the GDD curve is observed,
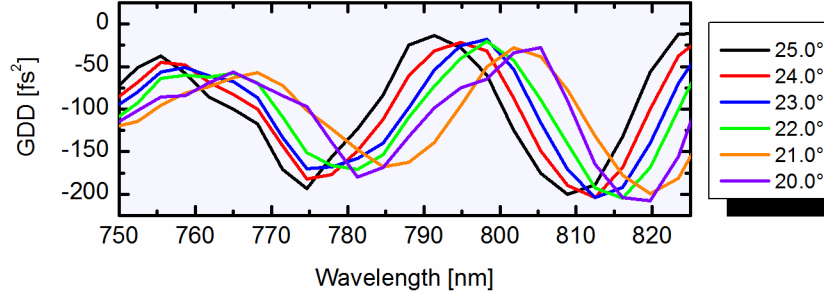

Figure 3.17: GDD angle dependence

depending on the angle of incidence. For a correct setting we found a necessary angle accuracy of ±0.3°. This can be still achieved only by hand if there are enough reflections on one mirror piece, in minimum two reflections. Concerning an angle of incidence of 5°, no significant spectral shift of the GDD curve has been observed for ±2°. The large freedom has been already noted in earlier experiments. For the input polarization accuracy we found that ±3° shows no difference. If s polarization instead of p polarization is used, the GDD curve shifts for a half period of the GDD ripples.

3.6.2   5fs complementary double chirped mirrors

Complementary double chirped mirrors have been designed for 5fs, p-polarized pulse compression, designed for a bandwidth from 550nm to 1200nm with an angle of incidence of 7°. Due to the large bandwidth only a small amount of GDD correction is possible. Therefore it is necessary to make several reflections on the mirrors which require that the dispersion ripples should be kept small to avoid pulse distortion. Complementary DCM will fulfill this requirement. The net compensated GDD is around -30fs^2 with dispersion ripple amplitude of 50fs^2. Third-order dispersion compensation is already included. For the used fiber length of 1.95cm (resulting in much more GDD as compared with hollow core fibers) we have estimated the need of around 30 reflections. Fig.3.18 (a) shows the complementary DCM design and (b) the measured net GDD compared with the design one. Between 680nm to 1000nm the complementary curves cancel each other resulting in a net GDD curve close to the theory one. Below 680nm the curves overlaps each other giving rise to huge dispersion ripples. The reason is not fully clear but probably due a production error. Measuring several DCMs we made an essential observation. Fig.3.19 (a) shows the measured GDD curves of two different DCM which have the same GDD design. Therefore we expected to measure the same GDD curve but as highly visible they are spectrally shifted to each other. A spectral shift in the reflectivity should been observed too, as the reflectivity is given as well through the dielectric multilayer structure. In Fig.3.19 (b) we measured the reflectivity and immediately we note that the reflectivity curves are spectrally shifted. Measuring all mirrors we have observed for every mirror a different strong spectral shift in the reflectivity, although they have been manufactured in the same production run. Consequently, the manufactured GDD curves are all shifted differently to each other. Therefore, no sufficient canceling of the dispersion ripples is possible when the GDD curves are unknown of each chirped mirrors, leading to huge dis-
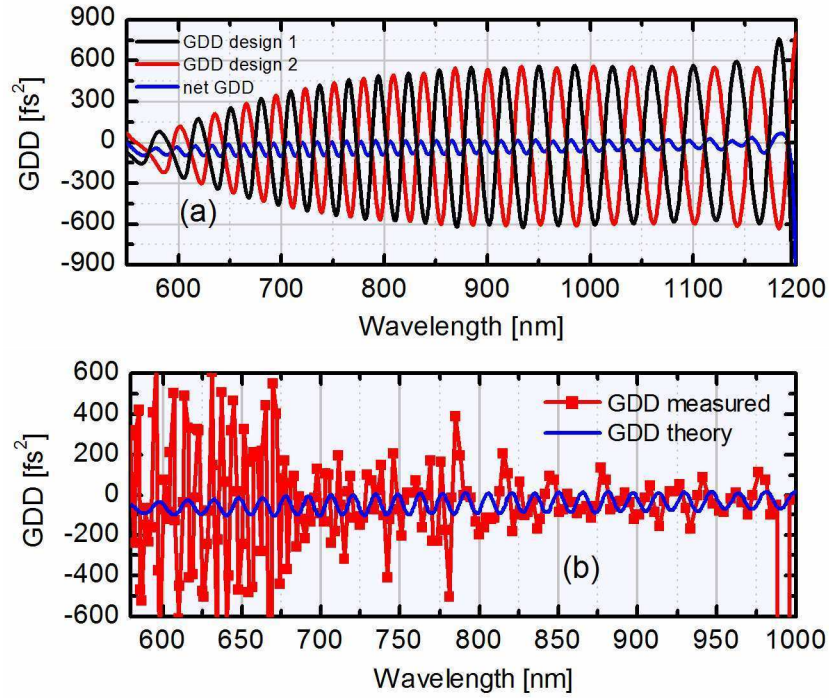
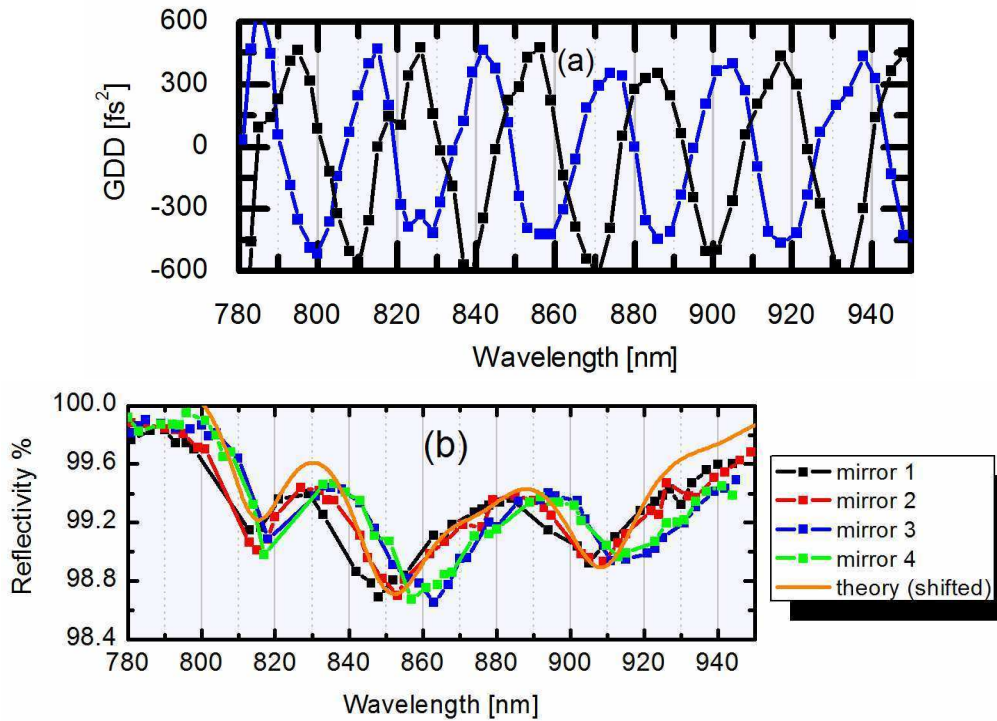Figure 3.18: Net GDD of 5fs complementary double chirped mirrors.

Figure 3.19: Spectral displacement of the GDD (a) and reflectivity (b) curve.

person ripples and strong pulse distortion. For successful pulse compression it is unavoidable to measure the GDD curve so that one can select the DCMs which will lead to a canceling of their dispersion ripples. For our 6fs pulse compression experiment we used only measured and selected chirped mirrors which guarantee proper canceling of the dispersion ripples. The spectral shift comes probably from the coating process which produces slightly different layer thicknesses on each mirror.

3.6.3   Brewster angle chirped mirrors (BACM)

Octave spanning antireflection (AR) coatings are challenging to produce. To avoid AR coatings one can design the DCM for an angle of incidence at Brewster's angle [65]. The Fresnel reflectivity vanishes for p-polarization which should avoid dispersion ripples. BACMs support a bandwidth over one optical octave as the variation of the Brewster angle in the visible is very small over one octave. Using BACM routinely sub 9fs pulses in the visible are achieved. Coincidentally we had the occasion to measure the BACM used for the sub-6fs pulse compression experiment [67]. The recorded GDD curve under Brewster angle is shown in Fig.3.20. The
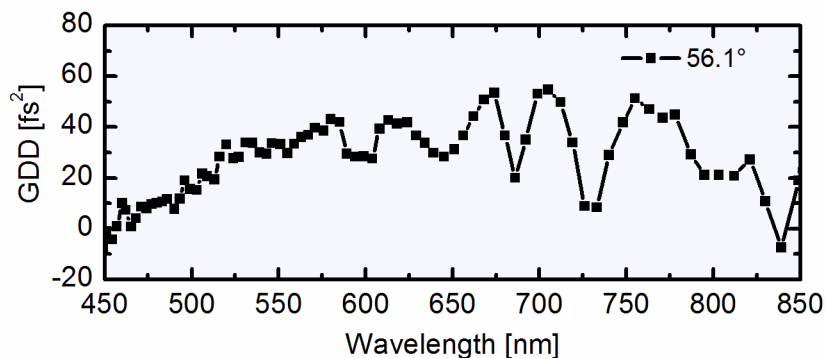
Figure 3.20: Measured GDD curve of a sub-6fs Brewster angle chirped mirror.

dispersion ripples with amplitude of 10fs^2 are very small and provide an proper pulse compression. However, they do not vanish totally probably due impedance matching inside the layers. The accuracy of setting the Brewster angle we found as $\pm 0.5°$ which can be achieved by hand. Changing the input polarization for more than 10° we have not observed a significant difference compared to the p-polarized case. In Fig.3.21 we measured another BACM made for the same specification as the above mentioned one. As clearly seen the dispersion ripples towards the near-infrared are much stronger. We believe that the reason lies in the manufacturing process but we cannot specify it in detail. Therefore one should characterize the BACM as well before applying; even one does not have to care about selecting the correct one as with complementary DCMs. Our results support the experimental observation that not all BACM have resulted in the same good pulse compression.[4] The measured BACM belong to the group of Prof. Dr. Riedle at the Ludwig-Maximilians-Universität, and have been designed by Dr. Steinmeyer. The GDD measurements and analysis have been done together with Nils Krebs of the group of Prof. Dr. Riedle.

---

[4]private communication, Nils Krebs, Riedle's group
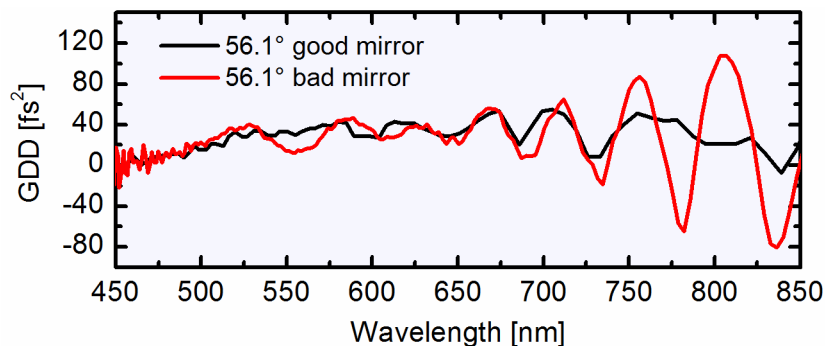
Figure 3.21: Different GDD curves of Brewster angle chirped mirrors.

3.6.4   Conclusions

Chirped mirrors are a very essential and powerful tool for dispersion management, demonstrated in numerous experiments including our ones. But the very high demands on the layer thickness accuracy for each mirror can be achieved only approximately. This leads to slightly different layer thicknesses on every mirror, resulting in a spectral shift of the GDD curve. Consequently, chirped mirrors designed for a configuration of canceling dispersion ripples will not cancel its dispersion ripples which leads to a strong pulse distortion.We strongly encourage to measure the GDD curve of each chirped mirror so that corresponding complementary pairs can be found and selected for successful pulse compression.

3.7   Summary and conclusions

With a proof-of-principle experiment we demonstrated the generation of 6fs with 15nJ at 5MHz, using only one fiber stage with an LMA-5 and 55fs long input pulses directly from the oscillator. If the input energy is increased we achieved a spectral broadening corresponding to a Fourier-limit of 5.3fs with 40nJ of output energy. The transmission has been only around 60% but can be probably increased by a suitable beam matching onto the mode field diameter. Scaling up the energy should be feasible using the concept of chirped pulse compression, or the optimization of different core diameter respectively numerical aperture.

Excellent long term and pulse-to-pulse stability (RMS ~1.3%) has been measured for the concept of chirped pulse compression in combination with our chirped oscillator. The fiber was not protected nor fixed on the holder. We believe that protections like a fiber case, fiber fixing or a fiber alignment system will further improve the stability. However, even without protections it is more than sufficient for further experiments.

Unproblematic operation has been found if the input power is set 10% under the self-focusing threshold of around 2.6MW. In none of our experiments, ablation or other type of direct damage to the input surface was observed. Neither dust has been a problem. Removing the jacket of the fiber should be done mechanically and not by aceton as this will cover the fiber surfaces and decreasing the damage threshold.

The polarization ratio after spectral broadening was found to be stable with >1/100 for linear polarization. Respectively ~1/60 if circular input polarization and transforming back to linear one after spectral broadening is used. For circular input polarization we have coupled ~31% more energy into the fiber compared to linear polarization, which is close to

the theoretical limit of 33%. The azimuthal orientation of the fiber's photonic structure was investigated and found to be insignificant for the output values.

With white-light interferometry we recorded the GDD curve of different chirped mirror concepts. Thereby, we noted that the GDD curve for each chirped mirror shifts spectrally to the others which is very inconvenient for complementary designs where the GDD curve should cancel each other. Reaching short pulses, the GDD curve of the chirped mirrors have to be measured so that one can select the correct cancelling chirped mirror pair.

In conclusion, thanks to a good long term, pulse-to pulse stability and polarization ratio, the simple and compact concept of chirped pulse compression together with a chirped pulse oscillator presents a valuable alternative for the generation of short pulses at MHz repetition rate. Direct applications can be high harmonic generation [40], resonant plasmonic field enhancement [41], material processing [56] or ultrafast spectroscopy [54, 55]. In this chapter we have demonstrated that the concept of chirped pulse compression in combination with a chirped pulse Ti:sapphire oscillator is ready for applications.

Chapter 4

High average power and μJ pulse compression at MHz repetition rate

During the last years, the optics community has attentively pursuit the development of Yb doped femtosecond laser and amplifier concepts at MHz repetition rate which resulted in several μJs laser-system at MHz [35, 36, 49]. Although attractive for many applications like coherent XUV generation [40, 68], material processing respectively micromachining [69], optical parametric amplification [70] and others [49, 71], due the material bandwidth the pulse duration stayed between 300fs and 1ps which represents a clear drawback for a variety of experiments which desire sub-30fs or 5fs [40]. Combining pulse compression with the current Yb MHz laser systems would present a powerful tool for ultrafast optic research.

In 2003, a 800fs Yb:YAG thin disk laser has been compressed using a large mode area fiber to 33fs with an output energy of 0.5μJ at 34 MHz [29]. Though this was a promising beginning no further development has been done to combine pulse compression with Yb laser systems for daily applications. Only two more experiments at MHz have been published [31, 32] with comparable output energies [32]. Pulse compression with an input energy respectively output energy clearly above 1μJ at MHz has not been shown yet. It is unclear how self-phase modulation in fibers at such energies respectively average power will behave. Questions like the influence and consequences of thermal properties and, or the appearance of other nonlinear effects aren't yet answered. Yb baser laser systems have made great progress since 2003 and it is essential to clarify if pulse compression still can handle the achieved output parameters of these laser systems.

In this chapter we go a step further compared to 2003 and present spectral broadening and compression with input energies higher than 1μJ and with average powers over 100Ws. Thereby we gained essential knowledge on which other current pulse compression experiments are based.[1] However, a detailed measurement series was not yet possible therefore we restrain us in this chapter on presenting the fundamental observations we have found.

In section 4.1 we present the spectral broadening and compression results using our home-made Yb:YAG thin disk lasers and in section 4.2 we show our measurements of >100W pulse compression with the Innoslab amplifier. Different issues like polarization ratio, transmission or thermal behavior are discussed in section 4.3. A summary and conclusions are presented in section 4.4. With our experiments we have demonstrated the practicability of pulse compression with energies over 1μJ and average power over 100W.

---

[1]Experiments of Lauryna Lötscher (MPQ) and Peter Russbüldt (ILT)

4.1   Pulse compression using a 1ps Yb:YAG thin disk laser

Pulse compression of a Yb:YAG thin disk laser at MHz repetition rate has been demonstrated in 2003 through the group of Prof. Dr. Keller at ETHZ [29]. Using a large mode are fiber (LMA) for spectral broadening, a Yb:YAG thin disk laser has been compressed from 800fs down to 33fs with an output energy of 0.5μJ at 34 MHz. Although the results attracted the community, only a few experiments have followed [30–33]. In 2007 the group of Prof. Tünnermann presented a pulse compression experiment using a Yb:KGW amplifier [32]. However, the input energy stayed under 1μJ. First in 2009 a publication with an input energy of 4μJ appeared, using an 80μm core diameter LMA but at 200 kHz repetition rate [33] and thereby neglecting possible thermal influence or other effects which can occur at MHz. In this section we focus on spectral broadening with input energies above 1μJ and how large one can achieve spectral broadening using a 1ps Yb:YAG thin disk laser at MHz repetition rate. As stated in the introduction we didn't performed a detailed measurement series but nevertheless we gained first essential insights for pulse compression experiments with high input energies and average power.

We used a homemade Yb:YAG thin disk laser at 1030nm, 11MHz, 1ps and 5.5μJ (60W) output energy. After the oscillator, a tunable attenuation (half-wave plate and a thin film polarizer) and an isolator for 50W (Electro-Optics Technology, Inc.) has been placed before we coupled into a large mode area photonic crystal fibers using a plano-convex, antireflection coated lens. A lever-arm is placed before the focusing lens. The final available energy for experiments was around 4.5μJ. The fiber holder is made out of aluminium, is nearly as long as the fiber respectively 10cm or 15cm, and contains a V-groove for the fiber. It is placed onto a 3-axis positioner (Thorlabs, MBT616). Note, the fiber is not cooled. The spectrum is recorded with a high resolution spectrometer from Oceanoptics (HR400) having a resolution of 0.01nm. We collected the light scattered by a white paper because regularly used black beam blockers absorb the spectral parts of the broaden spectrum differently strong. Pulse compression is done using double chirped mirrors ranging from 980nm to 1100nm for p polarization with -500fs^2 per reflection, see Fig.4.1, with an angle of incidence of 5°. No

Figure 4.1: GDD and Reflectivity design curve
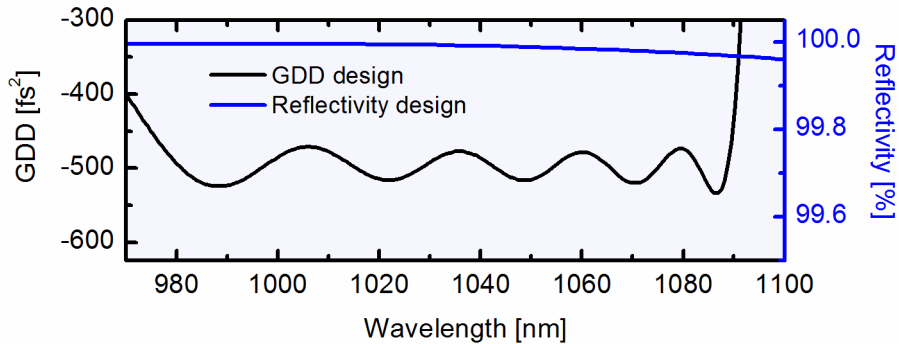
complementary design is used and third-order dispersion compensation is not included. Note, the chirped mirrors were not yet available during the measurement series concerning $>\mu$J spectral broadening. We used different LMAs ranging from core diameters of 12.5, 15, 20, 25 and 35μm, all available from Thorlabs. For $>1\mu$J spectral broadening we applied only 25 and 35μm.

Before we discuss the $>\mu$Js experiments we briefly demonstrate pulse compression with sub-μJ input energies. Fig.4.2 show the spectral broadening in a 65mm long piece of LMA-15 (15μm core diameter) with an input energy of 545nJ (6W), a transmission of 75% (410nJ output) and a spectral broadening corresponding to $\sim$75fs. For compression we used 12 re-

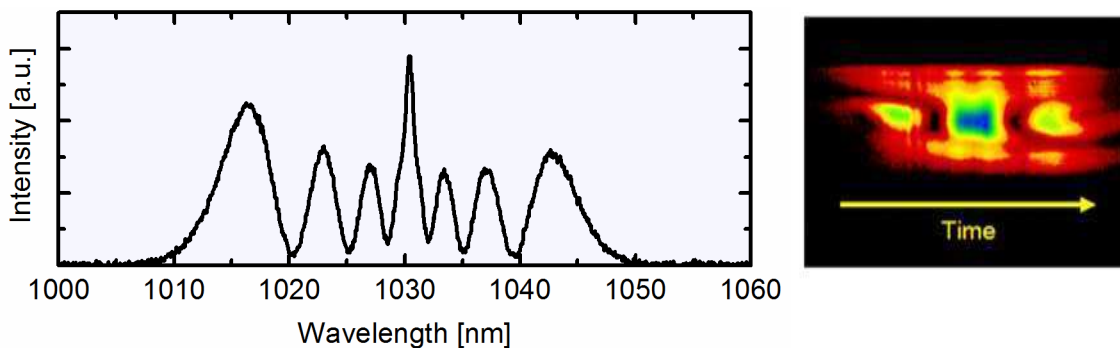Figure 4.2: Proof-of-principle pulse compression of 0.5μJ to $\sim$100fs

flections on the chirped mirrors. With a GRENOUILLE (Swampoptics, Model 8-9-USB) we recorded the trace (right picture of Fig.4.2). The raw data trace is shown. The main part in the middle is compressed to around 100fs (no scale in the picture). The achieved spectral broadening and compression is not as large as in the paper of 2003 due a three times shorter fiber length. A certain amount of energy is left too in a pre or after-pulse, probably coming from the uncompensated third-order dispersion. The trace is not yet optimized but as proof-of principle experiment it is obviously that the pulse can be compressed. In section 4.2 further autocorrelation traces using the Innoslab amplifier are shown. We should note here that GRENOUILLE traces (or better generally FROG and SPIDER traces) of such high power pulse compression in solid core fiber has not yet been published. Calculating the optimal fiber length [8] for the parameters above we found a length of 114cm which is much longer as our used 6.5cm. Therefore, following section 1.2.2 respectively [6] the linear chirp for compression does not cover the full pulse width, probably only to around 60%. The other part leads to a background and, or enhanced pre and after pulses as shown in [6]. It would be interesting and important to know how much energy is now really compressed in the pulse. A simulation is therefore necessary as well. Using a 114cm long fiber is not suitable as on the one hand the compression of the huge amount of GDD and third order dispersion is difficult (not suitable with chirped mirrors) and on the other hand other unwanted nonlinear effects can appear due the long fiber length. The optimal fiber length should be considered more as a hint than as a fixed number, as it is based on assumptions whose validity is not always fully given for our input values.

Increasing the energy, we coupled 2.2μJ (24W) into a 15.8cm long LMA-35 with a transmission of 68% (1.5μJ), see Fig.4.3 (a). The spectrum still shows clear the self-phase modulation pattern and corresponds to a Fourier limit of 30fs. Looking at a larger spectral range (Fig.4.3 (b)) we detect new generated spectral parts between 825 and 870nm. Increasing the energy further one increases mainly these new spectral parts. This could be a first limitation of the pulse compression scheme in combination with Yb based laser systems at MHz. In section 4.3 we discuss in detail this new frequency generation. With our tunable attenuation we could increase the input energy up to slightly over 4μJ ($>$40W) using a LMA-35 fiber.
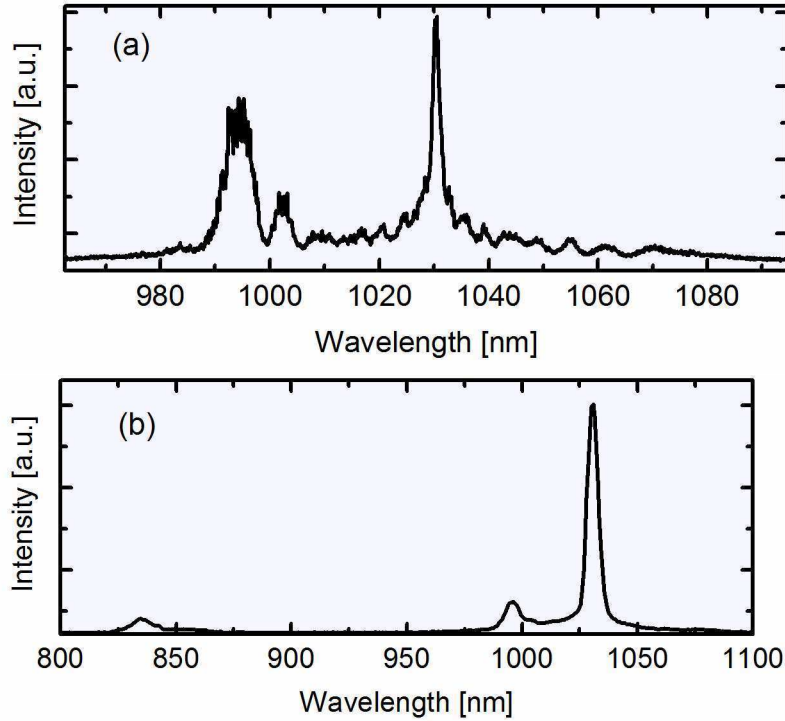
Figure 4.3: Spectral broadening for 2.2μJ of input energy (a) and generation of new frequencies (b)

Unfortunately, later it has been observed that the used isolator starts generating a thermal lens after 25W, even specified for 50W. As the thermal lens distorts the coupling into the fiber, more energy can escape into the cladding leading to unwanted effects like the cladding modes, see 4.3.2. Therefore, we had to pay attention with the interpretation of the obtained spectra with an input energy larger as 2.5μJ. We decided to leave these spectra away. Coupling 4μJs (40W) into the fiber [2] was possible only with a LMA-35. Increasing the energy resulted in a damage of the input piece of the fiber, probably by self-focusing. Thereby, parts of the first few millimeters of the fiber were blow up. From our measurement with the >100W average power Innoslab amplifier (next section) we know that the blow up is not caused by the average power, respectively intensity.

Starting with a 1ps long input pulse the maximally achieved spectral broadening always had corresponded to a Fourier-limit between 25 - 30fs [29, 32]. But it would be interesting to know if longer fibers as the normally used 15cm ones will increase the spectral bandwidth significantly. In Fig.4.4 we have increased the fiber length of a LMA-25 dramatically to 43cm. Using an input energy of 0.96μJ (10.8W) we achieved a spectral broadening corresponding to a Fourier-limit of 19.0fs with an output energy of 0.43μJ. For comparison the spectrum of Fig.4.3 is added. Note, due the larger bandwidth the spectrum is taken with a HR2000 Oceanoptics Spectrometer which is not able to resolve the modulation structure. Looking at the beamprofil we see that it is not the fundamental mode however, this is an alignment issue as we were able to achieve proper fundamental mode too, but with a slightly smaller

---

[2]respectively focusing onto the mode field diameter on the fiber surface

spectrum.[3] The transmission was measured to be only 44%. The spectral attenuation of the
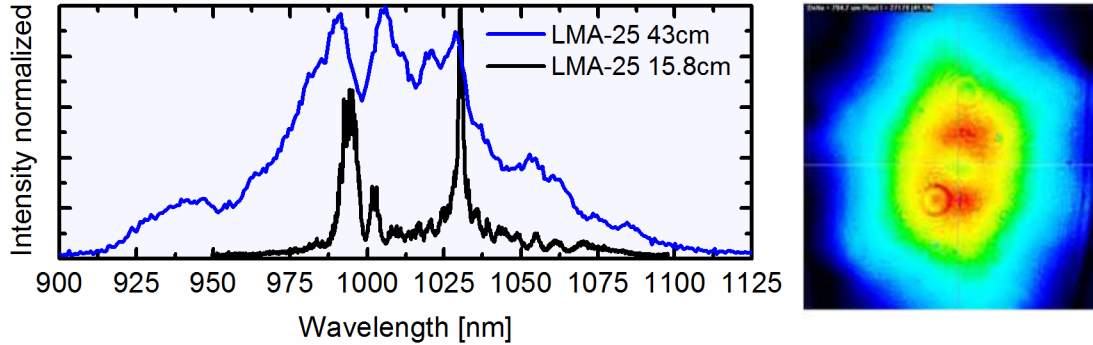
Figure 4.4: Spectral broadening and beamprofil after a 43cm long LMA-25 fiber

LMA-25 is only ~5dBm per km in this spectral range and therefore not strong enough to explain the low transmission. The measurements so far have shown that reaching sub-30fs is not that trivial starting with a 1ps Yb:YAG thin disk laser. But if shorter input pulses would be available, the sub-20fs region could be accessed. Fig.4.5 shows spectral broadening using a commercial YB:KGW lasersystem (Jenlas D2.fs of Jenoptik) at 1025nm with 350fs input pulses, 1μJ (100mW) at 10kHz and a 10cm long LMA-25 fiber. The measurements have been done in the Group of Prof. Dr. Riedle at Ludwig-Maximilians-Universität München. The spectrum supports sub-20fs pulses. But the generation of new frequency components
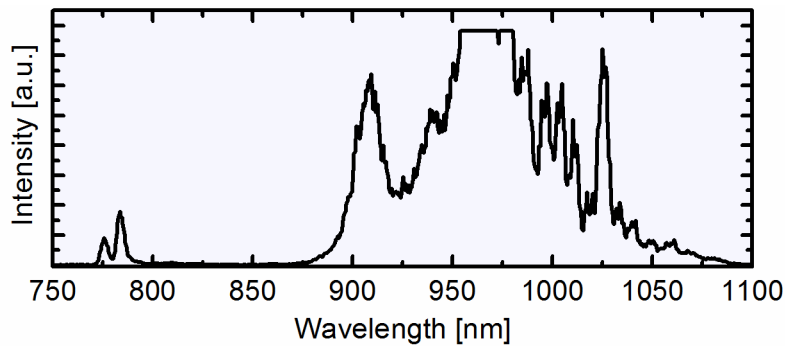
Figure 4.5: Sub-20fs with input pulse duration of 350fs

not due SPM is observed again. If a Yb:YAG thin disk laser could be compressed first to 300-500fs one probably could reach with a second pulse compression the sub-15fs area with nearly the full energy. The first spectral broadening could be done in a crystal or glass, and after compression with chirped mirrors. This setup wouldn't require any alignment and could be very compact. However, we have found that our Yb:YAG thin disk laser has slightly to less energy for testing this approach. The new generation of high energy lasers and amplifiers at MHz repetition rate will overcome this point.

The presented results do not claim to cover the full topic in detail as no systematical study has been done. In summary we have seen that 1ps pulses can be compressed but input

---

[3]We observed the tendency that a 01 mode at 1030nm will lead to a slightly larger spectral broadening as through the fundamental one

energies above 1μJ can lead to new frequencies not generated by self-phase modulation. This could be a limitation for larger spectral broadening and the available energy compressed in the pulse. Furthermore we noticed a lower transmission compared using Ti:sapphire laser systems at 800nm. From our and other experiments we know that it is hard to reach sub-25fs pulses starting with 1ps. Using very long fibers and optimizing the core diameter one should be able to reach sub-20fs. However, using 300fs pulses which are available from YB:KGW lasers, sub-20fs should be reached much easier. Therefore, an interesting approach would be to make a first pulse compression of the 1ps pulses through bulk or gases to 300fs and then with fibers a second pulse compression down to sub-20fs. As the bulk or gas approach does not require any alignment or complex optics, this could be as well an interesting opportunity for high energy lasers [72].

4.2 100W pulse compression experiments with an Innoslab amplifier

The femtosecond Innoslab amplifier concept is a very powerful one and has generated up to 400W at 1030nm with 650fs at 76MHz repetition rate [36]. In the meantime it is commercial available (www.amphos.de) too. Combining two such amplifiers have demonstrated >800W output average power [36]. But for a variety of applications shorter pulses would be more suitable, like high harmonic generation [40] or material processing[4]. A pulse compression setup using solid core fibers is unavoidable for generating shorter pulses. But the high average power will rise the question how the thermal influence will act onto the fiber and self-phase modulation process, respectively compression. No experience with over 100W laser systems exists and only rarely with 50W Yb:YAG [29] thin disk lasers and fiber amplifiers [32]. In this section we present first spectral broadening and compression experiments beyond the 100W scale.

For the experiments we used an Innoslab amplifier with 650fs long output pulses and maximally 400W of average power at 76MHz repetition rate, provided by the Fraunhofer-Institute of Lasertechnique ILT in Aachen, Germany. The Innoslab amplifier was seeded by a Yb:KGW oscillator at 1029.5nm with 1.5W, 300fs at 76MHz from "High Q Laser Innovation GmbH". Because of the fiber's input surface back reflection we have to place an optical isolator (Jenoptik, I-FS-1-P100-1030) after the Innoslab amplifier. Current best free space optical isolators are only working up to 200W without generating a thermal lens. Note that the Innoslab amplifier is working in both beam directions. Therefore it is very important to suppress the back reflection of the fiber. A 10.7cm long LMA-35 piece was placed unfixed in the not cooled fiber holder without any protection against dirt particles. For compression we used the same chirped mirrors presented in the last section with -500fs^2 per reflection from 980nm to 1100nm, and quartz plates for fine tuning. Fig.4.6 shows spectral broadening of 128W input power (1.68μJ) with a Fourier limit of 33fs and an output power of 82W (1.08μJ) corresponding to transmission of 64%. The spectral broadening evolves as the spectrum generated with a Yb:YAG thin disk laser and shows the same characteristic of a high peak at the fundamental wavelength (see section 4.3) and the typical self-phase modulation pattern. The interferometric autocorrelation (Femtochrome Research Inc., Model FR-103PD) indicates a pulse duration of $\sim$35fs (FWHM) and demonstrated the successful pulse compression of these high average power pulses. However, in the autocorrelation the first strong wiggles

---

[4]sub-100fs is desired, private communication with the Fraunhofer-Institute of Lasertechniques ILT
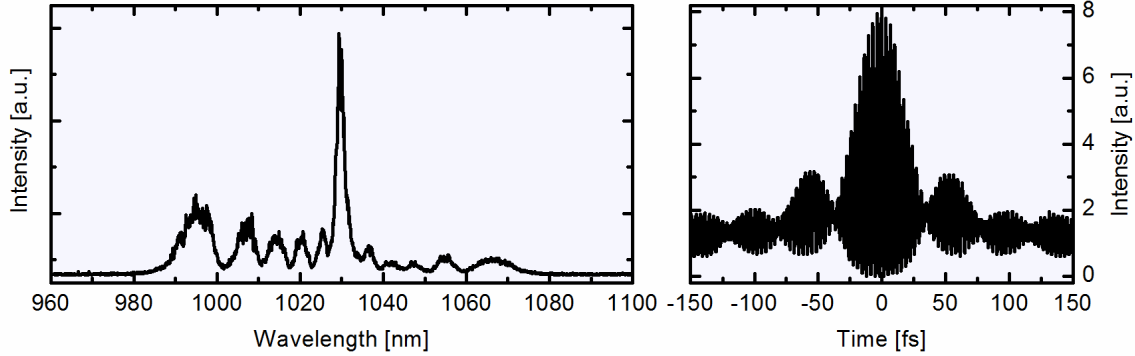
Figure 4.6: Spectral broadening and pulse compression of >100W input average power

appears from a not yet optimal compression. Therefore the pulse is still chirped and will be slightly longer as the measured 35fs. The other wiggles shown in the autocorrelation are coming from the spectral shape and are inevitable.

Increasing the input power we observed a decrease of the spectral bandwidth and in parallel an increase of the power around the fundamental wavelength, see Fig.4.7. We think
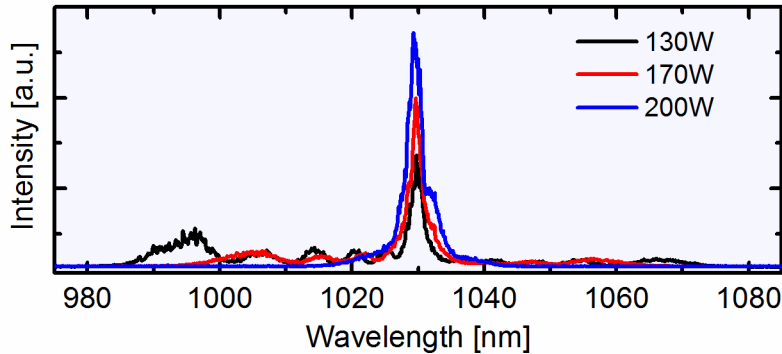
Figure 4.7: Spectral narrowing due thermal influences, no cooling.

that this decrease is a consequence of the thermal influence onto the fiber. Because all lenses are made of quartz, showing no thermal lens and the isolator first starts lensing after 200W. Cooling the input part of the fiber as done at ILT restores the spectral bandwidth again. It is not yet clear how the thermal influence acts on the fiber but probably it disturbs the coupling and therefore the wave guiding in the fiber leading too an increased scattering into the cladding part which heats in addition the fiber, changing again the material properties and leading to a different wave-guiding. Thermal influence in our experiments occurred at around 100W but had first a significant influence after 150W. Probably a better coupling will increase thermal threshold as less light gets scattered into the cladding. However, cooling the fiber allows stable operation with around 150W, even 200W, of input power and over 100W of output power.[5] Finally we point out one more thing, namely mode filtering. The amplified beam after the Innoslab has a measured M^2 of around 1.5. It is well-known that a single mode fiber acts as a mode filter too. We have measured the M^2 after the spectral broadening and

---

[5]according to the group at ILT

have found an improved M_x^2 of 1.23 and M_y^2 1.18 for the beam. Later experiments showed even a M_y^2 of 1.05. This is a welcome effect improving the whole laser setup. Note, an input beam $M^2<1.8$ is necessary to couple into the fiber. The current limitation for high average power is the thermal lens of the isolator which disable efficient coupling into the fiber as the M^2 of the beam increases. The constructing of even more powerful isolators is on the way but challenging.   In conclusion we have demonstrated that pulse compression down to 35fs with >100W input average power can be done and is stable enough for further applications as shown by the experiments at the Fraunhofer-Institute of Lasertechniques ILT. Problems through a thermal influence arise but can be handled by cooling the fiber. The limiting factor for increasing the input power is currently the thermal lens generated by the isolator which disable efficient coupling into the fiber.

4.3   Characteristics

During the fist section we presented successful high average power and μJ pulse compression down to 35fs. But contrary to the pulse compression at 800nm with the Ti:Sapphire laser, we noted a couple of differences at 1030nm which we have not yet emphasized in detail. In this section we discuss the most important differences which are the fiber's transmission, so called cladding modes, polarization ratio decay and the thermal influence.

4.3.1   Transmission

In the Ti:Sapphire pulse compression experiments at 800nm we observed an average transmission of around 88% at any input energies, thereby we used a maximally 5cm long LMA-25 fiber. Using a 1030nm laser-system, transmissions of only around 60% have been published [29]. In our own experiments we achieved a transmission between 70% and 80% at the beginning, using a 15cm long LMA-25 and LMA-35. The transmission decreased at higher energy to around 70% - 60%. Surprisingly, there is one publication which has reported a high transmission of 90% [32]. Contrary to all the other experiments they used only a 6cm long LMA fiber with a mode field diameter of 30μm. In our experiment with a 6cm long LMA-25 we achieved a transmission of 78% at an input energy of 1.8μJ. This value can be probably increased if a telescope for optimal mode-matching onto the fiber is used, as well as if no aceton for removing of the jacket will be taken. We noted the tendency that the transmission decreases using longer fibers as well as from an increased input energy. Note that we can exclude the average power as main reason due the different repetition rates of our used laser systems. A detailed measurement series should be done to confirm these tendencies. The reason of the lower transmission is not yet fully understand. One suggestion is that the fundamental fiber mode of the LMAs is not so strong bound anymore at 1030nm as at 800nm and therefore leaks stronger into the cladding, triggering other processes as well as cladding modes [13]. This would explain the fiber length and the input energy dependence. Using smaller core diameter LMAs which should exhibit a stronger bounding of the fundamental mode, an identification of the underlying process should be possible. Scattering losses in the fiber, as a possible reason, can be excluded. Because the LMA-25 and LMA-35 show the same transmission but the LMA-35 has already an attenuation of >100dB/km but the LMA-25 has only 5dB/km (www.nktphotonics.com). The transmission optimization of pulses at 1030nm in LMAs is an important aspect for further applications. For increasing on the one hand the final compressed

energy in the pulse but also to avoid and to delay nonlinear effects caused by the leaked light into the cladding, which will limit spectral broadening.

4.3.2 Cladding modes

As cladding modes [13, 73] we term modes which are not guided in the core but by its cladding structure. Such modes have a larger divergence and are centered like a ring around the core beam. Furthermore they do not experience self-phase modulation. In Fig.4.8 we see two spectra with different input energies but as highly visible a peak has raised strongly around the fundamental wavelength. The measurements were done with the Innoslab amplifier setup and fiber properties. Same behavior has been observed with the Yb:YAG thin disk laser. Using
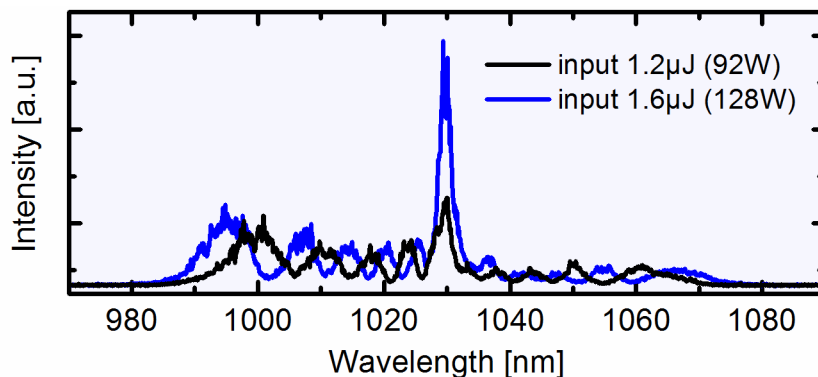
Figure 4.8: Cladding modes at higher input energies around the fundamental wavelength

an iris we could decrease the peak by maintaining the spectral bandwidth. We concluded that the peak originates from the cladding modes. A high coupling efficiency of the beam into the fiber delays the appearance of cladding modes. It is helpful to monitor the near-field profile of the fiber output for optimizing the coupling efficiency. However, cladding modes will be generated after a certain input energy. We found an input energy of $\sim 1\mu J$ for a 15cm long LMA-25 fiber with a transmission of $\sim 65\%$ as threshold for generating cladding modes in our setup. This explains why other pulse compression experiments [29, 30, 32] have not yet reported about cladding modes as they stayed beneath $1\mu J$. Using shorter fibers showed that this threshold is increased. Fig.4.9 shows the spectral broadening in a 6cm long LMA-25 fiber with an input energy of $1.8\mu J$ and a transmission of 78%. Note the small middle peak is an interference effect of the self-phase modulation [3]. We observed the tendency that as soon cladding modes appear, the additional energy if increased will mainly be transferred into the cladding modes. Consequently, the spectral bandwidth does not significantly increase anymore as well as the energy which experience self-phase modulation (see Fig.4.8). The contribution of the cladding modes concerning the thermal influence and to nonlinear effects is not yet investigated. Probably a short fiber piece is more suitable for spectral broadening with an input energy of several μJ.

4.3.3 Generation of new frequencies not due self-phase modulation

We observed the generation of new spectral components spectrally separated from the self-phase modulated spectrum. Fig.4.10 shows new spectral components, in dB scale, generated
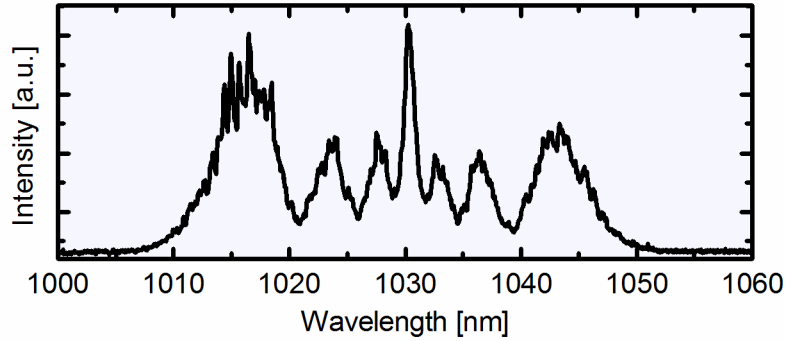
Figure 4.9: Less cladding modes appear in a shorter fiber piece (6cm LMA-25, 1.8μJ input energy, 78% transmission).

in a LMA-25. Following ref [74, 75] probably degenerate four-wave-mixing (DFWM) in the fiber is the reason. The experiments at ILT have shown similar spectral features, explaining it with DFWM.[6] More measurements and plotting a phase matching diagram would be necessary to confirm this assumption. However, this new spectral features slow down the original spectral broadening and the available compressed energy in the pulse. It is an interesting question if the SPM and the DFWM spectral parts can be compressed together without a too complex setup. Interestingly but expectable, the cladding modes are not present in the
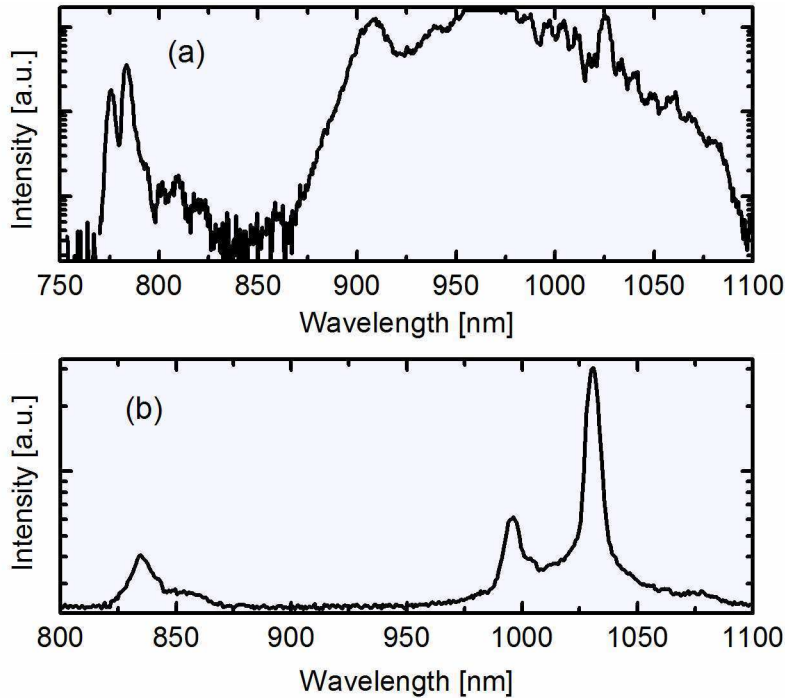
Figure 4.10: Possible degenerate four-wave-mixing in a LMA-25 with (a) 350fs and (b) 1ps input pulses.

---

[6]private communication with ILT

DFWM spectra as they are at least locally separated from the SPM spectrum. Furthermore, DFWM seems to "copy" the total broaden spectrum. Before we continue we should ask us why we do not observe DFWM in our spectra obtained in the Ti:Sapphire experiments. The answer is probably that due the much shorter input pulse duration the different spectral parts in the fiber are already temporally and locally separated when the bandwidth is large enough for DFWM for phase matching. With a 1 ps pulse duration this distance is much longer, ~15cm in our case.

The generation of new spectral parts in the fiber through another process, not SPM or DFWM, is shown in Fig. 4.11. In this figure the jacket of the LMA-25 was not removed but the same spectral components have been observed as when using LMAs with removed jackets, at very high input energies. Recording the beamprofil we observed that the new frequencies
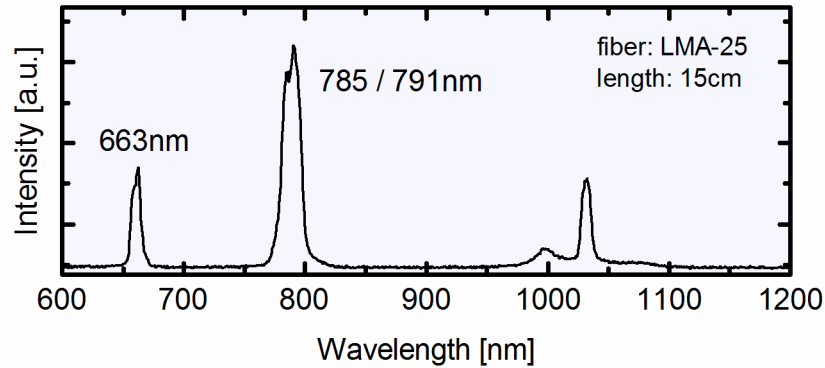
Figure 4.11: Possible Cherenkov radiation generated in the jacket?

are defined as a ring around the core, whereas different wavelengths had a different radius. As further in the visible spectrum as larger the radius was. We also think to have observed a tendency that the new generated frequency scales with the fiber length. A possible physical nonlinear process could be Cherenkov radiation, generated in the cladding or jacket [76]. Unfortunately, more data would be necessary to verify this assumption.

The unwanted generation of new spectral components not due self-phase modulation decreases the energy in the compressed pulse as well as slows down the generated spectral bandwidth through SPM.

4.3.4 Polarization ratio decay

With the Yb:YAG thin disk laser and a 15cm long LMA-25 fiber piece we observed a strong polarization ratio decay after the spectral broadening when the input energy is increased. This stands in a clear contrast to the Ti:Sapphire results where the polarization ratio stayed over 1:100. Note that in all our measurements, with the Yb:YAG and Ti:Sapphire laser we have used non polarization maintaining LMAs. Fig.4.12 summarizes the measured polarization ratios using the Yb:YAG thin disk laser. Due the limited spectral bandwidth of our polarizer we could measure only until 1μJ. At an input energy of 1μJ we measured a polarization ratio of only 1:5. The same measurement was repeated with a regenerative thin disk amplifier at 3kHz, 1030nm center wavelength and an input pulse duration of ~1.5ps. Fig.4.13 presents shows the polarization ratio obtained again after the spectral broadening in an undoped 100μm core diameter ROD-PCF (www.nktphotonics) of 10cm length. Obviously, the polarization
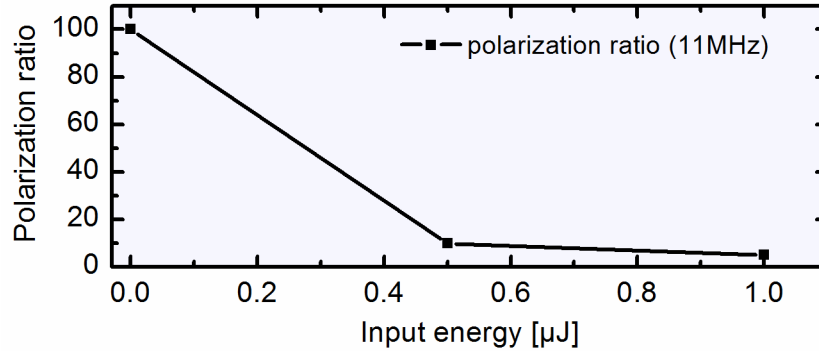
Figure 4.12: Polarization ratio using a thin disk Yb:YAG laser at 11MHz
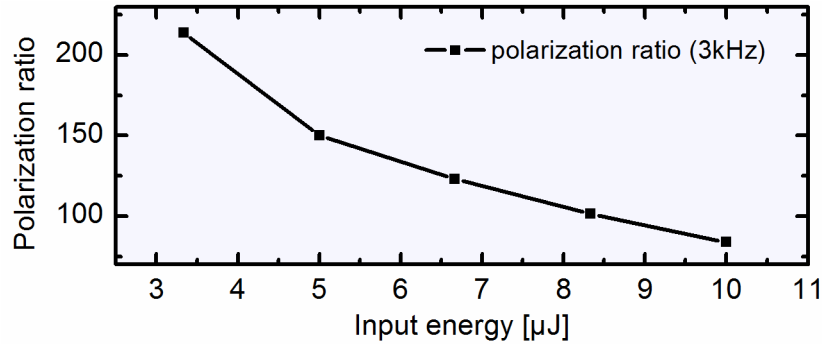
Figure 4.13: Polarization ratio using a regenerate thin disk amplifier (1030nm) at 3kHz.

ratio does not show the strong decay. These measurements were done together with Lauryna Lötscher and will be presented in detail in her thesis. Furthermore, the experiments performed at the ILT with the Innoslab ampflifier at 76MHz indicate that the polarization ratio is maintained as well. Without a comparison of these three laser systems it is difficult to see a tendency and the reason behind it. Currently it seems that the decay only appears when using the Yb:YAG thin disk laser. To improve the polarization ratio one could use polarization maintaining LMAs. Also a detailed measurement series should be done investigating if the ratio depends on the fiber length and, or the core diameter. Furthermore, one should clarify if this decay is a general problem of 1030nm laser systems or restricted to our Yb:YAG thin disk laser respectively the corresponding laser concept.

4.3.5   Thermal behavior

When working with a beam of several Watts of average power or more, one has to consider the thermal properties of the optical components in the beam path. Thermal lenses can be created through the material, increasing the M^2 of the beam which degrades the coupling into the fiber. Therefore one has to select lenses of a suitable material like quartz. Furthermore, a special optical isolator from Jenoptik has been bought, working until 200W without a significant thermal lens. Currently this is state of the art of free space optical isolators. Being sure that our spectrum is not influenced through thermal lens of an optical element, we observed three different regimes of thermal influence to the self-phase modulation process

in the fiber. Until 50W we do not see significant changes indicating that there is no thermal influence. From 50W until 150W we noticed that if the beam is blocked and unblocked again that it will take 1-3 seconds until the same spectral bandwidth is achieved as before. This is a strong indication for a thermal effect. Note that the same spectral bandwidth is reached quickly but the spectral form changes during 1-3 seconds. Over 150W we observe a decrease of the broaden spectrum and an increasing of the cladding modes (see Fig.4.14) as already reported in the last section. For the measurement, a 10.7cm long LMA-35 has been used with different input average power of 130W, 170W and 200W. Note, the fiber material is quartz as well. Cooling the fiber surfaces, performed at ILT, has prevented the decrease in the
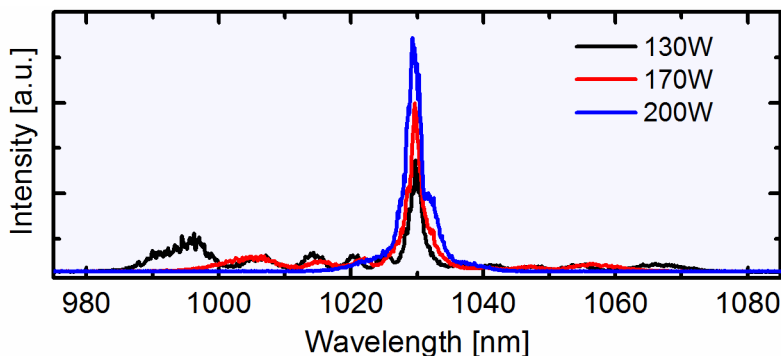
Figure 4.14: Spectral decrease of the broaden spectrum at different input powers.

broaden spectrum. Working with the Yb:YAG thin disk laser at 40W input average power we have noticed that the temperature of the fiber holder (made of aluminium) is only negligible increasing (can be touched by hand without any problem). This indicates in general a good wave-guiding in the core (and cladding of the cladding modes). However, a small misalignment of the input coupling increases the temperature of the fiber holder extremely. Touching by hand is not possible anymore.

The thermal influence to self-phase modulation is currently not the limiting factor of high average power pulse compression. Although we see their consequences, we can correct it by cooling the fiber. The power limitation is currently given by the thermal properties of the optical isolator which exhibits a to strong thermal lens above 200W of average power, disenabling the coupling into the fiber.

4.4 Summary and conclusions

We presented pulse compression experiments with a Yb:YAG thin disk laser at 11MHz and an Innoslab amplifier at 76MHz, both with a center wavelength of 1030nm. The Innoslab amplifier was compressed down from 650fs to 35fs with an output power of 82W ($1.08\mu J$). The transmission was always around 60-70% which is clearly lower compared to the experiments at 800nm. We performed first experiments with input energies above $1\mu J$ in LMA fibers as well as input average powers up to 200W. Thereby we observed the generation of so called cladding modes which slow down the spectral broadening as more energy is coupled into the fiber. The threshold for this cladding modes has been found slightly above $1\mu J$ for a 10 - 15cm long LMA-25 fiber. Using shorter fiber the threshold seems to be higher, as well as through a better mode-field matching onto the fiber. Cladding modes are limiting

the spectral bandwidth as well as the available energy in the compressed pulse. Another spectral bandwidth limitation is the generation of new frequencies probably by degenerated four wave mixing (DFWM). DFWM can be delayed to a certain extend by choosing suitable fiber parameters. It is an interesting question if the SPM and the DFWM spectral parts can be compressed together without a too complex setup.

Concerning the Yb:YAG thin disk laser we discovered a dramatic polarization ratio decay after spectral broadening to only $\sim$1:5 at 1μJ. This decay is in clear contrast to the Ti:Sapphire experiments. Polarization maintaining fibers will probably help to slow down this decay. However, it seems that this decay is restricted only to the Yb:YAG thin disk oscillator as such a strong decay has not been observed with the Innoslab amplifier or with a regenerative thin disk amplifier. For future applications it is important to clarify this point.

We have shown that high average power does not influence essentially the spectral broadening up to 100W and that with cooling the fiber one can operate pulse compression up to 200W of input power. Operating with even higher input average power is probably possible but the limiting factor is currently the thermal lens of the optical isolator, rising at 200W. To clearly distinguish average power (thermal) and energy effects one should perform an identical measurement series at kHz and MHz repetition rate.

Pushing our spectral broadening and compression experiments beyond the μJ and $>$100W regime we have gained first essential knowledge on the way toward μJ pulse compression at MHz repetition rate. We identified challenges and their possible solutions and have already built new setups, integrated in existing experiments.

Chapter 5

Nanoscale mid-infrared near-field spectroscopy

About the first half of my time was spent in the field of nano-optics. We combined Fourier-transform spectroscopy with a scattering scanning near-field optical microscope (s-SNOM) and demonstrated continuous near-field spectra simultaneously in amplitude and phase of gold and silicon carbide samples. True near-field character has been proven for the first time with near-field approach curves. The very weak mid-infrared broadband power has made it impossible to characterize the setup in detail or to record a full data set, as we were forced to work at the edge of the noise level. Currently, thanks to a new, more powerful infrared broadband laser system [77] and an improved detection setup, the microscope is successfully used to address physical questions. First results were published [78, 79], demonstrating the potential for the field of nanoscience.

Section 5.1 presents a brief overview and introduction about our work and research field. Section 5.2 describes the developed experimental setup and in section 5.3 we present and discuss first results. In section 5.4 an outlook is given and section 5.5 closes with a short summary and conclusions. Because of several reasons we omitted the results of the short work period performed in frequency-comb spectroscopy. We reference to the two published papers [80, 81] raising from this work, one of them [80] even awarded as "Best of 2008" publication in the optics and imaging section of "New Journal of Physics" (see appendix B).

5.1 Introduction

Nanoscience will pave the way to promising future developments and applications [82]. But handling nanoscale phenomena necessitates suitable microscopy tools to access critical dimensions for analysis and control. Well known techniques are transmission electron and scanning electron microscopy as well as the family based on the scanning probe microscopy which provide analysis for many research topics. Unfortunately, none of them can access directly the chemical recognition at the nanoscale <30nm, which is today highly desirable. Scattering scanning near-field optical microscopy [82], s-SNOM, has demonstrated to extend the range sufficiently down to 7nm, from the visible [83] to the terahertz range [84, 85]; routinely, 20nm resolution is achieved.

S-SNOM is based on an atomic force microscope (AFM) with conventional metal-coated probing tips (cantilevers) in tapping mode. A monochromatic laser beam is focused onto

the the cantilever tip apex, generating a nano-focus at the apex. This small and confined light source is used to locally probe the sample. Because of an optical near-field interaction between the tip-apex and the sample, the backscattered light contains also information about the local optical properties (e.g. refractive index) of the surface, see Fig.5.1. To distinguish
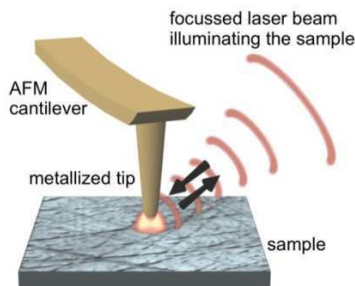

Figure 5.1: s-SNOM principle, picture from www2.neaspec.com

the relevant near-field information from the unwanted background scattering, different simple techniques exist [86, 87], like the higher-order demodulation of the near-field signal with respect to the cantilever frequency. The background signal is thereby not demodulated and therefore suppressed. The corresponding order is called n_1, n_2 and so on. In the mid-infrared region ($\lambda \sim 10\mu m$) one has to use at least n_2 for revealing near-field signals. The achieved optical resolution is only determined by the tip apex radius (in general 20nm), hence yielding the same optical resolution from the visible to the terahertz. Optical imaging is performed by detecting the backscattered light interferometrically (optical amplitude and phase images are acquired simultaneously) by the probing tip while scanning the sample surface topography. Note that s-SNOM is based on well-known and proven techniques and that no further special requirements are necessary, i.e. sample labeling. Several experiments in a variety of different fields from conductivity/ doping mapping in semiconductor nanostructures [83,88,89], i.e. transistors, single particle material recognition [90], plasmonics [91,92] and nanoantennas [93], to single virus analysis [94] and Mott transition in Vanadiumdioxid [95] have demonstrated the potential of s-SNOM for nanoscience. However, one drawback in all these experiments remained: the insufficient process of recording a spectrum. Due to the lack of suitable broadband laser sources in the visible and especially in the infrared region, only tunable monochromatic lasers have been applied, resulting in two main consequences for s-SNOM. The first is that recording the near-field spectra can be done only by comparing many recorded images with sequentially altered frequencies of the same probe position. This very time-consuming procedure supports unwanted artifacts like sample drifts, changing imaging conditions by cantilever tip erosion or contamination as well as small beam alignment changes. The second consequence is that only a narrow spectral ranges can be accessed by tunable monochromatic laser systems. Hence, many interesting samples can be explored only insufficiently, if at all, in the relevant spectral range with the near-field resonance. A first approach has been done in 2006 using multiheterodyne detection with frequency combs [96] but has suffered from a large complexity and could never identify true near-field signals. To sum up, s-SNOM lacks the essential feature of a true spectroscopic tool.[1]

Here we show that using a broadband mid-infrared laser source the combination of Fourier-

---

[1]Very recently, broadband near-field spectra using a thermal emitter have been published [97]. This experiment was based to a certain degree (technique) on the here presented results.

transform infrared spectroscopy (FTIR) with a scattering near-field optical microscope will overcome these limitations. Amplitude and phase spectra of gold (Au) and silicon carbide (SiC) in the mid-infrared are presented, as well as approach curves proving the near-field character. Adaption of our simple technique to visible and near-infrared can easily be done. In conclusion, our near-field microscope is able to record complete spectra in amplitude and phase at each scanning pixel thereby opening the route for true nanoscale spectroscopy.

5.2 Experimental setup

The experiment was based on a broadband mid-infrared laser-system, a commercial s-SNOM (NEAsnom, www2.neaspec.com) and a dispersive Michelson interferometer. Thereby, the s-SNOM is placed in the sample arm and the reference arm length is continuously varied for recording an interferogram and subsequent Fourier-transformation, see Fig.5.2 The broadband
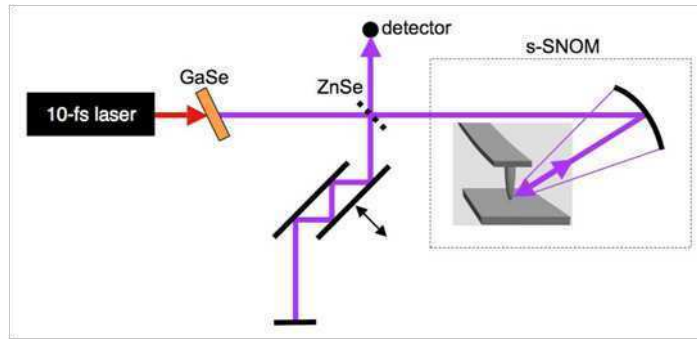
Figure 5.2: Schematic setup of the combined FTIR with s-SNOM, from [78]

mid-infrared is generated as described in [98], using a broadband Ti:Sapphire femtosecond laser and focusing the beam into a GaSe crystal so that the outer spectral parts fulfill the phase matching for degenerate difference frequency generation in the mid-infrared. Our commercial 12fs Ti:Sapphire oscillator (Femtolasers Produktions GmbH) is centered at 800nm with an average power of 440mW at 125MHz. With an aspheric 18mm lens we focus into a 200μm thick GaSe crystal. Depending on the phase matching we generate broadband mid-infrared with a FWHM of around 2μm, tunable from 7μm to 13μm (detector cut-off wavelength) with an average power of around 10μW, see Fig.5.3. A parabolic mirror behind the GaSe collects and collimates the mid-infrared beam, which is congruent to the residual input beam. Therefore, the residual input beam can be used to align the mid-infrared beam onto the tip-apex. But care should be taken not to damage the tip-apex through the high intensity of the residual beam. After the alignment, the residual input beam is blocked through a NaCl crystal, which also absorbs around 20% of our mid-infrared beam.

In the sample arm, the mid-infrared beam is focused by a silver parabolic off-axis mirror onto the tip apex of a commercial Si-coated cantilever (CSC37; MikroMasch), operating in the tapping mode with a frequency of ~30kHz. The backscattered light is collected by the same silver parabolic mirror and superimposed with the mid-infrared beam of the reference arm on the ZnSe beamsplitter. The signal was recorded by a mercury cadmium telluride (MCT) detector. A detailed description of s-SNOM is presented in ref [99]. A conventional FTIR achieves very high resolution by moving the end mirror of the reference arm over a long distance. In our case, due to the weak signal we have to average our spectra hence the
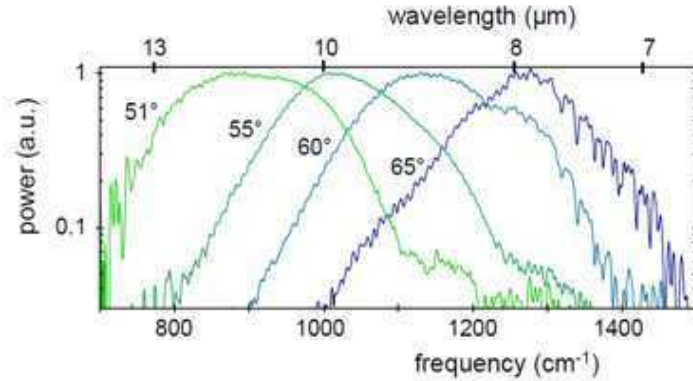
Figure 5.3: Tunable broadband mid-infrared spectrum, from [96]

spectrum should be recorded quickly. Therefore moving the end mirror over large distances, which takes several seconds or even minutes, is not a suitable solution as the imaging conditions may change. On the other hand, moving the mirror over a small distance will not give the required spectral resolution. The solution is a design shown in Fig.5.4. The beam is reflected several times between two mirrors in the reference arm, one of them is movable by a long range piezo. Due to several reflections on the movable mirror the optical path L
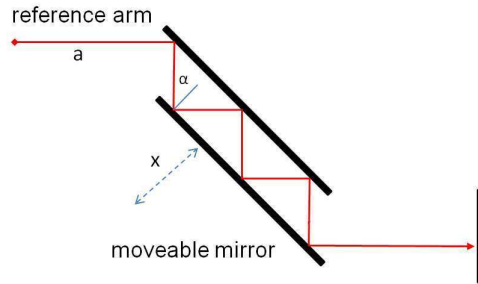
Figure 5.4: Increasing the optical resolution by keeping small moving distances.

is increased while keeping the moving displacement of the mirror small. This enables a high resolution with a fast recording time. Note that the beam position moves on the end mirror of the reference arm but not at the beamsplitter when passed back through the reference arm. Therefore, the reference beam and the sample beam will always overlap. The optical path length L is given by $L = 2(2n)\frac{x}{\cos(\alpha)}$ with α as incident angle, n: number of reflections on the moved mirror, x: moving distance of the mirror. This is an additional factor of $2n\frac{1}{\cos(\alpha)}$ compared to the conventional optical path length x in an FTIR. The reference arm length of about 25cm is found to be stable enough for the measurement (in the climatized laboratory). The interferograms were recorded with an oscilloscope (Wavesurfer 422,lecroy.com). The resolution is theoretically given by the number of reflections and the translation distance of the mirror, but currently limited through nonlinearity in the mirror translation stage (P-628, pi.ws). This can be overcome (as shown in [78]) by off-line resampling according to the frequency calibration interferograms taken with a CO_2 laser beam, or by calibrating the translation stage movement with a capacitive sensor (already included in the translation

stage). In the following measurements we haven't fixed this issue yet.

For recording an approach curve, necessary for proving true near-field character, the moving mirror is placed in the white-light position (all wavelengths interfere constructively) of the interferometer. This position can be found easily by monitoring the interferogram and decreasing the moving distance of the mirror until the interferogram shows only the white-light position (max. signal strength).

5.3 Results and discussions

Recording a continuous near-field spectrum in one single measurement represents the next logical step forward concerning s-SNOM. The possibility of recording an interferogram presents an additional new source of analyzing the near-field tip-sample interaction. This is a unique feature currently only provided by our technique. In the following, we present first continuous near-field spectra in amplitude and phase taken on silicon carbide and gold samples. Approach curves confirm their near-field character. Finally, we discuss the interferograms and show their potential for further research.

5.3.1 Silicon carbide and gold near-field spectra in amplitude and phase

Near-field spectra in amplitude and phase of silicon carbide (SiC) and gold (Au) are presented in Fig.5.5 for the demodulation order of n_1 and n_2. The n_1 demodulated spectra, called s_1,
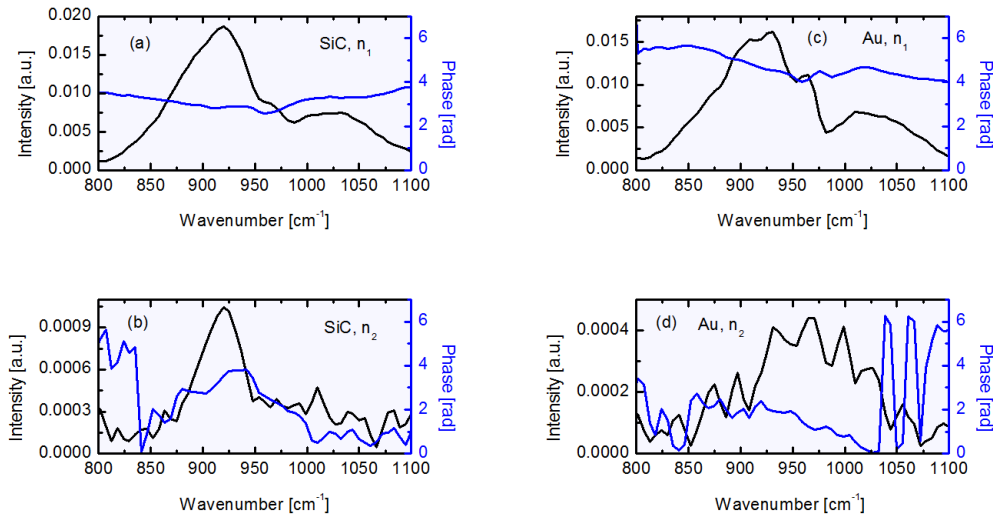
Figure 5.5: Continuous near-field spectra in amplitude and phase for SiC (a,b) and Au (c,d)

are dominated by the background as expected. Therefore the spectrum is similar to the so-called "illumination spectrum" [100] which is the backscattered light of the tip and sample without demodulation. It is interesting that both s_1 spectra are similar to each other, which shouldn't be as for the Au spectra no SiC Fresnel coefficient has to be multiplied to achieve the correct "illumination spectrum". A reason for the similarity could be the illumination onto the tip, if directly or over reflection on the sample[2] [100]. At n_2 the background is

---

[2]The Au was coated in strips onto the SiC

much better suppressed, and we record near-field spectra in amplitude and phase similar as it has been measured with monochromatic infrared s-SNOM. In the case of Au (d) no spectral dependence of the near-field interaction is expected. For SiC (b) a sharp peak with a width of $20\,\text{cm}^{-1}$ at $930\,\text{cm}^{-1}$ should arise [101], but we observe only the Restrahlenbande. There are two reasons why we haven't detected the near-field resonance of SiC. First, the spectral resolution was probably a bit too bad and second, it is well-known that using a damaged tip will not show anymore the near-field resonance due contamination of the tip. A tip can be damaged within a few hours or even during some minutes, depending on the tapping conditions, cantilever and sample properties[3]. Nevertheless we have observed first evidence of the SiC near-field resonance as shown in Fig.5.6 where a peak at the expected wavelength appears, though the peak is to small probably due missing spectral resolution. In Fig.5.7 we
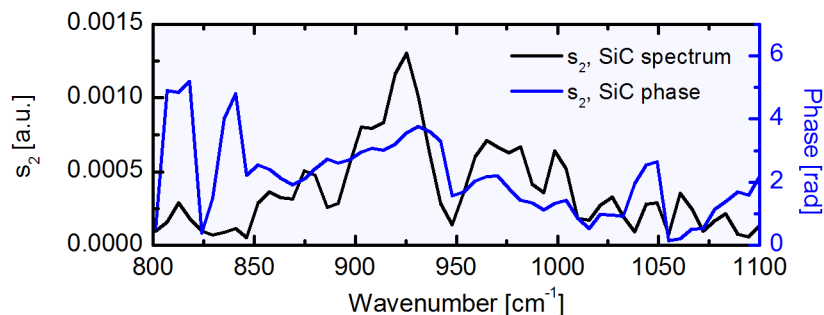
Figure 5.6: First evidence of the SiC near-field resonance

compare in (a) directly the obtained s_2 signals, and in (b) we have divided the s_2 SiC signal through the s_2 Au one as well as the Au phase is subtracted from the SiC one. The obtained curves follows the same shape compared to sequential s-SNOM measurements, supporting that we are measuring near-field signals [100].

The recorded signals are very weak but nevertheless we have found many indications that they represent true near-field spectra in amplitude and phase. The final proof for true near-field spectra is done through so-called approach curves which we present in the next subsection.

5.3.2 Approach curves

True near-field signals are currently approved through the analysis of so-called approach curves. Concerning broadband illumination this has not been shown yet. Thereby the sample is retracted from the tip, continuously recording the signal whereas the moving mirror is kept stable in the white-light position of the interferometer. As the near-field is confined to the surface of the probe, one should see an exponential decay of the intensity if the background is sufficient suppressed. If not, the measured signal (from the background) will periodically rise and fall again over a larger distance because of an interference effect [83]. Due the weakness of the broadband signal, approach curves are very difficult to record. The retraction had to last several seconds for a strong enough signal. Fig.5.8 shows the s_1 and s_2 near-field approach curves for SiC. As expected for s_1 the background is not suppressed leading to a rise in the signal strength at a greater distance [83,102]. The s_2 should contain already much less

---

[3]private communication, Dr. Rainer Hillenbrand, Dr. Andreas Huber
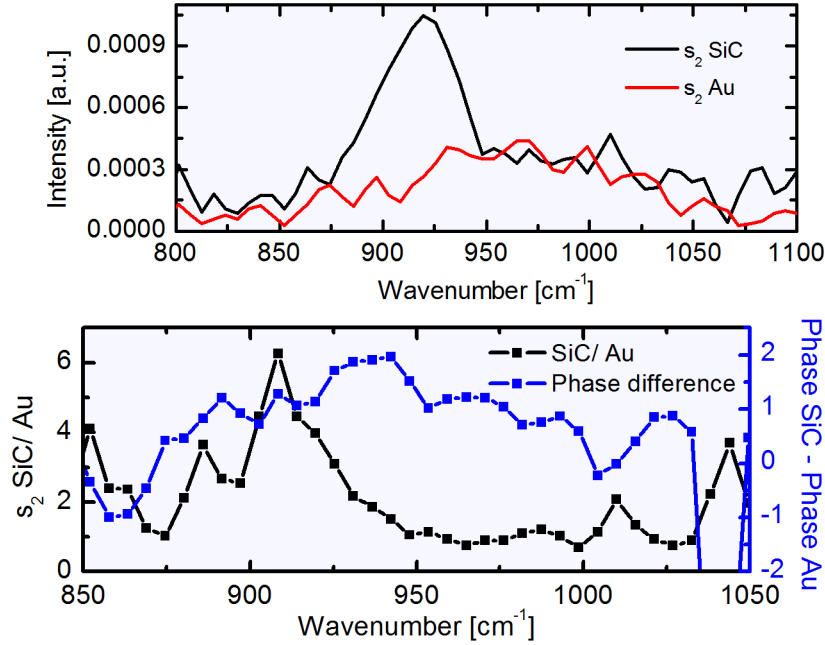
Figure 5.7: SiC and Au comparison, see text for details
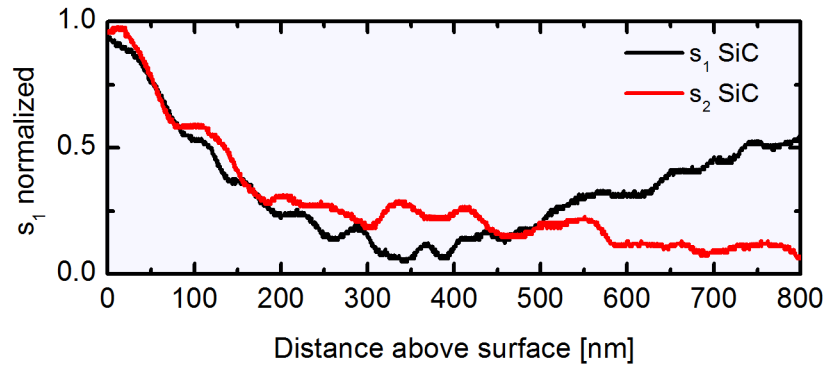
Figure 5.8: Approach curves on SiC for s_1 and s_2. Background signal is still contained in s_1.

background signal which is clearly observed as the signal does not rise anymore like s_1. Hence, the s_2 spectrum is dominated by the near-field but not the background signal. It has been shown with CO_2 lasers that for mid-infrared near-field spectra one should record at least the second demodulated order signal. In Fig.5.9 we compare the s_2 approach curves taken on gold by the broadband illumination (red) and an attenuated CO_2 laser (black). The same decay characteristic is observed which is an additional confirmation that the measured broadband approach curve results from the near-field. With these approach curves we have proven for the first time that continuous near-field spectra in amplitude and phase can be recorded.

5.3.3 "Near-field" interferogram

With our technique we can obtain the sample's properties not only by the near-field spectra in amplitude and phase but also through the recorded interferograms. This is a unique
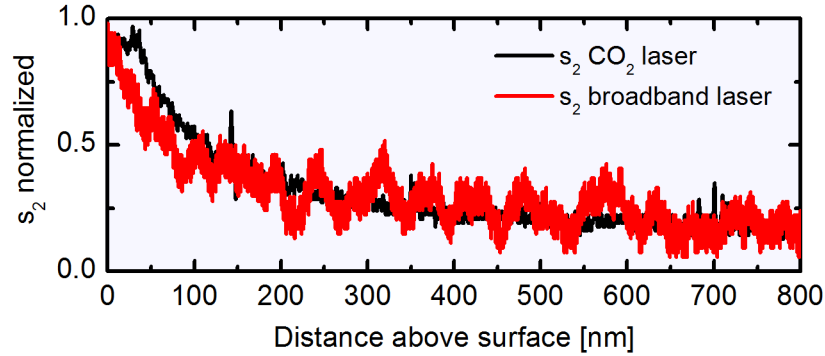
Figure 5.9: Broadband approach curve on Au compared with an approach curve by a CO_2 laser.

feature of our Fourier-transform s-SNOM. The potential of this analysis method has to be still explored. Following we will show some first aspects gained through the interferogram analysis. Fig.5.10 presents the interferogram taken at the surface of SiC (a) and $3\mu m$ above (b) at the demodulation order n_1. In the approached case (a) a long interference part (A) is visible which disappears in the retracted case (b) which consists only of background. We assume that this is the contribution rising from the near-field interaction. Furthermore, as the approach curves have already shown, a larger background dominates the interferogram.
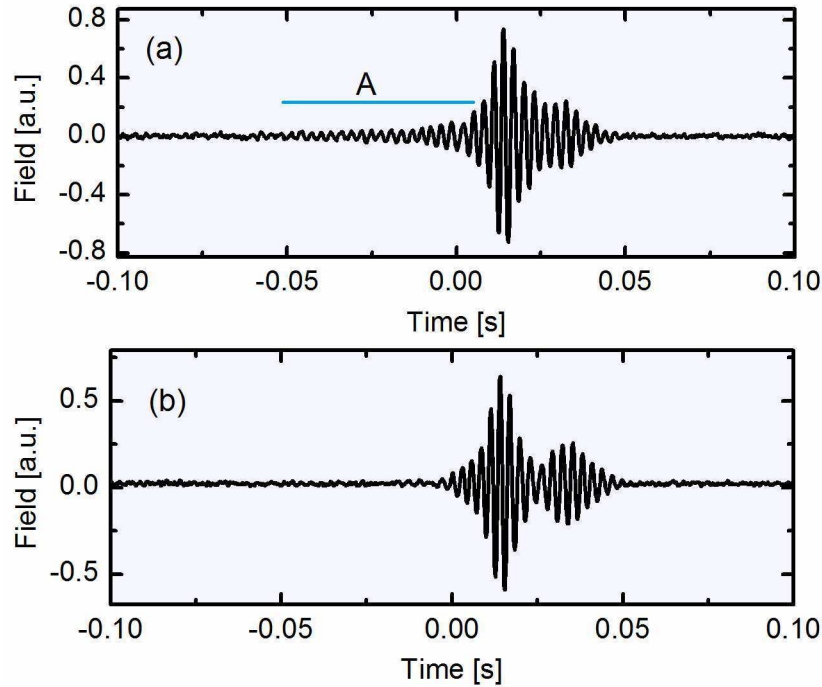
Figure 5.10: Interferograms (n_1) taken on SiC in the (a) approached case and (b) $3\mu m$ above the sample's surface.

The corresponding spectra are shown in Fig.5.11.
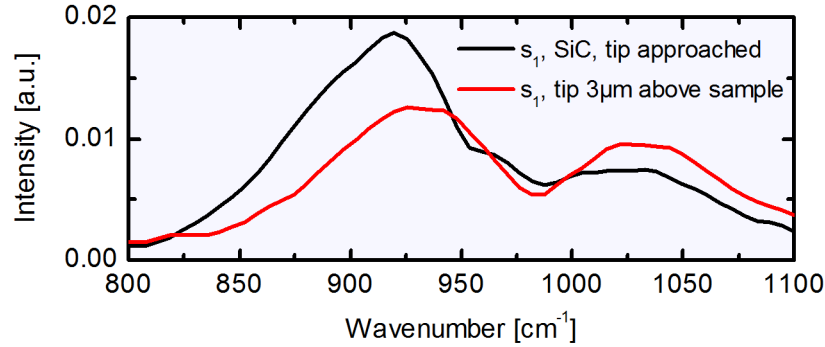
Figure 5.11: Corresponding spectra of Fig.5.10.

Fig.5.12 shows the subtraction of the approached interferogram minus the retracted one. Part A is again the near-field contribution and part B very probably still presents a larger background signal. This can be explained by the way of illumination onto the tip apex-sample region [100]. Another way of illumination can completely avoid part B [78] and only show Part A as in [78]. The near-field contribution can be used as well for confirming true near-field signals, alternatively to approach curves.
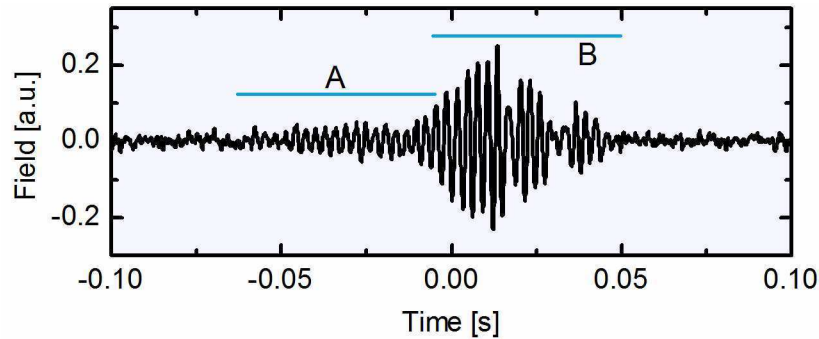
Figure 5.12: Resulting interferogram by subtraction of Fig.5.10 (a)-(b). A: near-field contribution, B: residual background

The prolonged response due to the phonon resonance in SiC of part A marks the high quality factor due the substantial energy stored in the cavity formed by the tip apex and the sample. This prolonged response is probably the first evidence of free induction decay (FID) in a classical near-field coupled system, namely a scatter close to a material surface [78]. Differently materials will have a different long FID as shown in Fig.5.13 Therefore we compared the interferograms (n_1) of SiC and Au. The prolonged response of Au is more "covered" by the background which indicates that it is shorter as the one of SiC. This is better emphasized in the measurements in [78]. But going into the field of FID is beyond the scope of this chapter [78]. In Fig.5.13 we observe another interesting behavior. As we can see, the SiC interferogram (including the background) precedes the gold one, although these measurements were done in the same measurement series without changing the illuminating or recording conditions. The reason is not yet clear but as the background is shifted too one could think about a slightly different attraction strength between the gold-to-tip-apex and SiC-to-tip-apex system which
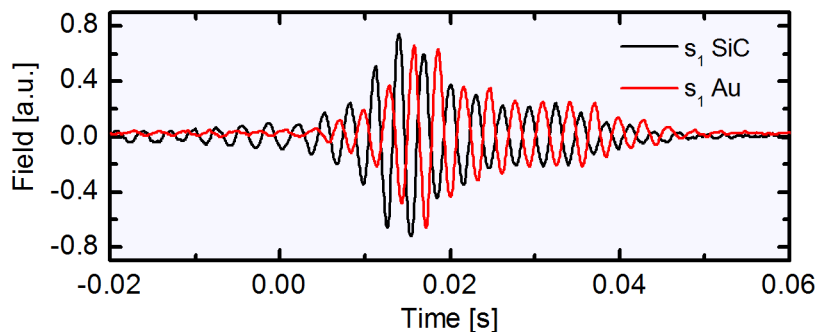
Figure 5.13: Comparison of the SiC and Au interferogram (n_1).

would result in a slightly different path length.

On the basis of the interferograms, an additional source of information has been added to explore material properties and interactions on the nanoscale.

5.4 Outlook

We have demonstrated broadband s-SNOM and shown its potential with respect to nanoscale spectroscopy. Due to the very weak broadband source we were currently limited to proof-of-principle measurements and had to average several spectra to decrease the noise. Therefore, the key question for further applications addresses the mid-infrared broadband power at MHz repetition rate. Generating mid-infrared broadband spectra by difference frequency generation in GaSe will be the most promising and simplest way. But using a broadband Ti:Sapphire femtosecond laser at 800nm will not further improve the situation as the mid-infrared power of around 10μW is currently already limited by two photon absorption (TPA) in GaSe. To increase the power, one has to use a laser-system above the TPA region of 1.5μm for GaSe. During the last years several promising and simple laser systems concerning the mentioned problem have been published yielding a power up to 100μW [77] in the MIR. Currently, such a laser-system has replaced our old Ti:Sapphire based one. A totally different approach could be the use of a supercontinuum spectrum [14] generated in photonic crystal fibers (PCF) as discussed in chapter 1.2.4. Routinely, such spectra can cover the visible part and, depending on the fiber and laser source, can go up to 5μm [103]. Such sources could be very interesting reaching the spectral range around 5μm which is of interest to many vibrational samples. Probably the simplest approach is replacing the laser-system by a thermal emitter. Recently, first promising results have been published [97].

With a stronger broadband source, respectively improved detectors, the measurement time for a pixel will decrease. However, it is questionable if pictures can be recorded like done with a monochromatic s-SNOM. But this might not be a strong limitation. Most of the sample's relevant information does not require a full picture but only some pixels or a linescan at the relevant sample positions, e.g. in doped nanowires [89] or field enhancement in nanogaps [93, 104, 105]. A last approach which can improve the signal essentially is the shape of the cantilever tip-apex. A suitable design increases the amount of backscattered light.[4] We observed indications of this behavior by damaging the tip on purpose, but we couldn't

---

[4]private communication, Prof. Dr. Thomas Taubner, RWTH Aachen University

investigate it in detail.

We also want to draw your attention to a possible combination of the s-SNOM with our pulse compressed chirped pulse oscillator (see 2) for pump-probe spectroscopy.

In the near future, samples with a pronounced spectral near-field characteristic can be investigated, like e.g. conductivity phenomena or plasmonic resonators phonon resonances for chemical identification. As soon as a more broadband MIR power is available one can exploit other topics as well which are currently under investigation with monochromatic s-SNOM. Many mentioned improvements are already in progress and should allow an efficient operation of the broadband s-SNOM, making it a truly spectroscopic tool.

5.5   Summary and conclusions

Current s-SNOM techniques lack on being a true spectroscopic tool. We closed this gap by combining s-SNOM with dispersive Fourier-transform spectroscopy and presented for the first time near-field spectra in amplitude and phase of SiC and Au. Recording approach curves we proved the near-field character as well. This demonstrated the potential of our technique. Our experimental setup can without any problem be adapted to other spectral ranges, like the visible or terahertz ones. New laser systems and detectors will reduce the measurement time, enabling line-scans and small pictures. Furthermore, analyzing the interferograms one receives additional knowledge of the coupled near-field systems of material surface and tip apex which is currently not possible with other techniques. Thus, the combination of s-SNOM with dispersive Fourier-transform spectroscopy presents a powerful tool for nanoscale spectroscopy.

Chapter 6

Conclusions

The motivation of this thesis was to do pulse compression with high energy pulses at MHz repetition rates which can then be used for several experiments like high harmonic generation or ultrafast spectroscopy to increase the signal-to-noise ratio and reduce measurement time. With the development and demonstration of the chirped pulse compression concept we have built such a desired laser system for daily use.

Chirped Pulse Compression ...
> With the invented concept of chirped pulse compression we have successfully overcome the current energy limitations due to self-focusing in fibers, yielding the same results as in the Fourier-limit case. The concept is not limited to a special laser or certain input parameters, and should be transferable to other pulse compression schemes using self-phase modulation (e.g. hollow core fiber compression). Optimizing all parameters of the setup one can again improve the output values. The measured stability, polarization ratio and the compact setup makes the combination of our concept with a chirped pulse oscillator a very interesting alternative to MHz-NOPAs which operate with similar output values in energy and pulse duration but have a more complex setup and a worse stability, and are therefore not suitable for many research groups. Our setup is ready for applications in ultrafast spectroscopy, high harmonic generation, material processing and much more.

Few-cycle pulse compression ...
> We demonstrated a 6fs pulse compressed starting the laser's 55fs, using only one fiber stage. Further optimizing the setup's parameters sub-5fs should be realistic. The combination of our 6fs beam with a white-light beam, generated in a crystal from the original 55fs beam, presents an interesting alternative for ultrafast spectroscopy at MHz repetition rate e.g. photoinduced electron transfer samples, like solar-cells. Currently such measurements can only be done with kHz laser systems.

Dispersion transfer ...
> We showed that the transfer of the input GDD to the output GDD after spectral broadening by self-phase modulation behaves significantly different than expected and cannot be explained through the increased spectral bandwidth only. A satisfying explanation has not been found yet. The special GDD transfer property allows to keep the chirped pulse compression setup nearly unchanged over a large input chirping range; a clear advantage. We believe that our measurements will help also to understand other recent

experiments using chirped input beams, e.g. the rise of self-compression in filamentation at some certain well-defined input chirp values [27]. The influence of chirp to nonlinear processes is definitely larger than previously assumed.

High average power pulse compression with 1030nm laser systems ...
Our >100W average power pulse compression experiments at 1030nm have shown that thermal aspects concerning fibers and self-phase modulation can be controlled and do not represent the a fundamental limitation. However, the current limit is given through the thermal lens of the optical isolator which decrease the M^2 of the beam so that one cannot couple into the fiber anymore. In the near future one will therefore be restricted to around 200W because no better isolators exist. Comparing with the experiments at 800nm we found a couple of differences (transmission, polarization) which require a detailed measurement series. Although pulse compression with 1030nm laser systems can already be used for further experiments, it has not reached the level of the Ti:Sapphire experiments yet.

Chirped mirrors ...
Chirped mirrors are a very powerful and essential tool for dispersion management. But using broadband chirped mirrors which rely on the (necessary) concept of canceling dispersion ripples one needs to measure their group delay dispersion (GDD) curve as otherwise one cannot select the canceling chirped mirror pair. Relying on the design curves clearly is not sufficient Through our measurements we have found that every chirped mirror has a different spectral shift of its GDD curve compared to the other chirped mirrors which should have identical properties. As all these mirrors are manufactured in the same run we believe that the reason lies in the coating machine. Probably, the coating setup does not allow a sufficiently constant layer thickness on each mirror. Measuring the spectral reflection curve of broadband chirped mirrors one can often make a first selection which mirrors work well together.

s-SNOM ...
True continuous near-field spectra in amplitude and phase recorded in one single measurement have been demonstrated for the first time by combining Fourier-transform spectroscopy with a scattering scanning near-field optical microscope. Through our technique we closed the gap of an insufficient spectral recording by monochromatic s-SNOM and raised it finally to a true spectroscopic tool. Direct applications in nanoscience can be any kind of doped semiconductor materials. New, stronger laser systems for broadband mid-infrared generation will increase the power of the beam enabling the recording of pictures of the sample instead of the current single pixels or linescans. Specially designed tip scatters are another possibility to increase the signal. Our approach opens an additional analysis method by recording the "near-field" interferograms. Broadband s-SNOM stands at the beginning of demonstrating its full potential for the field of nanoscience, but the first steps have been presented in these thesis.

Bibliography

[1] Govind P. Agrawal. *Nonlinear Fiber Optics*. Academic Press, third edition edition, 2001.

[2] Robert R. Alfano, editor. *The Supercontinuum Laser Source*. Springer, 2006.

[3] Weiner A. M. *Ultrafast Optics*. Wiley, 2009.

[4] http://en.wikipedia.org/wiki/Self-phase_modulation.

[5] Frank Träger, editor. *Springer Handbook of Lasers and Optics*. Springer, 2007.

[6] D. Grischkowsky and A. C. Balant. Optical pulse compression based on enhanced frequency chirping. *Applied Physics Letters*, 41(1):1–3, 1982.

[7] A. A. Amorim, M. V. Tognetti, P. Oliveira, J. L. Silva, L. M. Bernardo, F. X. Kärtner, and H. M. Crespo. Sub-two-cycle pulses by soliton self-compression in highly nonlinear photonic crystal fibers. *Opt. Lett.*, 34(24):3851–3853, Dec 2009.

[8] W. J. Tomlinson, R. H. Stolen, and C. V. Shank. Compression of optical pulses chirped by self-phase modulation in fibers. *J. Opt. Soc. Am. B*, 1(2):139–149, 1984.

[9] W. J. Tomlinson, R. H. Stolen, and A. M. Johnson. Optical wave breaking of pulses in nonlinear optical fibers. *Opt. Lett.*, 10(9):457–459, 1985.

[10] J. C. Knight, T. A. Birks, P. St. J. Russell, and D. M. Atkin. All-silica single-mode optical fiber with photonic crystal cladding. *Opt. Lett.*, 21(19):1547–1549, Oct 1996.

[11] T. A. Birks, J. C. Knight, and P. St.J. Russell. Endlessly single-mode photonic crystal fiber. *Opt. Lett.*, 22(13):961–963, Jul 1997.

[12] J. C. Knight, J. Broeng, T. A. Birks, and P. St. J. Russell. Photonic band gap guidance in optical fibers. *Science*, 282(5393):1476–1478, 1998.

[13] Niels Asger Mortensen. Effective area of photonic crystal fibers. *Opt. Express*, 10(7):341–348, Apr 2002.

[14] John M. Dudley, Goëry Genty, and Stéphane Coen. Supercontinuum generation in photonic crystal fiber. *Rev. Mod. Phys.*, 78(4):1135–1184, Oct 2006.

[15] Mark Foster, Alexander Gaeta, Qiang Cao, and Rick Trebino. Soliton-effect compression of supercontinuum to few-cycle durations in photonic nanowires. *Opt. Express*, 13(18):6848–6855, Sep 2005.

[16] Gunther Krauss, Sebastian Lohss, Tobias Hanke, Alexander Sell, Stefan Eggert, Rupert Huber, and Alfred Leitenstorfer. Synthesis of a single cycle of light with compact erbium-doped fibre technology. *Nat Photon*, 4(1):33–36, January 2010.

[17] M. Nisoli, S. De Silvestri, and O. Svelto. Generation of high energy 10 fs pulses by a new pulse compression technique. *Applied Physics Letters*, 68(20):2793–2795, 1996.

[18] M. Nisoli, S. De Silvestri, O. Svelto, R. Szipöcs, K. Ferencz, Ch. Spielmann, S. Sartania, and F. Krausz. Compression of high-energy laser pulses below 5 fs. *Opt. Lett.*, 22(8):522–524, 1997.

[19] Akira Suda, Masatoshi Hatayama, Keigo Nagasaka, and Katsumi Midorikawa. Generation of sub-10-fs, 5-mj-optical pulses using a hollow fiber with a pressure gradient. *Applied Physics Letters*, 86(11):111116, 2005.

[20] Eiichi Matsubara, Keisaku Yamane, Taro Sekikawa, and Mikio Yamashita. Generation of 2.6 fs optical pulses using induced-phase modulation in a gas-filled hollow fiber. *J. Opt. Soc. Am. B*, 24(4):985–989, 2007.

[21] Selcuk Akturk, Cord L. Arnold, Bing Zhou, and Andre Mysyrowicz. High-energy ultrashort laser pulse compression in hollow planar waveguides. *Opt. Lett.*, 34(9):1462–1464, May 2009.

[22] B. F. Mansour, H. Anis, D. Zeidler, P. B. Corkum, and D. M. Villeneuve. Generation of 11 fs pulses by using hollow-core gas-filled fibers at a 100 khz repetition rate. *Opt. Lett.*, 31(21):3185–3187, Nov 2006.

[23] Steffen Hädrich, Jan Rothhardt, Tino Eidam, Jens Limpert, and Andreas Tünnermann. High energy ultrashort pulses via hollow fiber compression of a fiber chirped pulse amplification system. *Opt. Express*, 17(5):3913–3922, Mar 2009.

[24] C. Vozzi, M. Nisoli, G. Sansone, S. Stagira, and S. De Silvestri. Optimal spectral broadening in hollow-fiber compressor systems. *Applied Physics B: Lasers and Optics*, 80:285–289, 2005. 10.1007/s00340-004-1721-1.

[25] A. Braun, G. Korn, X. Liu, D. Du, J. Squier, and G. Mourou. Self-channeling of high-peak-power femtosecond laser pulses in air. *Opt. Lett.*, 20(1):73–75, Jan 1995.

[26] G. Steinmeyer and G. Stibenz. Generation of sub-4-fs pulses via compression of a white-light continuum using only chirped mirrors. *Applied Physics B: Lasers and Optics*, 82:175–181, 2006. 10.1007/s00340-005-2065-1.

[27] O. Varela, B. Alonso, I. J. Sola, J. San Román, A. Zaïr, C. Méndez, and L. Roso. Self-compression controlled by the chirp of the input pulse. *Opt. Lett.*, 35(21):3649–3651, Nov 2010.

[28] Alexander L. Gaeta. Catastrophic collapse of ultrashort pulses. *Phys. Rev. Lett.*, 84(16):3582–3585, Apr 2000.

[29] T. Südmeyer, F. Brunner, E. Innerhofer, R. Paschotta, K. Furusawa, J. C. Baggett, T. M. Monro, D. J. Richardson, and U. Keller. Nonlinear femtosecond pulse compression at high average power levels by use of a large-mode-area holey fiber. *Opt. Lett.*, 28(20):1951–1953, 2003.

[30] Frédéric Druon and Patrick Georges. Pulse-compression down to 20 fs using a photonic crystal fiber seeded by a diode-pumped yb:sys laser at 1070 nm. *Opt. Express*, 12(15):3383–3396, Jul 2004.

[31] Andy Steinmann, Alexander Killi, Guido Palmer, Thomas Binhammer, and Uwe Morgner. Generation of few-cycle pulses directly from a mhz-nopa. *Opt. Express*, 14(22):10627–10630, 2006.

[32] T. Eidam, F. Röser, O. Schmidt, J. Limpert, and A. Tünnermann. 57 w, 27 fs pulses from a fiber laser system using nonlinear compression. *Applied Physics B: Lasers and Optics*, 92(1):9–12, 2008.

[33] Igor Martial, Dimitris Papadopulos, Marc Hanna, Frédéric Druon, and Patrick Georges. Nonlinear compression in a rod-type fiber for high energy ultrashort pulse generation. *Opt. Express*, 17(13):11155–11160, Jun 2009.

[34] S Naumov, A Fernandez, R Graf, P Dombi, F Krausz, and A Apolonski. Approaching the microjoule frontier with femtosecond laser oscillators. *New Journal of Physics*, 7(1):216, 2005.

[35] F. Röser, D. Schimpf, O. Schmidt, B. Ortaç, K. Rademaker, J. Limpert, and A. Tünnermann. 90 w average power 100 μj energy femtosecond fiber chirped-pulse amplification system. *Opt. Lett.*, 32(15):2230–2232, Aug 2007.

[36] P. Russbueldt, T. Mans, J. Weitenberg, H. D. Hoffmann, and R. Poprawe. Compact diode-pumped 1.1 kw yb:yag innoslab femtosecond amplifier. *Opt. Lett.*, 35(24):4169–4171, Dec 2010.

[37] Moritz Emons, Andy Steinmann, Thomas Binhammer, Guido Palmer, Marcel Schultze, and Uwe Morgner. Sub-10-fs pulses from a mhz-nopa with pulse energies of 0.4 μj. *Opt. Express*, 18(2):1191–1196, 2010.

[38] Christian Schriever, Stefan Lochbrunner, Patrizia Krok, and Eberhard Riedle. Tunable pulses from below 300 to 970 nm with durations down to 14 fs based on a 2 mhz ytterbium-doped fiber system. *Opt. Lett.*, 33(2):192–194, 2008.

[39] J. Rothhardt, S. Hädrich, D. N. Schimpf, J. Limpert, and A. Tünnermann. High repetition rate fiber amplifier pumped sub-20 fs optical parametric amplifier. *Opt. Express*, 15(25):16729–16736, 2007.

[40] Thomas Brabec and Ferenc Krausz. Intense few-cycle laser fields: Frontiers of nonlinear optics. *Rev. Mod. Phys.*, 72(2):545–591, Apr 2000.

[41] Seungchul Kim, Jonghan Jin, Young-Jin Kim, In-Yong Park, Yunseok Kim, and Seung-Woo Kim. High-harmonic generation by resonant plasmon field enhancement. *Nature*, 453:757–760, 2008.

[42] Roberto Osellame, N. Chiodo, V. Maselli, A. Yin, M. Zavelani-Rossi, G. Cerullo, P. Laporta, L. Aiello, S. De Nicola, P. Ferraro, A. Finizio, and G. Pierattini. Optical properties of waveguides written by a 26 mhz stretched cavity ti:sapphire femtosecond oscillator. *Opt. Express*, 13(2):612–620, Jan 2005.

[43] A. Fernandez, T. Fuji, A. Poppe, A. Fürbach, F. Krausz, and A. Apolonski. Chirped-pulse oscillators:?a route to high-power femtosecond pulseswithout external amplification. *Opt. Lett.*, 29(12):1366–1368, 2004.

[44] Martin Siegel, Nils Pfullmann, Guido Palmer, Stefan Rausch, Thomas Binhammer, Milutin Kovacev, and Uwe Morgner. Microjoule pulse energy from a chirped-pulse ti:sapphire oscillator with cavity dumping. *Opt. Lett.*, 34(6):740–742, Mar 2009.

[45] F. Röser, J. Rothhard, B. Ortac, A. Liem, O. Schmidt, T. Schreiber, J. Limpert, and A. Tünnermann. 131 w 220 fs fiber laser system. *Opt. Lett.*, 30(20):2754–2756, Oct 2005.

[46] R. L. Fork, C. H. Brito Cruz, P. C. Becker, and C. V. Shank. Compression of optical pulses to six femtoseconds by using cubic phase compensation. *Opt. Lett.*, 12(7):483–485, 1987.

[47] Andrius Baltuska, Zhiyi Wei, Maxim S. Pshenichnikov, and Douwe A. Wiersma. Optical pulse compression to 5 fs at a 1-mhz repetition rate. *Opt. Lett.*, 22(2):102–104, 1997.

[48] V.S. Yakovlev, P. Dombi, G. Tempea, C. Lemell, J. Burgdörfer, T. Udem, and A. Apolonski. Phase-stabilized 4-fs pulses at the full oscillator repetition rate for a photoemission experiment. *Applied Physics B: Lasers and Optics*, 76:329–332, 2003.

[49] T. Südmeyer, S. V. Marchese, S. Hashimoto, C. R. E. Baer, G. Gingras, B. Witzel, and U. Keller. Femtosecond laser oscillators for high-field science. *Nat Photon*, 2(10):599–604, October 2008.

[50] T. Ganz, V. Pervak, A. Apolonski, and P. Baum. 16 fs, 350 nj pulses at 5 mhz repetition rate delivered by chirped pulse compression in fibers. *Opt. Lett.*, 36(7):1107–1109, Apr 2011.

[51] Donna Strickland and Gerard Mourou. Compression of amplified chirped optical pulses. *Optics Communications*, 56(3):219 – 221, 1985.

[52] V. Pervak, I. Ahmad, M. K. Trubetskov, A. V. Tikhonravov, and F. Krausz. Double-angle multilayer mirrors with smoothdispersion characteristics. *Opt. Express*, 17(10):7943–7951, 2009.

[53] A. Apolonski, P. Dombi, G. G. Paulus, M. Kakehata, R. Holzwarth, Th. Udem, Ch. Lemell, K. Torizuka, J. Burgdörfer, T. W. Hänsch, and F. Krausz. Observation of light-phase-sensitive photoemission from a metal. *Phys. Rev. Lett.*, 92(7):073902, Feb 2004.

[54] Ian A. Howard, Ralf Mauer, Michael Meister, and Fre?de?ric Laquai. Effect of morphology on ultrafast free carrier generation in polythiophene:fullerene organic solar cells. *Journal of the American Chemical Society*, 132(42):14866–14876, 2010.

[55] Christoph J. Brabec, Gerald Zerza, Giulio Cerullo, Sandro De Silvestri, Silvia Luzzati, Jan C. Hummelen, and Serdar Sariciftci. Tracing photoinduced electron transfer process in conjugated polymer/fullerene bulk heterojunctions in real time. *Chemical Physics Letters*, 340(3-4):232 – 236, 2001.

[56] Roberto Osellame, N. Chiodo, V. Maselli, A. Yin, M. Zavelani-Rossi, G. Cerullo, P. Laporta, L. Aiello, S. De Nicola, P. Ferraro, A. Finizio, and G. Pierattini. Optical properties of waveguides written by a 26 mhz stretched cavity ti:sapphire femtosecond oscillator. *Opt. Express*, 13(2):612–620, Jan 2005.

[57] M. Aidelsburger, F. O. Kirchner, F. Krausz, and P. Baum. Single-electron pulses for ultrafast diffraction. *Proceedings of the National Academy of Sciences*, 107(46):19714–19719, 2010.

[58] A. Fernández, A. Verhoef, V. Pervak, G. Lermann, F. Krausz, and A. Apolonski. Generation of 60-nj sub-40-fs pulses at 70 mhz repetition rate from a ti:sapphire chirped pulse-oscillator. *Applied Physics B: Lasers and Optics*, 87:395–398, 2007. 10.1007/s00340-007-2634-6.

[59] Joshua E. Rothenberg. Femtosecond optical shocks and wave breaking in fiber propagation. *J. Opt. Soc. Am. B*, 6(12):2392–2401, 1989.

[60] Robert W. Boyd. *Nonlinear Optics*. Academic Press, Inc, 1992.

[61] M. Lenzner, J. Krüger, S. Sartania, Z. Cheng, Ch. Spielmann, G. Mourou, W. Kautek, and F. Krausz. Femtosecond optical breakdown in dielectrics. *Phys. Rev. Lett.*, 80(18):4076–4079, May 1998.

[62] G. Steinmeyer. Dispersion compensation by microstructured optical devices in ultrafast optics. *Applied Physics A: Materials Science & Processing*, 79:1663–1671, 2004. 10.1007/s00339-004-2679-x.

[63] F. X. Kärtner, N. Matuschek, T. Schibli, U. Keller, H. A. Haus, C. Heine, R. Morf, V. Scheuer, M. Tilsch, and T. Tschudi. Design and fabrication of double-chirped mirrors. *Opt. Lett.*, 22(11):831–833, Jun 1997.

[64] F. X. Kärtner, U. Morgner, R. Ell, T. Schibli, J. G. Fujimoto, E. P. Ippen, V. Scheuer, G. Angelow, and T. Tschudi. Ultrabroadband double-chirped mirror pairs for generation of octave spectra. *J. Opt. Soc. Am. B*, 18(6):882–885, Jun 2001.

[65] G. Steinmeyer. Brewster-angled chirped mirrors for high-fidelity dispersion compensation and bandwidths exceeding one optical octave. *Opt. Express*, 11(19):2385–2396, Sep 2003.

[66] Mitsuo Takeda, Hideki Ina, and Seiji Kobayashi. Fourier-transform method of fringe-pattern analysis for computer-based topography and interferometry. *J. Opt. Soc. Am.*, 72(1):156–160, Jan 1982.

[67] Peter Baum, Markus Breuer, Eberhard Riedle, and Günter Steinmeyer. Brewster-angled chirped mirrors for broadband pulse compression without dispersion oscillations. *Opt. Lett.*, 31(14):2220–2222, Jul 2006.

[68] Ioachim Pupeza, Tino Eidam, Jens Rauschenberger, Birgitta Bernhardt, Akira Ozawa, Ernst Fill, Alexander Apolonski, Thomas Udem, Jens Limpert, Zeyad A. Alahmed, Abdallah M. Azzeer, Andreas Tünnermann, Theodor W. Hänsch, and Ferenc Krausz. Power scaling of a high-repetition-rate enhancement cavity. *Opt. Lett.*, 35(12):2052–2054, Jun 2010.

[69] Lawrence Shah, Martin E. Fermann, Jay W. Dawson, and Christopher P. J. Barty. Micromachining with a 50 w, 50 μj, subpicosecond fiber laser system. *Opt. Express*, 14(25):12546–12551, Dec 2006.

[70] Franz Tavella, Andrius Marcinkevicius, and Ferenc Krausz. 90 mj parametric chirped pulse amplification of 10 fs pulses. *Opt. Express*, 14(26):12822–12827, Dec 2006.

[71] T. Südmeyer, C. Kränkel, C. Baer, O. Heckl, C. Saraceno, M. Golling, R. Peters, K. Petermann, G. Huber, and U. Keller. High-power ultrafast thin disk laser oscillators and their potential for sub-100-femtosecond pulse generation. *Applied Physics B: Lasers and Optics*, 97:281–295, 2009. 10.1007/s00340-009-3700-z.

[72] Claude Rolland and P. B. Corkum. Compression of high-power optical pulses. *J. Opt. Soc. Am. B*, 5(3):641–647, 1988.

[73] Benjamin Eggleton, Charles Kerbage, Paul Westbrook, Robert Windeler, and Arturo Hale. Microstructured optical fiber devices. *Opt. Express*, 9(13):698–713, Dec 2001.

[74] D. Nodop, C. Jauregui, D. Schimpf, J. Limpert, and A. Tünnermann. Efficient high-power generation of visible and mid-infrared light by degenerate four-wave-mixing in a large-mode-area photonic-crystal fiber. *Opt. Lett.*, 34(22):3499–3501, Nov 2009.

[75] W. Wadsworth, N. Joly, J. Knight, T. Birks, F. Biancalana, and P. Russell. Supercontinuum and four-wave mixing with q-switched pulses in endlessly single-mode photonic crystal fibres. *Opt. Express*, 12(2):299–309, Jan 2004.

[76] Guoqing Chang, Li-Jin Chen, and Franz X. Kärtner. Highly efficient cherenkov radiation in photonic crystal fibers for broadband visible wavelength generation. *Opt. Lett.*, 35(14):2361–2363, Jul 2010.

[77] Alessio Gambetta, Roberta Ramponi, and Marco Marangoni. Mid-infrared optical combs from a compact amplified er-doped fiber oscillator. *Opt. Lett.*, 33(22):2671–2673, Nov 2008.

[78] Sergiu Amarie, Thomas Ganz, and Fritz Keilmann. Mid-infrared near-field spectroscopy. *Opt. Express*, 17(24):21794–21801, Nov 2009.

[79] S. Amarie and F. Keilmann. Broadband-infrared assessment of phonon resonance in scattering-type near-field microscopy. *Phys. Rev. B*, 83(4):045404, Jan 2011.

[80] T Ganz, M Brehm, H G von Ribbeck, D W van der Weide, and F Keilmann. Vector frequency-comb fourier-transform spectroscopy for characterizing metamaterials. *New Journal of Physics*, 10(12):123007, 2008.

[81] T. Ganz, H.G. von Ribbeck, M. Brehm, and F. Keilmann. Compact frequency-comb fourier-transform infrared spectrometer. *Optics Communications*, 281(14):3827 – 3830, 2008.

[82] Keilmann F. and Hillenbrand R. *Nano-Optics and Near-Field Optical Microscopy*. ArtechHouse, Norwood, MA,, 2009.

[83] R. Hillenbrand and F. Keilmann. Material-specific mapping of metal/semiconductor/dielectric nanosystems at 10 nm resolution by backscattering near-field optical microscopy. *Applied Physics Letters*, 80(1):25–27, 2002.

[84] A. J. Huber, F. Keilmann, J. Wittborn, J. Aizpurua, and R. Hillenbrand. Terahertz near-field nanoscopy of mobile carriers in single semiconductor nanodevices. *Nano Letters*, 8(11):3766–3770, 2008. PMID: 18837565.

[85] H.-G. von Ribbeck, M. Brehm, D. W. van der Weide, S. Winnerl, O. Drachenko, M. Helm, and F. Keilmann. Spectroscopic thz near-field microscope. *Opt. Express*, 16(5):3430–3438, Mar 2008.

[86] T. Taubner, R. Hillenbrand, and F. Keilmann. Nanoscale polymer recognition by spectral signature in scattering infrared near-field microscopy. *Applied Physics Letters*, 85(21):5064–5066, 2004.

[87] Nenad Ocelic, Andreas Huber, and Rainer Hillenbrand. Pseudoheterodyne detection for background-free near-field spectroscopy. *Applied Physics Letters*, 89(10):101124, 2006.

[88] A. J. Huber, D. Kazantsev, F. Keilmann, J. Wittborn, and R. Hillenbrand. Simultaneous ir material recognition and conductivity mapping by nanoscale near-field microscopy. *Advanced Materials*, 19(17):2209–2212, 2007.

[89] J. M. Stiegler, A. J. Huber, S. L. Diedenhofen, J. Go?mez Rivas, R. E. Algra, E. P. A. M. Bakkers, and R. Hillenbrand. Nanoscale free-carrier profiling of individual semiconductor nanowires by infrared near-field nanoscopy. *Nano Letters*, 10(4):1387–1392, 2010. PMID: 20302289.

[90] A. Cvitkovic, N. Ocelic, and R. Hillenbrand. Material-specific infrared recognition of single sub-10 nm particles by substrate-enhanced scattering-type near-field microscopy. *Nano Letters*, 7(10):3177–3181, 2007.

[91] A. Huber, N. Ocelic, D. Kazantsev, and R. Hillenbrand. Near-field imaging of mid-infrared surface phonon polariton propagation. *Applied Physics Letters*, 87(8):081103, 2005.

[92] Matthias Rang, Andrew C. Jones, Fei Zhou, Zhi-Yuan Li, Benjamin J. Wiley, Younan Xia, and Markus B. Raschke. Optical near-field mapping of plasmonic nanoprisms. *Nano Letters*, 8(10):3357–3363, 2008. PMID: 18788789.

[93] M. Schnell, Garcia-Etxarr iA., Huber A. J., Crozier K., Aizpurua J., and Hillenbrand R. Controlling the near-field oscillations of loaded plasmonic nanoantennas. *Nat Photon*, 3(5):287–291, May 2009.

[94] Markus Brehm, Albert Schliesser, and Fritz Keilmann. Spectroscopic near-field microscopy using frequency combs in the mid-infrared. *Opt. Express*, 14(23):11222–11233, Nov 2006.

[95] M. M. Qazilbash, M. Brehm, Byung-Gyu Chae, P.-C. Ho, G. O. Andreev, Bong-Jun Kim, Sun Jin Yun, A. V. Balatsky, M. B. Maple, F. Keilmann, Hyun-Tak Kim, and D. N. Basov. Mott transition in vo2 revealed by infrared spectroscopy and nano-imaging. *Science*, 318(5857):1750–1753, 2007.

[96] Markus Brehm, Albert Schliesser, and Fritz Keilmann. Spectroscopic near-field microscopy using frequency combs in the mid-infrared. *Opt. Express*, 14(23):11222–11233, Nov 2006.

[97] F. Huth, M. Schnell, J. Wittborn, N. Ocelic, and R. Hillenbrand. Infrared-spectroscopic nanoimaging with a thermal source. *Nat Mater*, 10(5):352–356, May 2011.

[98] R. A. Kaindl, F. Eickemeyer, M. Woerner, and T. Elsaesser. Broadband phase-matched difference frequency mixing of femtosecond pulses in gase: Experiment and theory. *Applied Physics Letters*, 75(8):1060–1062, 1999.

[99] N. Ocelic. *Quantitative Near-field Phonon-polariton Spectroscopy*. PhD thesis, Technische Universität München, 2007.

[100] Markus Brehm. *Infrarot-Mikrospektroskopie mit einem Nahfeldmikroskop*. PhD thesis, Technische Universität München, 2007.

[101] R. Hillenbrand, T. Taubner, and F. Keilmann. Phonon-enhanced light-matter interaction at the nanometre scale. *Nature*, 418(6894):159–162, July 2002.

[102] R. Hillenbrand and F. Keilmann. Complex optical constants on a subwavelength scale. *Phys. Rev. Lett.*, 85(14):3029–3032, Oct 2000.

[103] P. Domachuk, N. A. Wolchover, M. Cronin-Golomb, A. Wang, A. K. George, C. M. B. Cordeiro, J. C. Knight, and F. G. Omenetto. Over 4000 nm bandwidth of mid-ir supercontinuum generation in sub-centimeter segments of highly nonlinear tellurite pcfs. *Opt. Express*, 16(10):7161–7168, May 2008.

[104] M. Schnell, A. Garcia-Etxarri, J. Alkorta, J. Aizpurua, and R. Hillenbrand. Phase-resolved mapping of the near-field vector and polarization state in nanoscale antenna gaps. *Nano Letters*, 10(9):3524–3528, 2010.

[105] Robert L. Olmon, Matthias Rang, Peter M. Krenz, Brian A. Lail, Laxmikant V. Saraf, Glenn D. Boreman, and Markus B. Raschke. Determination of electric-field, magnetic-field, and electric-current distributions of infrared optical antennas: A near-field optical vector network analyzer. *Phys. Rev. Lett.*, 105(16):167403, Oct 2010.

Chapter 7

Acknowledgement

I am thanking very much Prof. Dr. Krausz for his trust in me and patience. As well as I am thanking Dr. Peter Baum for supervising me during the last years and I wish him all the best for his future. This honor belongs also to Dr. Alexander Apolonskiy, called Sasha, and to Dr. Fritz Keilmann who introduced me into the field of near-field microscopy.

A special thanks goes to Dr. Rainer Hillenbrand. I hope he will finally find the time to write the climbing guide of the Pyrenean. I wish him all the best for his exciting near-field microscopy experiments. A big thank you goes to the members of the former SPM group at the MPI of Biochemistry as well as to the members of Prof. Dr. Baumeister biochemistry group in Martinsried. I will not forget the parties.

A lot of fun we had in Sasha's group. I am thanking everyone for the nice hours and their support for my experiments. A special mention has my co-worker and good friend Friedrich Kirchner deserved, as well as to Stefan Lahme and Fabian Lücking. Without them the time would have been twice as long. I will miss our runs to catch the subway on time and good luck with the "Gas-Wasser-Scheisse". Not to forget is Dr. Peter Russbüldt of the Fraunhofer Institute of Lasertechnique ILT in Aachen. I profited a lot of his experience and knowledge and by the way...Aachen is a very boring town, I nearly died on the weekend there. A big thanks to the ILT Ultrafast group of Dieter Hofmann! I am also thanking the four ladies (Hanieh, Lauryna, Anna-Caroline and Monika) in my office, proving that physics is not limited to men only, at least temporarily. A special thanks goes to Nils Krebs. I enjoyed our climbing session, quite often followed by a beer. Daniel Herrmann and Raphael Tautz shall be not forgotten, as well as Elisabeth Magerl. Thanks for all the nice hours together. As our group is very big I will not mention everyone now, please forgive me but you can be sure that I greatly appreciate your help and the nice time we spend together (and I am now there where you want to be). Finally, I am thanking Rocío Borrego Varillas from Salamanca for her support in some important decisions.

Chapter 8

Curriculum Vitae

Thomas Ganz

08/2011 - present	Laser engineer at "FEMTOLASERS Produktions GmbH" in Vienna, Austria
06/2011	Technology transfer at "FEMTOLASERS Produktions GmbH" in Vienna, Austria
04/2007 - 05/2011	Graduate student in the group of Prof. Dr. Ferenc Krausz at the Max-Planck-Institute of Quantum Optics, Garching, and Ludwig-Maximilians-Universität, Munich, Germany Subject: "Supercontinuum Generation by Chirped Pulse Compression for Ultrafast Spectroscopy and Broadband Near-field Microscopy"
11/2006 - 02/2007	Intership at University of Basel in the biophysic group of Dr. Martin Hegner
10/2005 - 08/2006	Master thesis in the group of Prof. Dr. Nicolas Gisin at the University of Geneva Subject: "Independent, Picosecond Pulsed Time-Bin Entangled Twin Photon Source at 1550nm"
10/2004 - 11/2006	Master study in Physics at the University of Basel
10/2001 - 10/2004	Bachelor study in Physics at the University of Basel
2002	Corporal army service obligation in Switzerland
2001	Army service obligation in Switzerland
1993-2001	High school in Basel
20/04/1982	Birth in Basel, Switzerland

Appendix A

Fiber preparation and alignment

This appendix describes the preparation and alignment of large mode area fibers for spectral broadening and pulse compression. Although, the experimental setup requires a less intensive maintaining, some procedures like preparing the fiber and alignment have to be done from time to time. This appendix shall help to avoid mistakes.

Suppliers: There is currently only one company, called NKTphotonics (former crystal-fibre), which is able to produce photonic crystal large mode area fibers (LMA). Well known distributors are Thorlabs and Newport. Buying directly from NKTphotonics is possible, but a minimum length of 10m has to be purchased. Thorlabs offers only LMAs with core diameters of 12.5, 20, 25 and 35μm and a delivery time of maximally 3 days. Contrary Newport which has the whole offer except LMA 5 (note: LMA 5 polarization maintaining is offered) but with a delivery time of 2-3 weeks. The price for all core diameters is $\sim$100 euros per meter.

Removing the jacket: Jacket should be removed as scattered light can generate new undesired frequencies. Furthermore, at high average power the jacket evaporates probably due the scattered light from the core. Three different techniques exist, removing by aceton, by mechanical stripping, or by hot air, for example from a hair-dryer. For larger core diameters ($>15\mu$m) we used the stripping tool, smaller ones with aceton. With aceton it is more difficult to remove the full jacket length from pieces longer than around 7cm. The long fiber has to be submerged totally by aceton. For small pieces, putting the fiber in a small bottle of aceton and waiting around 2 minutes is enough. Note, aceton will get sucked into the holes and later covering the fiber surfaces which reduces the transmission for $\sim$2% as well as damaging the fiber earlier. If possible one should use mechanical stripping or by hot air (hair-dryer).

Cleaving the fiber: The fiber is scratched by a mechanical moved diamond blade from a commercial cleaver (Photon Kinetics, Inc., Model FK12)for single mode fiber with a 9μm fiber core diameter. However, every core diameter fits to the cleaver. No cleaving angle is set (induces too much stress onto the fiber). A "scream" during the diamond blade cuts the fiber indicates a good cleave. After, with tweezers the fiber is taken out of the cleaver and rotated by $90°$ so that the scratched zone shows up. Hold now the fiber with two fingers on the part you will use later and push with two fingers from above to down the other part of the fiber. The fiber will break, resulting in a nice cleave. No force or fast speed is needed, a smooth movement is sufficient. No experience is needed

to make the move. Note, that as long as the core does not show any kind of damages like, dirt (glass from the cleaving) or slots (which can appear from the holes) the fiber should work well in the experiment. The fiber can be scratched too by hand using a diamond blade or marble plate. Doing so, a certain experience is necessary until a good cleave is achieved.

Experimental setup: Concerning the fiber setup one should consider following aspects:

- The focusing lens is calculated for the mode field diameter of the fiber.
- A lever arm (and two irises) before the focusing lens ensures a correct excitation of the fundamental fiber mode.
- After the collimating lens, a lever arm and two irises before the chirped mirrors should be set, to guarantee a correct angle of incidence for the chirped mirrors. Note, every new fiber piece yields a slightly different output beam direction. This can be corrected with the lever arm and the irises.
- Focusing and collimating lenses should be aspheric and antireflected ones, and be placed on translation stages.
- The fiber holder should be mounted onto a 3-axis translation stage (e.g. NanoMax MAX312/M, Thorlabs) for coupling into the fiber.

Of course, other setups are possible as well. Like having a fixed fiber position but moving the collimating lens for coupling. However, we recommend our setup as it is cheaper and more compact. No, clear advantage or disadvantage of the two setups have been noted.

Alignment of the fiber: A correct pre-alignment of the setup saves you 99% of the time of the fiber alignment. With some experience the alignment of a new fiber piece is done within a minute.

Pre-alignment of the setup (has to be done only once): Essential for the mode excitation is that the wavefront comes perpendicular to the fiber surface. Hence, care has to be paid when fixing the height of the beamline. Alignment is done as usual. One fixes the beamline (first lever arm already set) and starts putting the elements from inside to outside. Means first set the fiber holder, then the focusing lens, the collimating lens and then the two irises before the focusing lens. The second lever arm and irises will be set as last. Mark the fiber holder translation stage position as well as the one of the lenses (best middle position of each translation axis) so that you can always return to this position if necessary.

Fiber alignment: Pre-exciting the mode requires that the focus is within 1mm set to the fiber surface. This accuracy can be easily measured by a ruler. Or by watching the beamprofil scattered on the fiber holder. If the beam focus is near the input surface, all light hits the fiber input surface and will be not scattered by the fiber holder. Put now a white piece of paper behind the collimating lens and watch the "beamprofil". In parallel, record the spectrum by the spectrometer. Normally, one should see now only "speckles" in the beamprofil and no broadening of the spectrum. If you have already some spectral broadening, then optimize on it. If not, then move the fiber in the middle of the focus. You can do that easily

by counting the way you moved with the translation screws from one side of the fiber to the other one (width and height). The beamprofil changes dramatically as soon you are out of the fiber. Now move your fiber into the middle of the focus. Watch the beamprofil and spectrum. If you still see no broadening or mode (on the paper), then move slightly the focusing lens until you see a mode. For small core fibers (<LMA 8), before you reach the middle, your beam will vanish totally on the screen. It is a good indication that you are near to the mode coupling. As soon as you have a pre-excitation of the mode you can optimize it, first with the help of the spectral broadening. Move the focusing lens and the fiber translation screws to achieve maximal spectral broadening. Repeat this several times. Now, the mode looks already quite good but has still some "speckles" around it. Make a walk-off with the first leverarm until you see no speckles anymore. The spectrum should be a bit broader again. Use again the translation screws to be sure you have maximum broadening.

01 Fiber mode: Even the LMAs are so called endlessly single mode, the 25μm core LMA shows sometimes some 01 fiber mode behavior. Actually, in many cases you will first have a 01 mode, especially when working with a laser system at 1030nm. Note that you have to look exactly to recognize it. Single mode operation is achieved during the fine adjustment with the leverarm. Note that the spectral broadening of the 01 mode will be not significantly different compared to the fundamental mode.

Transmission: the transmission of around 87% for a 800nm beam indicates a good coupling into the fiber (nice mode assumed). Having smaller transmission mostly corresponds with some "speckles" in the beamprofil and comes from either not yet a good coupling (check focusing length), or from a bad cleave e.g. (very) dirty fiber surface. In most of the cases it is the coupling. For a 1030 laser system the transmission is ∼70% (see section 4.3).

Contrary to the widespread opinion of a difficult fiber handling, the preparation and alignment of a LMA fiber is trivial and does not require any special skill nor effort. A fiber change, including cleaving and alignment, can be done without problems in less than 15 minutes.

Appendix B

Reprint publications

16 fs, 350 nJ pulses at 5 MHz repetition rate delivered by chirped pulse compression in fibers

T. Ganz, V. Pervak, A. Apolonski, and P. Baum*

*Max-Planck-Institute of Quantum Optics and Ludwig-Maximilians-Universität München,
Am Coulombwall 1, 85748 Garching, Germany*
Corresponding author: peter.baum@lmu.de

We demonstrate a simple approach for broadening and compression of intense pulses at megahertz repetition rates by self-phase modulation in nonlinear photonic crystal fibers. In order to avoid damage by self-focusing, we positively chirp the input pulses, which allows coupling of significantly more energy into the fiber, while maintaining the same spectral bandwidth and compression as compared to the Fourier-limited case at lower energy. Using a commercial long-cavity Ti:sapphire oscillator with 55 fs, 400 nJ pulses at 5 MHz, we generate 16 fs, 350 nJ pulses, which is a factor of 4 more energy than possible with unchirped input pulses. Self-phase-modulated spectra supporting 11 fs duration are also shown with 350 nJ pulse energy. Excellent stability is recorded over at least 1 h.   © 2011 Optical Society of America

OCIS codes: 140.7090, 190.4370, 320.1590, 320.5520.

At megahertz repetition rates, the generation of sub-15-fs laser pulses with hundreds of nanojoules of single-pulse energy represents a challenging task, but a variety of applications, such as ultrafast spectroscopy, diffraction with single electrons [1], high-harmonic generation [2], resonant plasmonic field enhancement [3], and material processing [4,5], would profit from the increased signal-to-noise ratio, total flux, or reduced measurement and processing time. One approach for generating short and intense pulses at megahertz repetition rates is the use of noncollinear optical parametric amplifiers (NOPAs); the typical achievements at 800 nm are 400 nJ, 15 fs at 1–2 MHz [6–8]. Noncollinear optical parametric amplifiers offer some advantages, such as spectral tunability, but also suffer from a certain complexity as a result of the several nonlinear conversions to be combined. Alternatively, intense pulses at megahertz repetition rates can also be produced by long-cavity oscillators [9], fiber amplifiers [10,11], or Innoslab amplifiers [12], but the pulse duration is so far only ~40 fs to 1 ps in these systems.

Directly reaching shorter durations seems currently not feasible, and an external pulse compression stage is therefore required. An efficient way is to couple the laser beam into a solid single-mode fiber for spectral broadening by self-phase modulation [13] and subsequent chirp compensation [14–18]. However, a central limitation is the damage caused by self-focusing in the front part of the fiber. This limits the maximum amount of single-pulse energy that can be coupled into the fiber.

Self-focusing is mainly caused by peak power but not by intensity. This should allow prevention of damage by using the well-known concept of chirping [19]. Making use of the longer duration of chirped pulses, the peak power decreases, and we can couple more energy into the fiber before self-focusing starts (see Fig. 1). Our approach is based on fibers with normal dispersion, in order to avoid solitonic and Raman processes that can make the output incompressible. This regime requires positive chirp, because negative chirp will result in spectral narrowing [20], or broadening only after an intermediate temporal focus somewhere in the middle of the fiber [21]. The question that remains is whether we can achieve the same extent of spectral broadening and compression as compared to conventional, unchirped input pulses. In the following we demonstrate that this is indeed the case and show that compressed output pulses of significantly higher energy can be generated as without chirping.

Our femtosecond laser source at 5 MHz repetition rate is a commercial chirped pulse Ti:Sa oscillator (Scientific XL, Femtolasers GmbH) with an output of 500 nJ and 55 fs at 800 nm central wavelength. The high intracavity energy requires operation of the oscillator in the positive dispersion regime [9]; hence, the pulses are positively chirped at the output coupler. An extracavity prism compressor is therefore included in the commercial laser system. Translation of the prisms enables us to positively or negatively chirp the system's output pulses.

For the studies reported here, we used a tunable attenuation stage, consisting of an achromatic half-wave plate and a polarizer. A Faraday isolator is used to protect the laser's mode locking from backreflections from the fiber surface. By rotating the half-wave plate, an adjustable energy range of 0–400 nJ is thus provided without changing the chirp. For spectral broadening we selected a commercial large-mode-area photonic crystal fiber from NKTPhotonics (LMA-25, Thorlabs) with a mode field diameter of 20 μm and a zero-dispersion wavelength of ~1300 nm. The LMA-25 fiber lies freely in a self-made V-groove holder that is placed onto a three-axis translation stage. A fiber length of 30 mm was used [14,15]. For our beam diameter of about 3 mm, we selected antireflection-coated aspherical lenses with $f \approx$ 50 mm for focusing (L1) and with $f \approx 20$ mm for collimation (L2). Compression is achieved by using double-angle chirped mirrors [22], which were designed
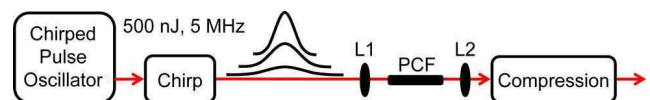

Fig. 1.   (Color online) Concept of chirped pulse compression. A megahertz laser's output pulses are stretched before entering a nonlinear fiber (PCF). This avoids self-focusing and provides significantly improved output energies.

for a bandwidth from 680 nm to 890 nm and for $-100\,\text{fs}^2$ per reflection, without compensation of higher-order dispersion. We used 24 reflections in combination with several millimeters of quartz blocks and wedges for fine tuning, resulting in a total transmission of >90%. Note that the output energy values given below are measured after the collimating lens and are to be reduced by 10% for the compressed pulses. The compressed pulses are characterized by interferometric autocorrelation (Femtometer, Femtolasers GmbH). The total setup of spectral broadening and compression covers a space of only 35 cm × 65 cm.

First, we investigated the broadening of Fourier-limited pulses (55 fs). The upper row of Fig. 2 shows the results. We adjusted the input pulse energy close to the damage threshold, resulting in an energy of ~90 nJ. Figure 2(a) shows the input spectrum (dotted) and the broadened spectrum (solid); note the linear scale. The transmission efficiency was 87% (~78 nJ after the collimating lens). The spectrum's Fourier limit was 12.0 fs, and the autocorrelation [Fig. 2(b)] indicated a pulse duration of 14.5 fs.

The lower row of Fig. 2 shows the results for a stretched input pulse. With the laser system's prism sequence, we positively chirped the pulses to a duration of ~215 fs (FWHM of the intensity). This made it possible to couple in and broaden the full available pulse energy of ~402 nJ without damage. Output pulses with ~352 nJ (average power 1.76 W) were achieved, which corresponds to a transmission of 88%, similar to the unchirped case. This represents a factor of 4 more energy as when using Fourier-limited input pulses. The spectrum [Fig. 2(c)] had a Fourier limit of 14.5 fs, and the measured pulse duration was 16 fs [Fig. 2(d)].

In both cases, chirped and Fourier-limited, the dominant process for spectral broadening is self-phase modulation influenced by group velocity dispersion [14], which is evident from the typical spectral shapes. The two autocorrelations show side maxima that are an inevitable result of the spectral shape. The positions and shapes of all side maxima in the range of ±150 fs are in very good agreement with calculated Fourier-limited autocorrelations of the respective spectra. We attribute
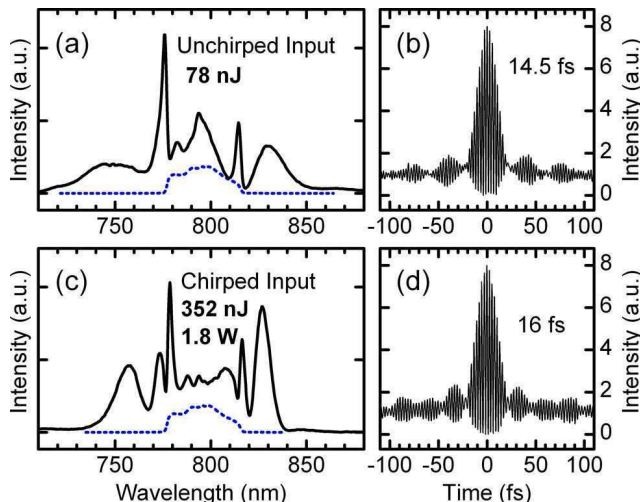

Fig. 2. (Color online) Comparison of (a), (b) unchirped and (c), (d) chirped broadening and compression.
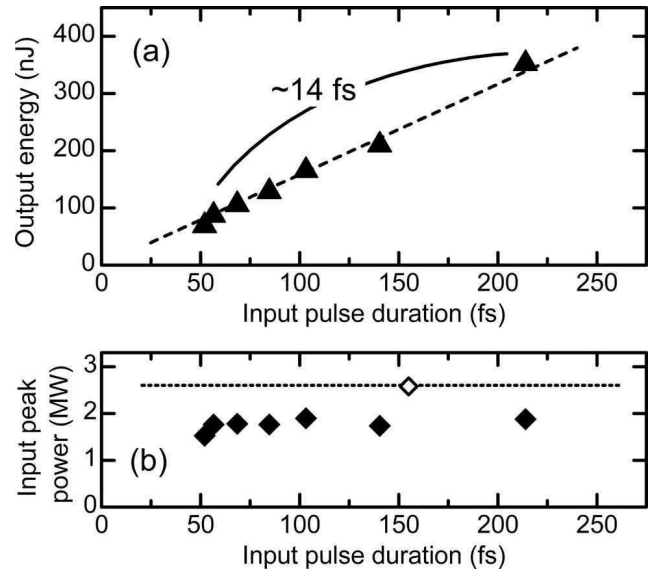

Fig. 3. Relation of input peak power to output energy at constant spectral broadening (see text). The open diamond shows the parameters for the 11 fs spectrum of Fig. 5.

the residual small deviations to the missing third-order-dispersion correction of the fiber material. However, not much more higher-order chirp seems to be induced by the chirped case as compared to the Fourier-limited case. The similarity of the two spectra and autocorrelations shows that chirped input pulses provide a comparable broadening and compression, but at higher energies. If, at a given chirp, the input pulse energy is successively increased, the full spectral width of the unchirped case can be recovered before the fiber gets damaged.

Figure 3(a) shows the achieved output energy (triangles) using different input pulse durations when the spectral width of the Fourier-limited case is maintained. For unchirped pulses, the input peak power was set to around 75% of the self-focusing threshold, which resulted in a spectrum extending from about 730 to 860 nm (Fourier limit ~14 fs). For each input chirp value, we increased the input power until a similar spectral broadening was reached. At constant broadening (Fourier limit of ~14 fs), the achievable output energy (triangles) increased directly with the input pulse duration. In Fig. 3(b), we plotted the resulting input peak power (solid diamonds), which stayed always in the same, safe range below the self-focusing threshold, computed for fused silica at 800 nm (dotted line) [23]. These two observations
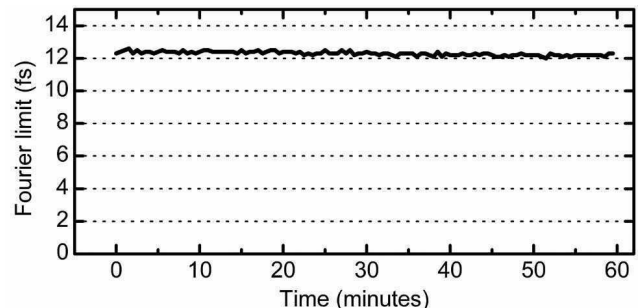

Fig. 4. Long-term stability of the spectral shape in our chirped pulse compression approach.
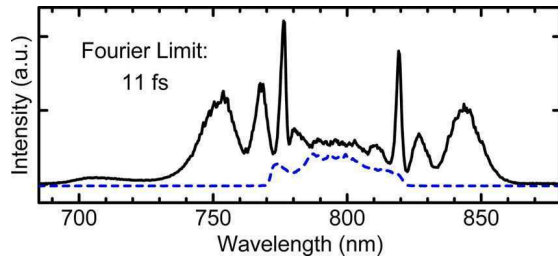
Fig. 5. (Color online) Approaching the 10 fs regime at full energy (5 MHz, input 400 nJ, output 354 nJ).

indicate that even higher output energies, in the microjoule regime, should be feasible with more input energy in combination with a stronger input chirp.

We demonstrate an excellent stability of our approach by recording the Fourier limit of a broadened spectrum (input ~286 nJ, transmission 88%) every 30 s (see Fig. 4). The spectral shape and Fourier limit, as well as the output energy, do not fluctuate or drift, although the fiber was lying freely in the holder. No kind of cover or fiber stabilization was necessary. The pulse-to-pulse energy fluctuations of the output were ~1% (RMS). In none of our experiments was ablation or other type of direct damage to the input surface observed. We could use the same piece of fiber over many weeks. Also, the azimuthal orientation of the fiber's photonic structure was investigated and found to be insignificant for the output.

In an additional measurement, we adjusted the chirp quite close to the self-focusing threshold [see open diamond in Fig. 3(b)], in order to see what spectral broadening can be achieved with the full available power of our laser system. With an input of ~400 nJ, a chirped duration of ~155 fs, and an LMA-25 fiber of 29 mm length, the broadened output spectrum supported pulses of 11 fs duration (see Fig. 5). The output energy was ~354 nJ, the transmission 88.5%, and the average power ~1.77 W. The peak power is ~30 MW. This spectrum was, like before, stable for at least 1 h. We expect that the sub-10-fs regime can be reached at our oscillator's full energy by using a fiber with a somewhat smaller mode field diameter. The higher intensity should lead to an increased broadening at constant peak power.

The concept of chirped pulse compression is general and should also be applicable to other broadening schemes based on self-phase modulation. For example, we expect direct advantages when compressing high-energy pulses from kilohertz lasers in gas-filled hollow-core fibers. At megahertz repetition rates, chirped pulse compression is an attractive alternative to megahertz NOPAs for generating extremely short pulses in the microjoule, 10 fs regime. Because of its simplicity, the combination of a commercial chirped pulse oscillator with our simple chirped pulse compression scheme will be a convenient source of shortest pulses for applications.

References

1. M. Aidelsburger, F. O. Kirchner, F. Krausz, and P. Baum, Proc. Natl. Acad. Sci. USA **107**, 19714 (2010).
2. T. Brabec and F. Krausz, Rev. Mod. Phys. **72**, 545 (2000).
3. S. Kim, J. Jin, Y.-J. Kim, I.-Y. Park, Y. Kim, and S.-W. Kim, Nature **453**, 757 (2008).
4. C. B. Schaffer, A. Brodeur, J. F. García, and E. Mazur, Opt. Lett. **26**, 93 (2001).
5. R. Osellame, N. Chiodo, V. Maselli, A. Yin, M. Zavelani-Rossi, G. Cerullo, P. Laporta, L. Aiello, S. D. Nicola, P. Ferraro, A. Finizio, and G. Pierattini, Opt. Express **13**, 612 (2005).
6. M. Emons, A. Steinmann, T. Binhammer, G. Palmer, M. Schultze, and U. Morgner, Opt. Express **18**, 1191 (2010).
7. C. Schriever, S. Lochbrunner, P. Krok, and E. Riedle, Opt. Lett. **33**, 192 (2008).
8. J. Rothhardt, S. Hädrich, D. N. Schimpf, J. Limpert, and A. Tünnermann, Opt. Express **15**, 16729 (2007).
9. S. Naumov, A. Fernandez, R. Graf, P. Dombi, F. Krausz, and A. Apolonski, New J. Phys. **7**, 216 (2005).
10. F. Röser, J. Rothhard, B. Ortac, A. Liem, O. Schmidt, T. Schreiber, J. Limpert, and A. Tünnermann, Opt. Lett. **30**, 2754 (2005).
11. F. Röser, D. Schimpf, O. Schmidt, B. Ortaç, K. Rademaker, J. Limpert, and A. Tünnermann, Opt. Lett. **32**, 2230 (2007).
12. P. Russbueldt, T. Mans, J. Weitenberg, H. D. Hoffmann, and R. Poprawe, Opt. Lett. **35**, 4169 (2010).
13. G. P. Agrawal, *Nonlinear Fiber Optics* (Academic, 2001).
14. D. Grischkowsky and A. C. Balant, Appl. Phys. Lett. **41**, 1 (1982).
15. W. J. Tomlinson, R. H. Stolen, and C. V. Shank, J. Opt. Soc. Am. B **1**, 139 (1984).
16. T. Südmeyer, F. Brunner, E. Innerhofer, R. Paschotta, K. Furusawa, J. C. Baggett, T. M. Monro, D. J. Richardson, and U. Keller, Opt. Lett. **28**, 1951 (2003).
17. T. Eidam, F. Röser, O. Schmidt, J. Limpert, and A. Tünnermann, Appl. Phys. B **92**, 9 (2008).
18. B. Metzger, A. Steinmann, F. Hoos, S. Pricking, and H. Giessen, Opt. Lett. **35**, 3961 (2010).
19. D. Strickland and G. Mourou, Opt. Commun. **56**, 219 (1985).
20. M. Oberthaler and R. A. Höpfel, Appl. Phys. Lett. **63**, 1017 (1993).
21. P. Dombi, P. Antal, J. Fekete, R. Szipőcs, and Z. Várallyay, Appl. Phys. B **88**, 379 (2007).
22. V. Pervak, I. Ahmad, M. K. Trubetskov, A. V. Tikhonravov, and F. Krausz, Opt. Express **17**, 7943 (2009).
23. D. Milam, Appl. Opt. **37**, 546 (1998).

Mid-infrared near-field spectroscopy

Sergiu Amarie*, Thomas Ganz, and Fritz Keilmann

Max Planck Institute for Quantum Optics, 85741 Garching, Germany
*samarie@rzg.mpg.de

Abstract: We demonstrate *continuous* infrared spectra from 20 nm sample spots, by combining dispersive Fourier-transform infrared spectroscopy (FTIR) with scattering near-field microscopy (s-SNOM). With the "apertureless" tip of a standard AFM cantilever in one arm of a Michelson interferometer the spectra arise simultaneously in amplitude and phase. The effect of near-field phonon resonance of SiC is used to verify background-free s-SNOM operation, and to determine the absolute scattering efficiency, at 6 cm^{-1} spectral resolution. We further report first evidence of free-induction decay from a scatterer composed of parts coupled by near-fields. This is possible only with broadband illumination. It offers a new, unique tool to discriminate against background scattering artifacts.

©2009 Optical Society of America

OCIS codes: (160.2710) Inhomogeneous optical media; (180.4243) Near-field microscopy; (300.6340) Spectroscopy, infrared; (300.6300) Spectroscopy, Fourier transforms.

References and links

1. F. Keilmann, and R. Hillenbrand, "Near-field nanoscopy by elastic light scattering from a tip," in *Nano-Optics and Near-Field Optical Microscopy*, A. Zayats and D. Richards, eds. (Artech House, 2009).
2. M. M. Qazilbash, M. Brehm, B. G. Chae, P. C. Ho, G. O. Andreev, B. J. Kim, S. J. Yun, A. V. Balatsky, M. B. Maple, F. Keilmann, H. T. Kim, and D. N. Basov, "Mott transition in VO$_2$ revealed by infrared spectroscopy and nano-imaging," Science **318**(5857), 1750–1753 (2007).
3. A. J. Huber, D. Kazantsev, F. Keilmann, J. Wittborn, and R. Hillenbrand, "Simultaneous infrared material recognition and conductivity mapping by nanoscale near-field microscopy," Adv. Mater. **19**(17), 2209–2212 (2007).
4. R. Hillenbrand, T. Taubner, and F. Keilmann, "Phonon-enhanced light matter interaction at the nanometre scale," Nature **418**(6894), 159–162 (2002).
5. T. Taubner, R. Hillenbrand, and F. Keilmann, "Nanoscale polymer recognition by spectral signature in scattering infrared near-field microscopy," Appl. Phys. Lett. **85**(21), 5064–5066 (2004).
6. M. Brehm, T. Taubner, R. Hillenbrand, and F. Keilmann, "Infrared spectroscopic mapping of single nanoparticles and viruses at nanoscale resolution," Nano Lett. **6**(7), 1307–1310 (2006).
7. I. Kopf, J. S. Samson, G. Wollny, C. Grunwald, E. Bründermann, and M. Havenith, "Chemical imaging of microstructured self-assembled monolayers with nanometer resolution," J. Phys. Chem. C **111**(23), 8166–8171 (2007).
8. K. Mueller, X. Yang, M. Paulite, Z. Fakhraai, N. Gunari, and G. C. Walker, "Chemical imaging of the surface of self-assembled polystyrene-b-poly(methyl methacrylate) diblock copolymer films using apertureless near-field IR microscopy," Langmuir **24**(13), 6946–6951 (2008).
9. M. Brehm, A. Schliesser, and F. Keilmann, "Spectroscopic near-field microscopy using frequency combs in the mid-infrared," Opt. Express **14**(23), 11222–11233 (2006).
10. N. Ocelic, A. Huber, and R. Hillenbrand, "Pseudo-heterodyne detection for background-free near-field spectroscopy," App. Phys. Lett. **89**, 101124–101121 - 101124–101123 (2006).
11. B. Knoll, and F. Keilmann, "Enhanced dielectric contrast in scattering-type scanning near-field optical microscopy," Opt. Commun. **182**(4-6), 321–328 (2000).
12. H. G. von Ribbeck, M. Brehm, D. W. van der Weide, S. Winnerl, O. Drachenko, M. Helm, and F. Keilmann, "Spectroscopic THz near-field microscope," Opt. Express **16**(5), 3430–3438 (2008).
13. M. Brehm, A. Schliesser, F. Cajko, I. Tsukerman, and F. Keilmann, "Antenna-mediated back-scattering efficiency in infrared near-field microscopy," Opt. Express **16**(15), 11203–11215 (2008).
14. T. Taubner, F. Keilmann, and R. Hillenbrand, "Nanomechanical resonance tuning and phase effects in optical near-field interaction," Nano Lett. **4**(9), 1669–1672 (2004).
15. A. Huber, N. Ocelic, T. Taubner, and R. Hillenbrand, "Nanoscale resolved infrared probing of crystal structure and of plasmon-phonon coupling," Nano Lett. **6**(4), 774–778 (2006).
16. A. J. Huber, A. Ziegler, T. Köck, and R. Hillenbrand, "Infrared nanoscopy of strained semiconductors," Nat. Nanotechnol. **4**(3), 153–157 (2009).
17. A. Cvitkovic, N. Ocelic, and R. Hillenbrand, "Analytical model for quantitative prediction of material contrasts in scattering-type near-field optical microscopy," Opt. Express **15**(14), 8550–8565 (2007).

18. F. Keilmann, "Surface-polariton propagation for scanning near-field optical microscopy application," J. Microsc. **194**(2-3), 567–570 (1999).
19. M. Stockman, "Nanofocusing of optical energy in tapered plasmonic waveguides," Phys. Rev. Lett. **93**, 137404 (2004).
20. P. G. Gucciardi, G. Bachelier, M. Allegrini, J. Ahn, M. Hong, S. H. Chang, W. Ihe, S. C. Hong, and S. H. Baek, "Artifacts identification in apertureless near-field optical microscopy," J. Appl. Phys. **101**, 64303–64308 (2007).
21. N. Ocelic, "Quantitative near-field phonon-polariton spectroscopy," *Thesis Technische Universität München,* ISBN 9783932749896 (2007).
22. R. Hillenbrand, and F. Keilmann, "Optical oscillation modes of plasmon particles observed in direct space by phase-contrast near-field microscopy," Appl. Phys. B **73**, 239–243 (2001).
23. R. Hillenbrand, F. Keilmann, P. Hanarp, D. S. Sutherland, and J. Aizpurua, "Coherent imaging of nanoscale plasmon patterns with a carbon nanotube optical probe," Appl. Phys. Lett. **83**(2), 368–370 (2003).
24. M. Schnell, A. Garcia-Etxarri, A. J. Huber, K. Crozier, J. Aizpurua, and R. Hillenbrand, "Controlling the near-field oscillations of loaded plasmonic nanoantennas," Nat. Photonics **3**(5), 287–291 (2009).
25. A. Huber, N. Ocelic, D. Kazentsev, and R. Hillenbrand, "Near-field imaging of mid-infrared surface phonon polariton propagation," Appl. Phys. Lett. **87**, 81103 (2005).

1. Introduction

Near-field microscopy by Rayleigh scattering from a tip has the proven potential of tip-limited resolution of typically 20 nm. This is independent of the wavelength which can be chosen throughout the visible, infrared, THz and even microwave regions [1]. Disturbing "background" scattering from parts outside the tip's apex region are routinely suppressed by tapping the tip against the sample and demodulating the light signal at the tapping frequency or its harmonics. Numerous applications have been established using *monochromatic* s-SNOM, for example, the detection of nanosize metallic regions that occur in the insulator-metal phase transition [2], or the quantitative mapping of free-carrier concentration in semiconductor nanodevices [3]. Yet the future impact of s-SNOM requires a *spectroscopic* operation exploiting the infrared and far-infrared vibrational fingerprints. These are routinely assessed in research and industry, using FTIR spectrometers for identification and quantifying chemical composition. Monochromatic s-SNOM has already succeeded in mapping vibrational resonances by repeated s-SNOM imaging at varied frequency, and subsequent extraction of spectra [4–8]. This procedure is, however, rather laborious and prone to errors from non-reproducibilities of the scan process. For example, the sample might drift, the tapping conditions might change, and the tip might erode or pick up debris.

2. Design of broadband s-SNOM

Our present experiment uses spectrally broadband illumination of a novel, commercial s-SNOM (NeaSNOM, neaspec.com), for recording a spectrum at each pixel while scanning (Fig. 1).
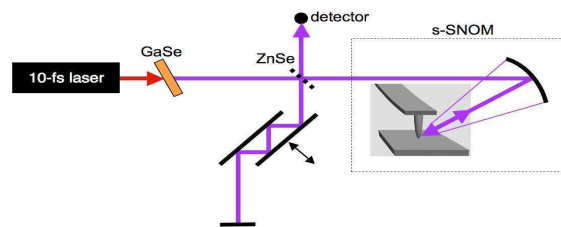
Fig. 1. Sketch of spectroscopic near-field microscope where the back-scattering probe tip represents one end mirror of a dispersive Michelson interferometer. A mirror in the reference arm is mechanically translated to record an interferogram which is then Fourier-transformed to determine both amplitude and phase spectra.

Interferometric operation is achieved by a dispersive Michelson configuration, resembling the earlier homodyne [5], multi-heterodyne [9], and pseudo-heterodyne setups [10]. The reference arm's length is continuously varied and an interferogram is recorded for subsequent Fourier-transformation (FT). We use a coherent beam with a broad spectrum resulting from difference-frequency generation in a 200 µm thick GaSe crystal (ATOM, eletot.tsu.ru), of 10-

fs Ti:S laser pulses at 125 MHz repetition and 500 mW quasi-c.w. power. The crystal is oriented to generate the band between 9 and 12 µm at 5 µW quasi-c.w. power. The back-scattered infrared beam is partially reflected at the beam splitter, a 2 mm thick uncoated ZnSe plate, and focused on a HgCdTe detector (KLD-0.25-J1, kolmar.com). The signal is amplified by 60 db (HVA-10M-60-B, femto.de) and processed in a lock-in amplifier (EG&G5302, princetonappliedresearch.com). The s-SNOM's focusing mirror has about 20 mm effective focal length and accepts a collimated beam in a 15 mm aperture. The incident beam is at about 30° inclination to the horizontal sample surface and is vertically polarized. The sample is scanned while the commercial cantilevered Pt-coated tip (PPP-NCHPt-20, nanosensors.com) is fixed and oscillates at 310 kHz. An integrated microscope provides a top view of the sample, the cantilever, the AFM laser spot, and the illuminating spot which helps in the alignment of both the AFM and s-SNOM operations.

The recording of interferograms is done with an oscilloscope (Wavesurfer 422, lecroy.com). This also performs on-line FT for previewing spectra at 20 cm^{-1} resolution, as limited by nonlinearity in the mirror translation stage (P-628, pi.ws). We overcome this constraint by off-line resampling according to frequent calibration interferograms taken with a CO_2 laser beam, set at about 100 µW by a step attenuator (102, lasnix.com). With our choice of 1.7 mm long interferograms taken in 2 s the resolution becomes 6 cm^{-1}. The interferometer arm length of about 25 cm is found sufficiently short to keep, in the thermostatted laboratory, thermal drifts small enough that the phase calibration stays valid over hours.

2. SiC near-field phonon resonance

In view of the rather low power from our broadband source the s-SNOM is initially aligned with the CO_2 laser beam. The reference mirror position for positive interference of all frequencies (white light position, WLP) is approximately set with the help of a ruler (the optical path length inside the NeaSNOM is 2 x 17 cm). The power efficiency of backscattering from the tip is found to be of the order of 0.25%, which corresponds to a detector signal level of about 5% of the input signal (Fig. 2). The latter is experimentally determined by an auxiliary probe arm with a full mirror.
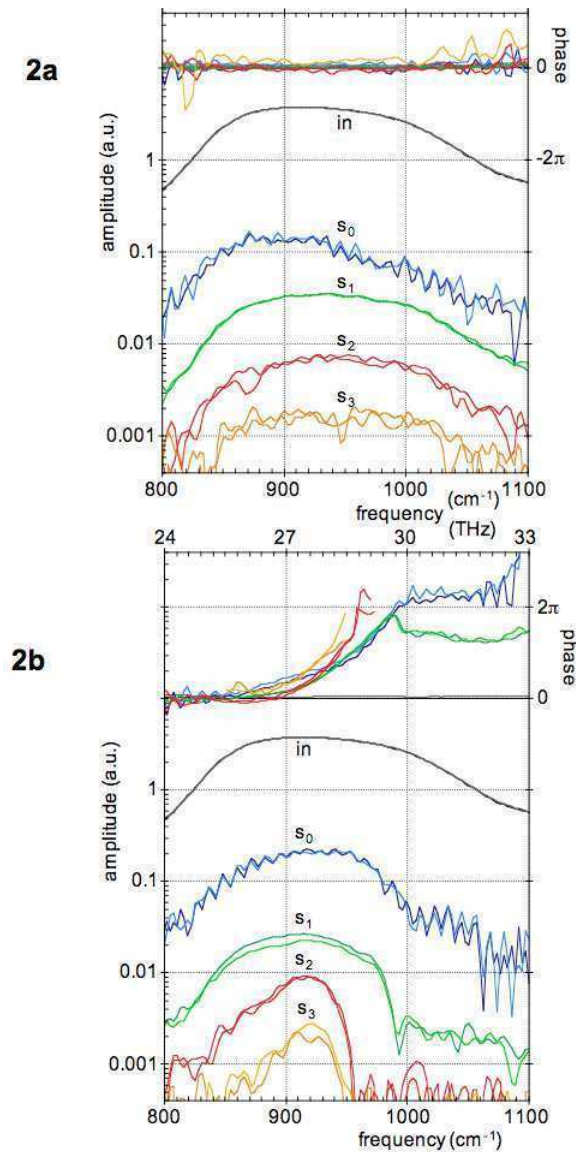
Fig. 2. Mid-infrared spectra obtained by s-SNOM of an Au sample (a) and a SiC sample (b). Amplitude spectra (lower part) are shown for the input beam (in), the directly backscattered beam (s_0), and its demodulated components at the nth harmonics (s_n). The corresponding phase spectra (upper part) are shown in the same colours. The WLP was chosen such that the phase is nearly constant for the $n = 1$ phase spectrum of Au. The tapping amplitude was set to 100 nm.

Similar as in earlier reports [9,11,12], the modulated amplitudes of backscattering are found to decrease with n, here roughly by a factor 5 per harmonic order. With the non-resonant Au sample the spectral shapes are similar to that of the input spectrum, except for the direct scattered one, s_0; its distortion resembles that found earlier with a different tip shape, and may indicate antenna resonance [13]. The phase spectra are flat and unshifted within 20° which means the locus of backscattering remains within ± 140 nm constant for all spectral elements. Approach curves (not shown) are regularly taken, with the interferometer kept fixed, to ascertain that the n = 2, 3 responses are dominated by near-field interaction.

Figure 2b displays the spectra obtained with a SiC sample which possesses a well-studied near-field phonon resonance in the mid infrared [4,9,13–17]. As expected for this resonance,

the amplitude spectra for n = 2, 3 exhibit a ca. 60 cm^{-1} wide peak (FWHM) at ca. 920 cm^{-1} exceeding the value of Au. The n = 0, 1 spectra, in contrast, appear flat up to about 980 cm^{-1} where the amplitude markedly decreases. This is expected for the far-field response due to Fresnel reflection in the Reststrahlen region of SiC, as illustrated in Fig. 2 of ref [4]. The phase spectra exhibit a monotonic increase in the Reststrahlen region. This increase is enhanced in the near-field interaction. Our general conclusion is that spectroscopic s-SNOM generates meaningful amplitude and phase spectra. Specifically, the near-field interaction dominates the spectra from demodulation order n = 2 up, given the tip geometry and tapping paramters as used here.

3. Background-free detection at first harmonic

The results (Fig. 3) of a second measurement series with a different tip from the same batch indicate, in the n = 1 spectrum, the presence of substantial background scattering; this could come from a non-perfect alignment of the focus to the tip or may reflect an antenna property of the tip. We present this series because it illustrates a new way to recognize background contamination, by inspecting pulse-type interferograms obtainable only with broadband illumination. In Fig. 3b the centrally plotted interferogram of the input (black, scaled /100) lasts for a time span A. It can be understood as the autocorrelation of a ca. 3-cycle input pulse. Nearly congruent with it are interferograms of the two samples measured at 3 µm retraction from contact (dotted red and green). Since such a retraction must fully suppress the near-field interaction [1,11], the dotted spectra (Fig. 3a) designate pure background scattering. We assume such background spectra should prevail nearly unaltered also at contact. This is confirmed by comparison with the n = 1 interferogram of Au. It starts out congruently in shape with the input, but then continues ringing for a time span B. The difference of both interferograms, on and off contact, is approximately identical in shape with that of the n = 2 interferogram. The latter represents the pure near-field response, as concluded above from approach curves, and as also can be seen by comparing the n = 2 spectrum of Fig. 3a with Fig. 2b and previous reports [9,16].
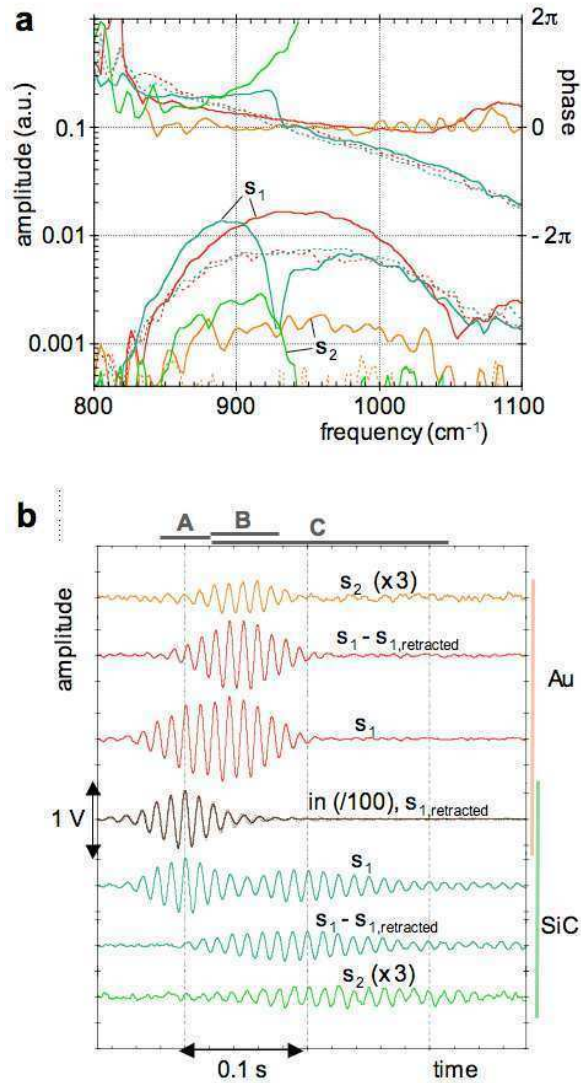
Fig. 3. Mid-infrared s-SNOM spectra (a) and corresponding interferograms (b) obtained with an Au (red, yellow) and a SiC sample (green, blue). Background scattering is present in the $n = 1$ but not in the $n = 2$ cases. The interferograms (offset for clarity) exhibit three distinguishable features, (A) background scattering signature congruent with input, (B) near-field response of Au, (C) near-field response of SiC. The tapping amplitude was set to 65 nm.

We thus suggest that the near-field response can be approximately determined even from background-contaminated $n = 1$ interferograms, during time span B, owing to the fact that the background and the near-field features appear essentially time-separated. Since the signal level for $n = 1$ is about 5x larger than for $n = 2$, the choice of using $n = 1$ interferograms instead of $n = 2$ interferograms has a decisive advantage for performing the initial s-SNOM setup because it requires a 25x shorter measuring time for the same S/N ratio. Note that, in contrast, the *spectral* curves (red, full and dotted, in Fig. 3a) would give no hint of the presence of a background. Our observation is corroborated by the interferograms taken with the SiC sample (Fig. 3b). In these, the ringing lasts for a prolonged time span C. Furthermore, it starts with a substantial phase shift compared to the background feature, which leads to a minimum in the s_1 envelope. Both features are related to the phonon resonance of SiC. The

relatively long ringing marks the high quality factor owing to substantial energy stored in the cavity formed by the tip apex and the sample.

4. Free-induction decay

A prolonged response (ringing) is well known as free-induction decay (FID) in many other fields of coherent spectroscopy mainly of quantum systems such as spin or vibrational/electronic two-level systems. What we observe here is the first evidence of FID in a classical near-field coupled system, namely a scatterer close to a material surface. While implications and analogies with quantum systems are beyond the scope of this letter, we emphasize the FID's interesting practical application for s-SNOM adjustment and operation as already explained. We add another aspect, which may be of high interest in future studies. The interferogram could detect retardation generated by internal delay within a complex scatterer caused, for example, by surface plasmon propagation as considered in refs [18,19]. Intra-scatterer retardation as small as $10°$ could be detected, which at 1 µm wavelength would correspond to a propagation time as short as 83 as.

5. Influence of tapping amplitude

To probe the influence of the tapping amplitude on both background and near-field signals we performed a systematic variation and display the result in Fig. 4.
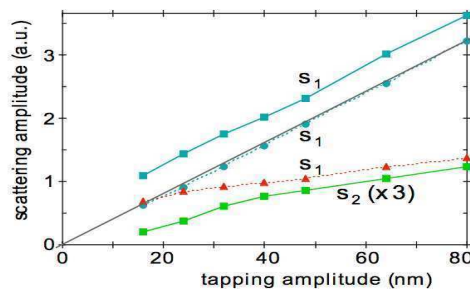

Fig. 4. Experimental, spectrally averaged s-SNOM amplitude of SiC (squares), of SiC retracted 3 µm away from contact (dots), and of the difference (triangles) *vs* tapping amplitude. Connecting curves and the straight line are guides to the eye only.

A linear behaviour is found for the pure background signal (dots at n = 1), as to be expected, whereas the other curves show a saturated behaviour obviously due to the near-field parts. In the n = 1 case, for example, at 20 nm the near-field part obtained by subtracting the off-contact from the on-contact interferograms (triangles) equals that of the background (dots), but at 50 nm tapping amplitude it amounts to only 50%. This trend is in accord with earlier estimations [20,21]. These predict a slowed increase of the near-field amplitude once the tapping amplitude exceeds the size of the near field, which is of the order of the tip radius, typically 20 nm in our study.

6. Proximity effect

As a final illustration of broadband s-SNOM spectra we demonstrate the influence of a nearby scattering object, the edge of an Au film, which is situated towards the focusing mirror. From former studies of plasmon-resonant scatterers [22–24] or edge scatterers [25] we expect to obtain an increased scattering caused by the additional illumination of the tip due to the proximal scatterer. The results show that such an enhancement indeed occurs, amounting to factors between 2 and 4, and that the spectral signatures stay largely unaffected (Fig. 5).
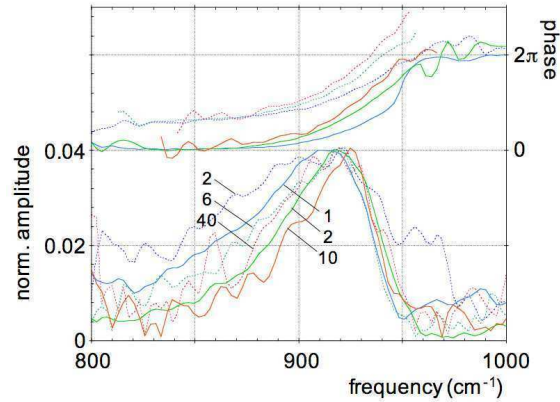
Fig. 5. Mid-infrared spectra obtained by s-SNOM on SiC, 100 µm (full) and 100 nm away (dotted) from a 25 nm high Au film, normalized to the input spectrum. Colour code as in Fig. 2: s_0 blue, s_1 green, s_2 red. The amplitudes are scaled by the factors indicated. The dotted phase spectra are offset for carity. The tapping amplitude was set to 70 nm.

7. Conclusion

The spectra shown in this work were acquired by averaging 10 to 100 interferograms, each lasting 2 s. A boost of the present beam power of 5 µW by at least an order of magnitude would eliminate the need of averaging, and ease the way to spectroscopic near-field images. Altogether, we have shown a robust setup and procedure which uses a broadband light source for illumination and for obtaining local spectra. Our setup requires less installation cost and less computational effort than the former coherent dual frequency-comb system [9]. The present method can readily be used with other types of light sources such as synchrotrons and in other frequency ranges such as, for example, covered by a white light continuum beam.

Acknowledgements

Vector frequency-comb Fourier-transform spectroscopy for characterizing metamaterials

Vector frequency-comb Fourier-transform spectroscopy for characterizing metamaterials

T Ganz[1,3]**, M Brehm**[1]**, H G von Ribbeck**[1,4]**, D W van der Weide**[2] **and F Keilmann**[1,3,5]

[1] Max-Planck-Institut für Biochemie and Center for NanoScience, 82152 Martinsried, Germany
[2] Department of Electrical and Computer Engineering, University of Wisconsin, Madison, WI 53706–1691, USA
[3] Max-Planck-Institut für Quantenoptik and Center for NanoScience, 85741 Garching, Germany
[4] Institut für Angewandte Photophysik, Technische Universität, 01062 Dresden, Germany
E-mail: fritz.keilmann@mpq.mpg.de

Abstract. We determine infrared transmission amplitude and phase spectra of metamaterial samples at well-defined incidence and polarization with a vector ('asymmetric') frequency-comb Fourier-transform spectrometer (c-FTS) that uses no moving elements. The metamaterials are free-standing metallic hole arrays; we study their resonances in the 7–13 μm and 100–1000 μm wavelength regions due both to interaction with bulk waves (Wood anomaly) and with leaky surface plasmon polaritons (near-unity transmittance, coupling features and dispersion). Such complex-valued transmission and reflection spectra could be used to compute a metamaterial's complex dielectric function directly, as well as its magnetic and magneto-optical permeability functions.

[5] Author to whom any correspondence should be addressed.

IOP Institute of Physics Φ DEUTSCHE PHYSIKALISCHE GESELLSCHAFT

Contents

1. Introduction

Metamaterials are artificially structured materials designed for specific electromagnetic properties; they were known as 'artificial dielectrics' in early microwave electronics. Metamaterials with a negative refractive index n, suggested by Mandelshtam (1950) and Veselago (1968), have in the past been experimentally demonstrated for microwaves (Smith *et al* 2000) up to THz frequencies (Yen *et al* 2004). Much activity is presently devoted to their realization for infrared and visible radiation (Dolling *et al* 2006).

A negative n requires both electric permittivity $\varepsilon < 0$ and magnetic permeability $\mu < 0$. The basic design of a negative-index metamaterial is to incorporate subwavelength-sized elements exhibiting either electric or magnetic resonance, and to arrange both types in a regular lattice with a subwavelength-size period. A microscopic optical characterization of such elements is possible by scattering-type scanning near-field microscopy (s-SNOM); this method has already enabled mapping of the electric *near-field* distribution surrounding resonant structures at sub-micrometer resolution (Hillenbrand and Keilmann 2001, Hillenbrand *et al* 2003, Jia *et al* 2008, Valk and Planken 2002, Yu *et al* 2007, Zentgraf *et al* 2008).

The optics application of a metamaterial depends, however, crucially on its *far-field* effects which relate to its spatially averaged optical properties, its electric permittivity and its magnetic permeability. Far-field optical methods can usually determine two observables simultaneously, for example transmittance and reflectance, or amplitude and phase in interferometry, or *psi* and *delta* in ellipsometry. The measurement of these two quantities then enables determination of two optical constants, usually $\varepsilon_1 = \text{Re}(\varepsilon)$ and $\varepsilon_2 = \text{Im}(\varepsilon)$, at each wavelength. Since metamaterials have at least four independent optical constants (the real and the imaginary parts of both ε and μ) their complete characterization requires more measurements, for example, at two different angles of incidence α which, of course, require a well-defined collimated beam. Higher complexity arises with metamaterials containing low-symmetry elements such as split rings which induce bianisotropy, requiring more measurements for the determination of their additional, magneto-optical permittivity properties (Padilla *et al* 2006).

In the near-infrared, broadband interferometric techniques have been used to measure negative-index metamaterials (Dolling *et al* 2006, Zhang *et al* 2005). An ideal instrument for far-infrared characterization is a pulsed-laser-based broadband THz spectrometer, allowing vector spectra with a collimated beam (Adelberger and Cheung 1985, Mittleman 2003). It uses a sampling detector for tracing out the electric field oscillation of the THz pulse with a mechanical delay stage, and has been extended to even mid-infrared frequencies
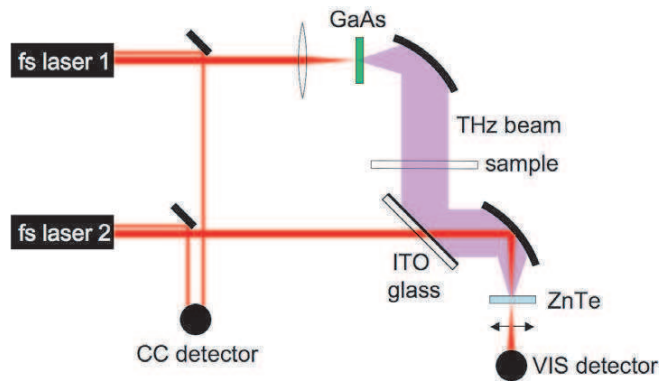
Figure 1. Optical layout of vector THz spectrometer using the ASOPS technique. To record complex THz amplitude and phase spectra, a trigger pulse is derived to mark the temporal overlap of the pulse trains from both lasers, generated here by cross correlating (CC) two sample beams split off the laser beams in a BBO crystal.

(Kübler *et al* 2005) yet metamaterials have been studied with this technique only in the far infrared (Azad *et al* 2008, Gomez Rivas *et al* 2003, Winnewisser *et al* 1999).

We suggest here metamaterial characterization by two recently introduced, coherent mid-infrared and THz spectrometers which contain *no moving parts*. Their laser-like beam can be well collimated, they measure vector information, and the absence of mechanical motion allows high-speed acquisition. The spectrometers' common, basic principle is the use of two pulsed laser beams with slightly different repetition frequencies, f_r and $f_r + \Delta$ (van der Weide and Keilmann 1998).

2. Far-infrared experiment

In a first configuration for THz vector spectrometry, one laser generates a THz beam (magenta in figure 1), whereas the other is used for asynchronuous electro-optic sampling of the THz pulse shape (ASOPS) (Bartels *et al* 2006, 2007, Yasui *et al* 2005, Yasui *et al* 2006). Such an 'asymmetric' THz spectrometer has recently illuminated a scattering-type scanning THz near-field microscope (von Ribbeck *et al* 2008). Here, we show that it can characterize metamaterials in a short time, which could be useful in studies of dynamic metamaterials (Chen *et al* 2008, Driscoll *et al* 2008). Our setup uses two 5W-laser-pumped Ti : S oscillators (FemtoSource Compact Pro, Femtolasers) emitting 10 fs pulses at 800 ± 50 nm wavelength, and $f_r = 125.11$ MHz. The first beam is focused with a 100 cm focal length lens onto a GaAs emitter (Tera-SED, Gigaoptics) biased at 10 V, to produce a 0.3–3 THz beam. This is collimated by a paraboloidal mirror with 25 mm effective focal length, and fully reflected by an ITO-coated glass slide (TS-GSHR, Bioscience Tools) which transmits the second Ti : S laser beam. Both are focused with a paraboloidal mirror with 25 mm effective focal length onto a 1 mm thick ZnTe crystal. The THz beam travels 25 cm in total. The sampling beam is split by a polarizing cube, and the signal of a differential detector (2107, New Focus) is recorded on a scope (WaveSurfer 422, LeCroy). In order to retrieve the phase information, ASOPS transients are recorded together
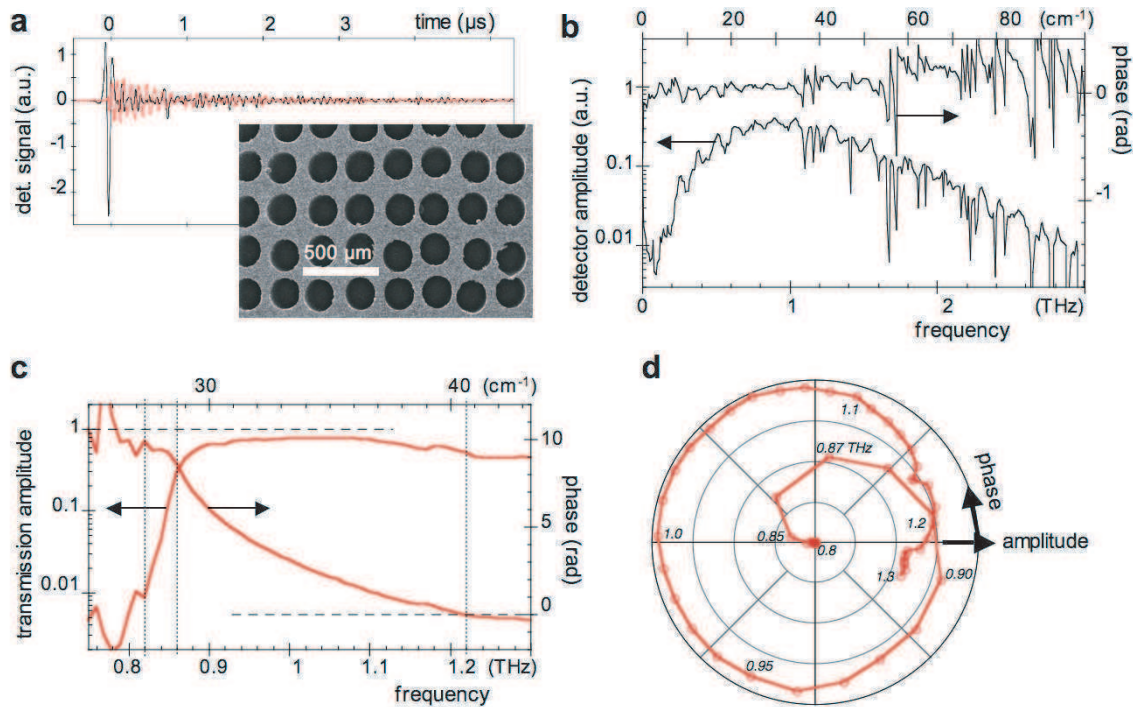
Figure 2. THz spectroscopy at normal incidence of a $t = 1$ mm thick brass plate with a nominally square array of $d = 204\,\mu$m dia. holes (inset: electron micrograph); (a) transients (averaged over 50 repeats, acquired within 1.4 s) with (red) and without (black) sample; (b) amplitude and phase spectra without sample, obtained by Fourier transforming the black transient in (a), showing signatures due to atmospheric absorption in the 25 cm long THz beam path (magenta in figure 1); (c) complex transmission spectrum of holey brass plate showing superluminal phase velocity and strong attenuation in the cutoff region (<0.86 THz), as well as high transmittance in the resonance region (0.9–1.1 THz); diffraction at the sample sets in at $c/g = 1.22$ THz; (d) polar plot of the complex transmission spectrum (c), with the frequency as parameter (amplitude in linear scale, from 0 to 0.8).

with trigger pulses. These are obtained as before (Brehm *et al* 2006, Schliesser *et al* 2005) by a BBO cross-correlator (CC in figure 1), which in this experiment is driven by two beams split off from the periphery of each laser beam by mirrors with sharp edges.

A piezoelectric transducer in one of the Ti : S lasers allows us to precisely set the offset frequency Δ, as before (Keilmann *et al* 2005, Schliesser *et al* 2005). We use $\Delta = 375.3$ Hz in order that the time dilatation factor becomes $f_r/\Delta = 333\,333$, such that a 1 THz oscillation appears down-sampled as a 1 THz/333 333 = 3 MHz oscillation. Transient pulses accordingly repeat at $\Delta = 375.3$ Hz rate, but much higher repetition rates could be obtained by setting a higher Δ, or by manipulating one of the lasers (Keilmann *et al* 2005, Schliesser *et al* 2005). We record the transients for 20 μs to obtain spectra at $(333\,333/20\,\mu\text{s}) = 0.017$ THz resolution, and perform on-line averaging of 35 transients s^{-1}, as limited by our oscilloscope, before Fourier transformation. The THz spectra (figure 2(b)) exhibit absorption lines from

the laboratory atmosphere. The phase is seen to decrease when an absorption resonance is approached from the low-frequency side, due to the increased refractive index, in accord with the sign convention of $\exp(2\pi i(ft - x/\lambda))$ for a wave propagating in the x-direction. The molecular lines cancel out completely when transmission spectra are calculated as ratios of spectra with and without sample (figure 2(c)), illustrating the excellent repeatability and resolution of the spectrometer.

3. Far-infrared results

We study a metallic metamaterial consisting of a square array of cylindrical holes drilled at a nominal period of $g = 246\,\mu$m into a $t = 1$ mm thick brass plate. The sample exhibits a broadband of high transmission (enhanced by $\approx 20\%$ over the areal fraction of the holes) near 1 THz, and this is accompanied by a monotonic phase change (figure 2(c)) which leads to an approximately circular trajectory in the complex transmission plane (figure 2(d)). Note this band is in the sub-diffractive frequency region $f < c/g$, well below the Wood anomaly given by the Rayleigh condition (Rayleigh 1907) $f_{\text{wood}} = c/g = 1.22$ THz that marks the onset of scattering into free-space diffraction orders. We assign this band to the leaky-wave resonance of a periodically corrugated or perforated metallic slab, here at frequency $f_{\text{res}} \approx 1$ THz $= 0.82\,c/g$. This resonance has first been analyzed and explained in the remarkable, pioneering work (Ulrich 1974) to arise from the interaction of the beam with modified Zenneck waves (Zenneck 1907) propagating in the plane of the guiding slab. Ulrich demonstrated in (Ulrich 1974), both in theory and experiment, that the periodic corrugations generate photonic Bloch waves and also a photonic band structure, and thereby he initiated no less than the physics of photonic crystals. In particular, he derived that on one hand there exist truly trapped or guided modes he named s_1 which are completely confined by the slab without any coupling to external radiation (like the 'spoof plasmons' on a corrugated metal surface of a later derivation (Pendry *et al* 2004) that, unfortunately, did not refer to Ulrich's work). Further he demonstrated that the slab also supports leaky modes—named 'guided resonances' in a related study (Fan and Joannopoulos 2002) and in a review (Garcia de Abajo 2007) of 'enhanced' optical transmission of hole arrays that unfortunately, also do not reference to (Ulrich 1974). These are directly connected to external radiation by the grating-coupling mechanism since the in-plane wavevector needs only to be conserved up to a reciprocal lattice vector. A leaky surface wave thus consists of two coupled parts, an evanescent surface wave and a free-space beam, as has been discussed in context with thermal emission from a metamaterial (Chan *et al* 2006, Laroche *et al* 2006). In our experiment the external beam is at normal incidence, and therefore, it has no electric field component normal to the slab: it cannot excite the lowest leaky mode (a_1), which is asymmetric in respect to the slab plane (Ulrich 1974). Efficient coupling occurs, however, to the next higher leaky mode (s_2), which is symmetric, and this coupling is so strong that a rather broad resonance results at $f_{\text{res}} < c/g$; its peak transmittance reaches 100% for the case of a perfect conductor (Ulrich 1974). A detailed experimental test of Ulrich's analytical model of leaky-wave coupling and of other theoretical developments reviewed in (Garcia de Abajo 2007) could be achieved in future by quantitative vector spectra (figures 2(c) and (d)). For this purpose higher-quality periodic structures are needed since the one used has evident irregularities.

The complex transmission spectrum (figure 2) gives further insight into wave propagation in and along the holes themselves because these are longer than a typical free-space wavelength, and have a large aspect ratio of depth t to diameter, of $t/d \approx 5$. Hollow metal waveguide

transport can thus be separated from the free-space-to-hole and hole-to-free-space couplings via surface waves at both surfaces (Keilmann 1981). A prominent property of hollow metal waveguides is their cutoff effect. It occurs below the cutoff frequency which for a perfectly conducting metal is $f_{cut} = 0.586 \, c/d$. In fact, we observe (figures 2(c) and (d)) that the transmission amplitude reduces sharply below $f_{cut} = 0.86 \, THz$ derived from $d = 204 \, \mu m$ in our sample. Interestingly, the phase of transmission stays advanced throughout the cutoff region $f \leqslant f_{cut}$ at about 9 rad compared to free space. While an advance of the order of 1 rad can be expected from the combined input and output couplings, as known from thin metal mesh where the holes do not contribute a waveguide propagation (see the results of figures 4 and 5, and of Winnewisser *et al* (2000)), the main effect of about 8 rad advancement can be attributed to superluminal propagation along the holes. Thus we derive the phase velocity in the waveguides to be $v_{ph} = c(1 + 8c/(2\pi f t)) = 14 \, c$ in the cutoff frequency region. Theoretically the phase velocity in perfectly conducting waveguides is infinite at and below f_{cut}, but this presents no contradiction; rather, a reduced velocity is to be expected from absorption and roughness scattering at the guide walls (Keilmann 1981) and could well serve to determine these hard-to-access quantities with high sensitivity. Note that the vector THz spectrometer (figure 1) could easily be adapted to measure also complex reflection spectra.

4. Mid-infrared experiment

In a second configuration of frequency-comb Fourier-transform spectrometer (c-FTS) for *infrared vector spectrometry*, we generate two infrared beams which we superimpose. To understand the basic principle, consider the frequency domain. Both infrared beams have harmonic frequency-comb spectra, regular sequences of modes with frequencies nf_r and $n(f_r + \Delta)$, respectively, caused by the regular pulse repetition and the process of frequency difference generation (Schliesser *et al* 2005). The offset Δ is chosen small enough that a low-frequency beating occurs only between the elements of both combs that have identical harmonic number n, at beat frequencies $n\Delta$. Then the beat spectrum uniquely replicates the infrared spectrum at the time-dilatation factor f_r/Δ (Keilmann *et al* 2004, Schliesser *et al* 2005, van der Weide and Keilmann 1998) chosen here with $\Delta = 25.02 \, Hz$ to be 500 000, such that a 30 THz mid-infrared oscillation appears down-scaled as a $30 \, THz/500 \, 000 = 6 \, MHz$ oscillation. Here we demonstrate the capability of mid-infrared c-FTS to acquire amplitude and phase transmission spectra. Our setup (figure 3) is a simpler version of our earlier arrangement for demonstrating the acquisition of amplitude and phase spectra of back-scattering from the tip of a scattering-type, 'apertureless' near-field microscope (s-SNOM) (Brehm *et al* 2006).

The Ti:S lasers and the trigger arrangement are identical to the THz experiment of figure 1. The infrared beams are generated by focusing the laser beams onto 200 μm thick GaSe crystals oriented between 50° and 65°, for the difference-frequency generation of 9 THz wide spectra in the 20–40 THz range, equivalent to 8–15 μm wavelength. In contrast with former setups, (Brehm *et al* 2006, Keilmann *et al* 2004, Schliesser *et al* 2005) the beams are not superimposed on a dielectric beam combiner. Instead, we use wavefront combination by a mirror with a sharp edge (Ganz *et al* 2008) to avoid a dielectric plate and the associated problems of multiple reflections and dielectric dispersion. This choice should be especially useful for extending the instrument to super-decade-wide infrared spectra (Kübler *et al* 2005). The infrared beams are refocused at 95 cm, by Au-coated paraboloidal mirrors with 25 mm effective focal length. The resulting 1–2 mm diameter spot allows us to measure small-size
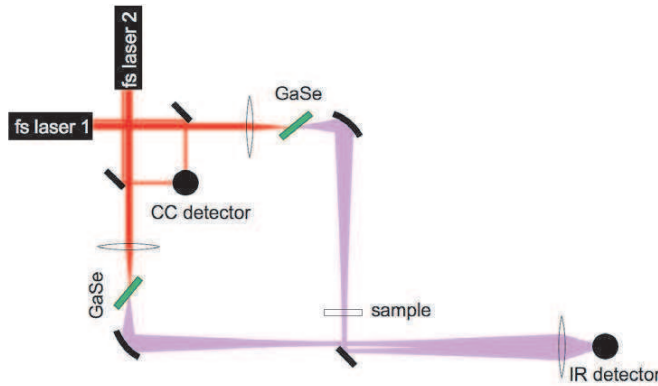
Figure 3. Optical layout of vector mid-IR spectrometer with no moving part. Two mid-infrared frequency-comb beams are generated by difference frequency generation in GaSe and adjusted for parallel propagation. Interference occurs on an HgCdTe infrared detector and results in self-scanned, repetitive inteferograms. With the sample in one of the beams, transmission spectra are recorded in amplitude and phase simultaneously.

samples at well-defined incidence angles, as the beam convergence angle is only about $0.8°$ full width at half maximum (FWHM). For initial alignment we temporarily place a 2 mm diameter HgCdTe detector just after the combining mirror, to maximize the signal of each beam. The beams are adjusted for parallel propagation at about 2 mm center-to-center distance, by translating and orienting the mirror which has a sharp edge, and they are focused after 105 cm by an $f = 25$ mm Ge lens onto a $200\,\mu$m diameter HgCdTe detector (KMPV11, Kolmar). The signal is preamplified at 30 MHz bandwidth and recorded on an oscilloscope (WaveSurfer 422, LeCroy). Transient interferograms appear at a rate of 25.02 Hz and are recorded for $6.1\,\mu$s, giving a spectral resolution of $(f_r/\Delta)/6.1\,\mu$s $= 0.8$ THz equivalent to $2.7\,\text{cm}^{-1}$. For averaging over typically 1000 transients in 40 s we stabilize Δ by sending the cross-correlator trigger signal to a lock-in amplifier (Stanford Research 510) which is externally referenced at 25.02 Hz, and by applying the X output at 100 ms time constant to the piezoelectric transducer. This simple arrangement allows a hold range of ±0.7 V equivalent to ±1 Hz, sufficient to stabilize against thermal drifts over several minutes. To understand the infrared comb-FT spectrometer's vector capability, especially for measuring phase spectra, consider the field amplitude

$$E(t) = \sum_{n=M}^{N} E_n \cos\left(2\pi\,nf_r t + \varphi_n\right),$$

of one beam, and

$$E'(t) = \sum_{n=M}^{N} E'_n \cos\left(2\pi\,n\,(f_r + \Delta)\,t + \varphi'_n\right)$$

of the other, where a choice of $M \approx 160\,000$ and $N \approx 320\,000$ would span the range from $Mf_r = 20$ THz to $Nf_r = 40$ THz, equivalent to $667\,\text{cm}^{-1}$ to $1334\,\text{cm}^{-1}$. The detector signal $U(t) \propto (E(t) + E'(t))^2$ contains, apart from two dc terms, several series of interference terms. Choosing $\Delta < f_r/2N \approx 195$ Hz assures that only one series,

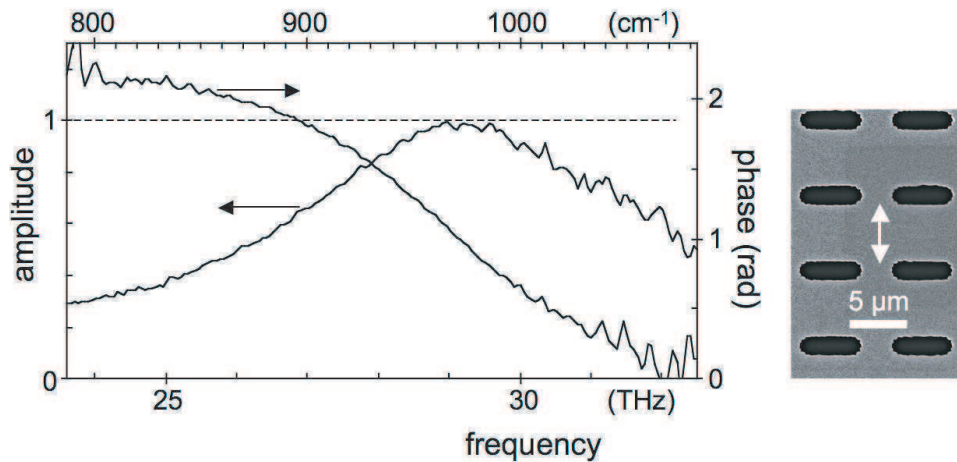$$\sum_{n=M}^{N} E_n E'_n \cos\left(2\pi\,n\Delta t + \varphi'_n - \varphi_n\right),$$

Figure 4. Complex transmission spectrum of $2\,\mu$m thick Au foil with rounded rectangular holes arranged at periods $g = 8\,\mu$m and $6.6\,\mu$m, respectively, for the directions parallel and perpendicular to the ellipses; inset: electron micrograph of sample, with electric field orientation indicated by arrow (as likewise in the following figures).

lies in the frequency range $< f_r/2$ and can be selected using a low-pass filter at $< f_r/2 \approx 63$ MHz. This signal's radio-wave spectrum is the direct replica of the mid-IR spectrum. In particular, its phase spectrum is identical to the infrared phase spectrum.

5. Mid-infrared results

Metamaterials of periodically perforated metal sheets are chosen to demonstrate the capabilities of c-FTS vector spectroscopy in the mid infrared. Near unity transmittance is observed with the metamaterial structure in figure 4, due to the s_2 leaky-wave resonance mentioned above, (Ulrich 1974) here at $f_{res} \approx 975\,\text{cm}^{-1} = 0.78\,c/g$ which is again considerably lower than the onset of diffraction at $f_{Wood} = c/g = 1250\,\text{cm}^{-1}$. Note that at resonance the transmission is sixfold enhanced over the area fraction occupied by the holes of only about 17%. This means that the average infrared intensity in the holes is more than sixfold enhanced over the incident (and likewise the transmitted) far-field intensity. The phase advances continuously from about zero as the resonance is traversed from the high-frequency side. Since the holes have a rather small depth $t/\lambda \approx 0.2$, we can expect that waveguiding effects in the holes are of minor importance to the transmission; both the amplitude and the phase spectra are dominated by the coupling effects of free-space waves into and out of the hole array. Here, we note that a special kind of a transmittance resonance has been theoretically described (Garcia-Vidal *et al* 2005) and measured (Lee *et al* 2006, 2007, Ruan and Qiu 2006) for a *single* hole shaped and oriented similarly as in figure 4; it occurs at $f_s \approx c/2L$, where L is the width of the hole; thus for a single hole with $L \approx 5\,\mu$m as in our sample one would expect $f_s \approx 1000\,\text{cm}^{-1}$.

In figure 5, we show results of measuring a more open metamaterial with square symmetry. The spectrometer's range was set to cover both the resonant-transmission and Wood anomaly regions. At normal incidence, the onset of diffraction leaves a marked signature at $f_{Wood} = c/g = 1250\,\text{cm}^{-1}$ (dashed vertical line). It is well known that the Wood anomaly is expressed
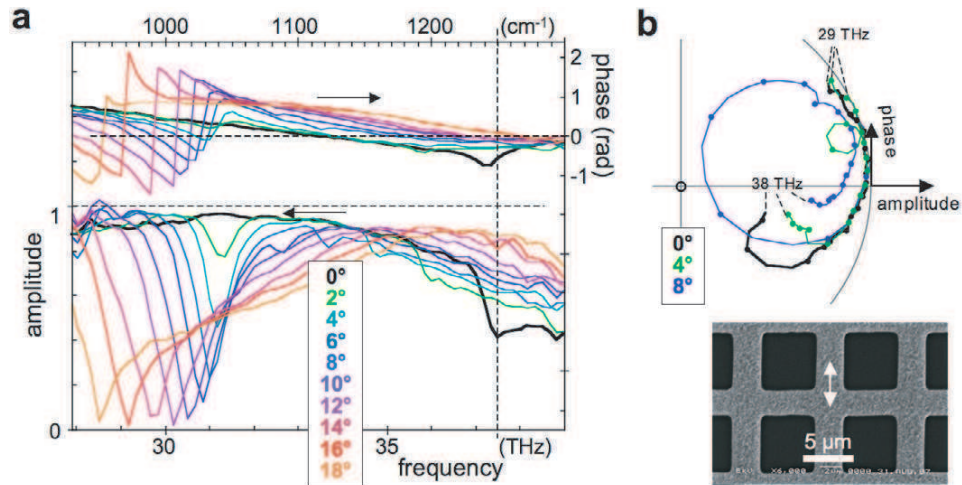
Figure 5. Complex transmission spectra (a) of a $t = 1 \, \mu$m thick Au foil with square holes of 3.5 mm width arranged at period $g = 8 \, \mu$m, taken at varied incidence angles α (p-polarization); diffraction at the sample sets in at $c/g = 1250 \, \text{cm}^{-1}$; (b) complex polar plot of amplitude and phase data from (a) for three angles, with the marked points separated by 0.5 THz (amplitude in linear scale, from 0 to 1).

in a stepwise decrease of the (zeroth order) transmittance when power is carried away into four first-order diffracted beams emanating at grazing angles. What our spectrometer reveals is that this onset of diffraction also induces a characteristic dip structure in the transmission phase spectrum. At non-normal incidence, both these amplitude and phase signatures tune pairwise according to the expected relation $f_{\text{Wood}} = (1 \pm \sin \alpha)^{-1} c/g$.

The transmission resonance due to the s_2 leaky-wave interaction (figure 5(a)) reaches near-unity amplitude at $f_{\text{res}} \approx 1050 \, \text{cm}^{-1} = 0.84 \, c/g$. In addition, but only at non-normal incidence, the transmission spectrum shows the onset of a marked amplitude dip at about $1040 \, \text{cm}^{-1}$ and a marked phase signature. Already at $4°$ the dip reaches down to 50% transmission amplitude, equivalent to a transmitted power of only 25%. This sharp resonance with a Q-value of $f/\Delta f$ (FWHM) ≈ 50 originates from the excitation of an a_1 leaky wave which has its field oriented normally (Ulrich 1974) hence its excitation must vanish at normal incidence. Since this a_1 resonance (high-Q) occurs within the broad band of the s_2 resonance (low-Q), the resulting transmission line shape expresses the interference of two interactions ('direct and indirect pathways' in (Fan and Joannopoulos 2002)), and therefore it is in this respect analogous to Fano's analysis (Fano 1961) of a sharp transition interfering with a continuum (Ulrich 1974). Our measurement is capable of supplying the complete information on this coupling resonance including the phase signature. For an illustration we plot three of the spectra of figure 5(a) in a polar diagram where the transmission amplitude and phase are the coordinates (figure 5(b)). The spectra in the coupling resonance region describe approximately circular trajectories which are traversed clockwise with rising frequency. Relative to such a_1 coupling features, the Wood anomaly appears as a smaller effect that describes an arc also traversed clockwise.

In the coupling dip, the missing power is converted via the a_1 surface wave (whose wavelength λ_{SPP} matches the condition $1/\lambda_{\text{SPP}} = 1/g - (\sin \alpha)/\lambda$) both into metal absorption
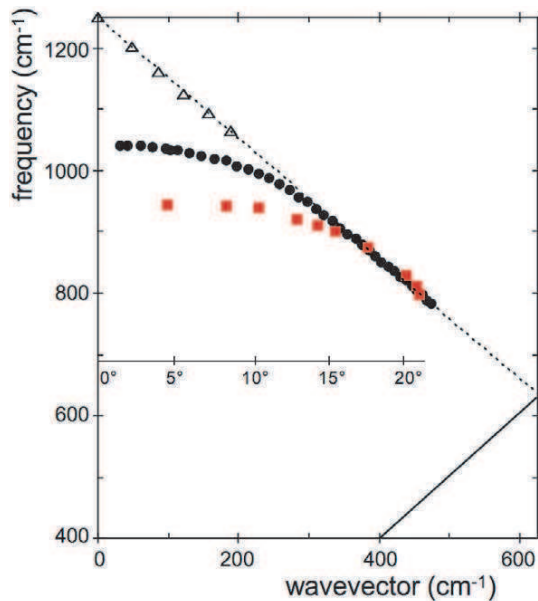
Figure 6. Dispersion of the a_1 leaky wave (black dots) determined from the positions of the coupling dip minima in figure 5(a); open triangles mark the Wood anomaly; the corresponding angle of incidence can be read from the inserted scale. Also shown is the light line (full), and its back-folded continuation (dashed) beyond the Brillouin zone edge. Also shown is the dispersion (red squares) of the leaky wave determined for the sample of figure 7.

and into a reflected beam. Extracting the resonances' spectral positions, taken at the dip minima, allows us to construct the dispersion relation of the excited a_1 leaky wave (figure 6; the open triangles taken at the amplitude minima represent the Wood anomaly; they exhibit linear dispersion because it represents first-order diffraction into a free-space wave).

The a_1 leaky surface wave on the sample in figure 5 asymptotically approaches, at $0°$, a frequency of about $1040\,\mathrm{cm}^{-1}$ and a phase velocity of $1040/1250 = 0.83\,c$; the coupling to external radiation vanishes. Caution is advised in interpreting the observed $Q \approx 50$ to be solely governed by nonradiative damping of the a_1 evanescent wave part, by absorption in the metal (Ulrich 1974). Rather, the resonance can be inhomogeneously broadened by residual wrinkle of the stretched foil; an additional mechanism is contributed by the mere width of our probing beam: when we assume $1\,\mathrm{mm}$ width, the transit time of the surface wave is $T = 1\,\mathrm{mm}/0.83\,c$ which induces a homogeneous broadening of $1/T = 8.3\,\mathrm{cm}^{-1}$.

The sample in figure 7 has the same periodicity and exhibits a similar light transmission resonance due to the s_2 leaky-wave interaction, at $f_{\mathrm{res}} \approx 1000\,\mathrm{cm}^{-1} = 0.8\,c/g$. Yet in contrast, the asymptotic frequency and phase velocity of its a_1 mode are both considerably reduced to about $930\,\mathrm{cm}^{-1}$ and $930/1250 = 0.76\,c$, respectively. It takes higher incidence angles α to observe a red-shifting of the dip which merges with the Wood feature above about $15°$. In the polar plot in figure 7(b) the Wood and a_1 coupling features can be distinguished in the $10°$ and $14°$ trajectories, the latter as rather weak loops, but no longer at $22°$ where they form a strong combination signature. The overall transmission is retarded in this sample by about $1\,\mathrm{rad}$, and
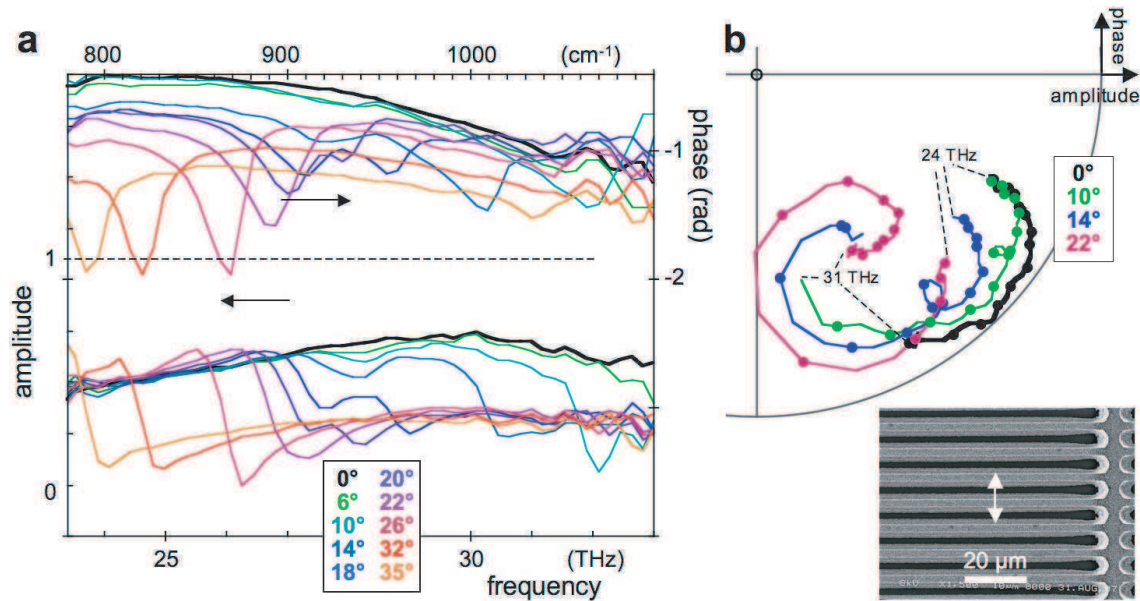
Figure 7. Complex transmission spectra (a) of a $t = 8\,\mu$m thick Au foil with $4\,\mu$m wide and $500\,\mu$m long slits arranged at period $g = 8\,\mu$m, taken at varied incidence angles α (p-polarization); (b) complex polar plot of amplitude and phase data from (a) for four angles, with the marked points separated by 0.5 THz (amplitude in linear scale, from 0 to 1).

even more at oblique incidence. This might be caused by a Fabry–Perot resonance in the deep slits, but not by a reduced phase velocity which should equal c for a TEM mode in a parallel-plate waveguide (Jackson 1975, Mendis and Grischkowsky 2001).

6. Outlook for metamaterials

The metamaterials investigated here do not contain deeply subwavelength structure elements that possess localized electric and magnetic resonances as needed to induce a negative refractive index. Yet we expect that it will be with such samples that vector c-FTS can serve with its quantitative measurement capabilities, given the ease demonstrated here of taking amplitude and phase spectra at well-controlled directions of both beam propagation and electric field. To retrieve effective-medium dielectric and magnetic functions from vectorial spectra, appropriate Fresnel-type analytic expressions have been given (Chen *et al* 2004, Smith *et al* 2002). A sensitive quantity is the slab thickness applicable to the case of single-layer metamaterials such as holey metal films. In practice, this thickness has been assumed equal to the in-plane unit-cell period (Driscoll *et al* 2007, Padilla *et al* 2007). Two-layer structures have allowed a better-defined determination, in two cases with an out-of-plane period which was about an order of magnitude smaller than the in-plane period (Dolling *et al* 2006, Zhang *et al* 2005). Experimentally retrieved optical constants of 1–4 layer metamaterials have recently been reported (Azad *et al* 2008). Quite generally the probing wavelength should greatly exceed the period of the metamaterial elements (this requirement, however, might have to

be relaxed to obtain a strong magnetic response (Rockstuhl *et al* 2007)). Otherwise optical probing does not deal with the effective dielectric and magnetic responses alone. Rather, a rich set of surface and bulk excitations, such as the a_1 leaky-wave and Wood interactions in the above examples, contributes characteristic signatures. These depend on incidence angle and beam width, and need to be understood and corrected for to avoid artefacts in the electric permittivity and magnetic permeability functions. Note these quantities might even be intrinsically non-local because inter-element coupling causes them to depend on momentum, not just frequency (Garcia de Abajo and Saenz 2005, Koschny *et al* 2005).

In conclusion, we have demonstrated amplitude and phase spectra by a vector comb-based spectrometer. It has enabled us to present complex-valued transmission spectra of metal hole arrays and identify phenomena such as leaky-wave interaction and cutoff-waveguide propagation. The method can characterize the optical properties of metamaterials more completely than previously possible, and may help to resolve issues such as the origin of negative refraction or the non-locality of dielectric and magnetic responses.

Acknowledgments

References

Auston D H and Cheung K P 1985 Coherent time-domain far-infrared spectroscopy *J. Opt. Soc. Am.* B **2** 606–12

Azad A K, Chen H T, Akhadov E, Weisse-Bernstein N R, Taylor A J and O'Hara F F 2008 Multi-layer planar tetrahertz electric metamaterials on flexible substrates *CLEO/QELS* abstract CTuD4

Bartels A, Cerna R, Kistner C, Thoma A, Hudert F, Janke C and Dekorsy T 2007 Ultrafast time-domain spectroscopy based on high-speed asynchronuous optical sampling *Rev. Sci. Instrum.* **78** 035107

Bartels A, Thoma A, Janke C, Dekorsy T, Dreyhaupt A, Winnerl S and Helm M 2006 High-resolution THz spectrometer with kHz scan rates *Opt. Express* **14** 430–7

Brehm M, Schliesser A and Keilmann F 2006 Spectroscopic near-field microscopy using frequency combs in the mid-infrared *Opt. Express* **14** 11222–33

Chan D L C, Celanovic I, Joannopoulos J D and Soljacic M 2006 Emulating one-dimensional resonant *Q*-matching behavior in a two-dimensional system via Fano resonances *Phys. Rev.* A **74** 064901

Chen H T, O'Hara J F, Azad A K, Taylor A J, Averitt R D, Shrekenhamer D B and Padilla W J 2008 Experimental demonstration of frequency-agile tetrahertz metamaterials *Nat. Photonics* **2** 295–8

Chen X, Grzegorczyk T M, Wu B I, Pacheco J and Kong J A 2004 Robust method to retrieve the constitutive effective parameters of a metamaterial *Phys. Rev.* E **70** 016608

Dolling G, Enkrich C, Wegener M, Soukoulis C M and Linden S 2006 Simultaneous negative phase and group velocity of light in a metamaterial *Science* **312** 892–4

Driscoll T, Andreev and Basov D N 2007 Quantitative investigation of a tetrahertz artificial magnetic resonance using oblique angle spectroscopy *Appl. Phys. Lett.* **90** 092508

Driscoll T, Palit S, Qazilbash M M, Brehm M, Keilmann F, Chae B G, Kim H T, Cho S Y, Jokerst N M and Basov D N 2008 Dynamic tuning of an infrared hybrid-metamaterial resonance using VO_2 *Appl. Phys. Lett.* **93** 024101

Fan S and Joannopoulos J D 2002 Analysis of guided resonances in photonic crystal slabs *Phys. Rev.* B **65** 235112

Fano U 1961 Effects of configuration interaction on intensities and phase shifts *Phys. Rev.* **124** 1866–78

IOP Institute of Physics ⚽ DEUTSCHE PHYSIKALISCHE GESELLSCHAFT

Ganz T, Ribbeck H G v, Brehm M and Keilmann F 2008 Compact frequency-comb Fourier-transform infrared spectrometer *Opt.Commun.* **281** 3827–30

Garcia de Abajo F J 2007 Light scattering by particle and hole arrays *Rev. Mod. Phys.* **79** 1267–90

Garcia de Abajo F J and Saenz J J 2005 Electromagnetic surface modes in structured perfect-conductor surfaces *Phys. Rev. Lett.* **95** 233901

Garcia-Vidal F J, Moreno E, Porto J A and Martin-Moreno L 2005 Transmission of light through a single rectangular hole *Phys. Rev. Lett.* **95** 103901

Gomez Rivas J, Schotsch C, Haring Bolivar P and Kurz H 2003 Enhanced transmission of THz radiation through sub-wavelength holes *Phys. Rev.* B **68** 201306

Hillenbrand R and Keilmann F 2001 Optical oscillation modes of plasmon particles observed in direct space by phase-contrast near-field microscopy *Appl. Phys.* B **73** 239–43

Hillenbrand R, Keilmann F, Hanarp P, Sutherland D S and Aizpurua J 2003 Coherent imaging of nanoscale plasmon patterns with a carbon nanotube optical probe *Appl. Phys. Lett.* **83** 368–70

Jackson J D 1975 *Classical Electrodynamics* (New York: Wiley)

Jia B, Norton A H, Li J, Rahmani A, Asatryan A A, Botten L C and Gu M 2008 Local observation of modes from three-dimensional woodpile photonic crystals with near-field microspectroscopy under supercontinuum illumination *Opt. Lett.* **33** 1093–5

Keilmann F 1981 Infrared high-pass filter with high contrast *Int. J. Infrared Millimeter Waves* **2** 259–72

Keilmann F, Gohle C and Holzwarth R 2004 Time-domain mid-infrared frequency-comb spectrometer *Opt. Lett.* **29** 1542–4

Keilmann F, Schliesser A, Brehm M and Ocelic N 2005 Verfahren und Vorrichtung zur Abtastung von sich periodisch wiederholenden Ereignissen *German Patent* 102005050151

Koschny T, Markos P, Economou E N, Smith D R, Vier D C and Soukoulis C M 2005 Impact of inherent periodic structure on effective medium description of left-handed and related materials *Phys. Rev.* B **71** 245105

Kübler C, Huber R and Leitenstorfer A 2005 Ultrabroadband tetrahertz pulses: generation and field-resolved detection *Semicond. Sci. Technol.* **20** S128–33

Laroche M, Carminati R and Greffet J J 2006 Coherent thermal antenna using a photonic crystal slab *Phys. Rev. Lett.* **96** 123903

Lee J W, Seo M A, Kang D H, Khim K S, Jeoung S C and Kim D S 2007 Tetrahertz electromagnetic wave transmission through random arrays of single rectangular holes and slits in thin metallic sheets *Phys. Rev. Lett.* **99** 137401

Lee J W, Seo M A, Park D J and Kim D S 2006 Shape resonance omni-directional tetrahertz filters with near-unity transmittance *Opt. Express* **14** 1253–9

Mandelshtam L I 1950 Lectures of some problems of the theory of oscillations *Complete Collection of Works* (Moscow: Academy of Sciences) pp 428–67

Mendis R and Grischkowsky D 2001 Undistorted guided-wave propagation of subpicosecond THz pulses *Opt. Lett.* **26** 864–48

Mittleman D 2003 *Sensing with THz Radiation* (Berlin: Springer)

Padilla W J, Aronsson M T, Highstrete C, Lee M, Taylor A J and Averitt R D 2007 Electrically resonant tetrahertz metamaterials: theoretical and experimental investigations *Phys. Rev.* B **75** 041102

Padilla W J, Smith D R and Basov D N 2006 Spectroscopy of metamaterials from infrared to optical frequencies *J. Opt. Soc. Am.* B **23** 404–13

Pendry J B, Matrin-Moreno L and Garcia-Vidal F J 2004 Mimicking surface plasmons with structured surfaces *Science* **305** 847–8

Rayleigh L 1907 Note on the remarkable case of diffraction spectra described by Prof Wood *Phil. Mag.* **14** 60–1

Rockstuhl C, Zentgraf T, Pshenay E, Petschulat J, Chipouline A, Kuhl J, Pertsch T, Giessen H and Lederer F 2007 The origin of magnetic polarizabilizy in metamaterials at optical frequencies—an electrodynamic approach *Opt. Express* **15** 8871–83

IOP Institute of Physics Φ DEUTSCHE PHYSIKALISCHE GESELLSCHAFT

Ruan Z and Qiu M 2006 Enhanced transmission through periodic arrays of subwavelength holes: the role of localized waveguide resonances *Phys. Rev. Lett.* **96** 233901

Schliesser A, Brehm M, van der Weide D W and Keilmann F 2005 Frequency-comb infrared spectrometer for rapid, remote chemical sensing *Opt. Express* **13** 9029–38

Smith D R, Padilla W J, Vier D C, Nemat-Nasser S C and Schultz P G 2000 Composite medium with simultaneously negative permeability and permittivity *Phys. Rev. Lett.* **84** 4184–7

Smith D R, Shultz S, Markos P and Soukoulis C M 2002 Determination of effective permittivity and permeability of metamaterials from reflection and transmission coefficients *Phys. Rev.* B **65** 195104

Ulrich R 1974 Modes of propagation on an open periodic waveguide for the far infrared *Optical and Acoustical Micro-Electronics* ed J Fox (New York: Polytechnic Press) pp 359–76

Valk N C J and Planken P C M 2002 Electro-optic detection of subwavelength terahertz spot sizes in the near field of a metal tip *Appl. Phys. Lett.* **81** 1558–60

van der Weide D and Keilmann F 1998 Coherent periodically pulsed radiation spectrometer US Patent 5748309 (filed 20 October 1994)

Veselago V G 1968 The electrodynamics of substances with simultaneously negative values of ε and μ *Sov. Phys.— Usp.* **10** 509–14

von Ribbeck H G, Brehm M, van der Weide D, Winnerl S, Drachenko O, Helm M and Keilmann F 2008 Spectroscopic THz near-field microscope *Opt. Express* **16** 3430–8

Winnewisser C, Lewen F, Weinzierl J and Helm H 1999 Transmission features of frequency-selective components in the far-infrared determined by terahertz time-domain spectroscopy *Appl. Opt.* **38** 3961–7

Winnewisser C, Lewen F T, Schall M, Walther M and Helm H 2000 Characterization and application of dichroic filters in the 0.1–3 THz region *IEEE Trans. Microw. Theory Tech.* **48** 744–9

Yasui T, Kabetani Y, Saneyoshi E, Yokoyama S and Araki T 2006 Tetrahertz frequency-comb by multifrequency heterodyning photoconductive detection for high-accuracy, high-resolution terahertz spectroscopy *Appl. Phys. Lett.* **88** 241104

Yasui T, Saneyoshi E and Araki T 2005 Asynchronous optical sampling terahertz time-domain spectroscopy for ultrahigh spectral resolution and rapid data acquisition *Appl. Phys. Lett.* **87** 61101

Yen T J, Padilla W J, Fang N, Vier D C, Smith D R, Pendry J B, Basov D N and Zhang X 2004 Tetrahertz magnetic response from artificial materials *Science* **303** 1494–6

Yu N, Cubukcu E, Diehl L, Belkin M A, Crozier K B, Capasso F, Bour D, Corzine S and Höfler G 2007 Plasmonic quantum cascade laser antenna *Appl. Phys. Lett.* **91** 173113

Zenneck J 1907 Über die Fortpflanzung ebener elektromagnetischer Wellen längs einer ebenen Leiterfläche und ihre Beziehung zur drahtlosen Telegraphie *Ann. Phys.* **23** 846–66

Zentgraf T, Dorfmüller J, Rockstuhl C, Etrich C, Vogelgesang R, Kern K, Pertsch T, Lederer F and Giessen H 2008 Amplitude- and phase-resolved optical near fields of split-ring-resonator-based metamaterials *Opt. Lett.* **33** 848–50

Zhang S, Fan W, Panoiu N C, Malloy K J, Osgood R M and Brueck S R J 2005 Experimental demonstration of near-infrared negative-index metamaterials *Phys. Rev. Lett.* **95** 137401

Compact frequency-comb Fourier-transform infrared spectrometer

T. Ganz, H.G. von Ribbeck, M. Brehm, F. Keilmann *

Max-Planck-Institut für Biochemie & Center for NanoScience (CeNS), 82152 Martinsried (München), Germany

Received 9 December 2007; received in revised form 19 March 2008; accepted 25 March 2008

Abstract

We demonstrate a Fourier-transform infrared (FTIR) spectrometer without moving parts based on frequency-combs where the interference of two coherent frequency-comb beams occurs via wavefront combination, thereby eliminating the need of a dielectric combiner. This enables dispersionless operation over eventually the complete THz-to-visible spectrum in a single instrument. Furthermore we demonstrate the use of a single GaSe crystal for generating both beams, in an implementation for the 22–36 THz mid-infrared range. Spurious cross-modulation effects and a way to eliminate them are experimentally demonstrated. The compact comb-FTIR can be equally well applied for spectroscopic microscopy as for long-path standoff chemical monitoring.
© 2008 Elsevier B.V. All rights reserved.

Fourier-transform spectrometers (FTS) without moving part based on frequency-combs were first described for the THz range, [1–3] then for the mid-infrared [4–7]. Their principle was also proposed in Ref. [8]. They overcome the necessity of a mechanical delay stage that is commonly employed in FTS and also in THz sampling systems. Instead, a self-scanning principle is used which operates purely in the time domain and therefore enables unlimited retardation and spectral resolution [9,10]. The spectrometer is based on superimposing two coherent frequency-comb beams. The coherent nature of the resulting "dual" spectrometer beam allows a long measurement path which is useful for environmental and standoff investigations. It also enables diffraction-limited focusing for microscopic and also near-field-nanoscopic imaging [7]. For reading out the spectral information either a power detector periodically records interferograms, or an electro-optic sampling system periodically records waveforms [11–13]. In both cases the spectrum is obtained by subsequent Fourier transformation. The direct-detector case can be viewed as a multi-heterodyne receiver system [4]. Its periodic interferograms arise as the superposition of a large number of beat oscillations, each of which results from a pairwise cross-comb mixing. As outlined earlier [4,5], the beams' mode frequencies need to form harmonic series nf_r and $nf_{r+\Delta}$, with base frequencies f_r and $f_{r+\Delta}$ for comb 1 and comb 2, respectively, in order that also the beat frequencies $n\Delta$ form a harmonic series of base frequency Δ. Then this beat frequency comb constitutes a faithful low-frequency replica of the THz or mid-infrared beam spectra, and the interferograms appear at rate Δ.

Our compact comb-FTIR (Fig. 1) combines two visible beams, at 800 ± 50 nm wavelength, from Ti:S oscillators (FemtoSource Compact Pro, Femtolasers) into a parallel bundle, by using a flat mirror with a sharp edge. Both lasers are mode-locked to give 10 fs pulses which repeat at the rate $f_r = 125.11$ MHz. The beams have 2 mm diameter and are set to 2 mm center-to-center distance. After 34 cm the beams are focused with a common $f = 18$ mm lens onto a common 200 μm GaSe crystal for difference frequency generation (DFG). Note this arrangement is not only simpler than previously, [4,5] but it furthermore provides equal incidence parameters for both beams. This ensures the mid-infrared beams co-propagate and are fully matched in respect to spectrum, polarization and collimation, all of which are prerequisites for maximum modulation of the interferograms. The visible laser beams are polarized horizontal, and the GaSe plane of incidence is rotated by 45°. The crystal is oriented at 52° incidence from

---
* Corresponding author. Tel.: +49 89 8578 2617; fax: +49 89 8578 2641.
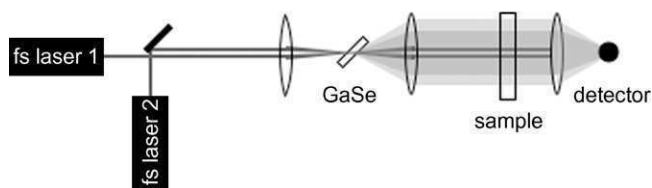*E-mail address:* keilmann@biochem.mpg.de (F. Keilmann).

Fig. 1. Compact mid-IR coherent-comb spectrometer (comb-FTIR). The visible beams of two independent Ti:S lasers are aligned for close, parallel co-propagation and focused on a single GaSe crystal. The generated mid-infrared beams are collimated and transmitted through a sample to the detector. On-line Fourier transformation of the signal produces a continuous sequence of mid-infrared spectra, without involving any moving part.

the normal for difference-frequency generation covering the 20–40 THz range, equiv. to 8–15 μm wavelength.

After recollimation by a gold-coated paraboloid mirror with 25 mm effective focal length the near-visible beams co-propagate in approximately 3 mm distance. The mid-infrared beams have approx. 15 μW power [5]. They have approximately 13 mm diameter (FWHM) due to diffractive spreading inside and beyond the GaSe crystal, and thus overlap and interfere sufficiently for considerable partial interference ("diffracting" interferometer [14]). Note the method of wavefront recombination has since long been used in interferometric infrared spectrometers [15]. After a distance of 23 cm we place an a.r. coated, $f = 25$ mm Ge lens to focus the mid-infrared beams on a 200 μm diameter HgCdTe detector (KMPV11, Kolmar). The signal is preamplified with 30 MHz bandwidth and recorded by a scope (wavesurfer 422, LeCroy). As in earlier experiments [5,7] we use a piezoelectric transducer in one of the Ti:S lasers to precisely set its pulse repetition frequency. In the present case we choose as before [5] an offset frequency of $\Delta = 83.47$ Hz in order that a beat frequency $b = 20$ MHz replicates the mid-infrared frequency $b f_r / \Delta = 30$ THz (equiv. to 10 μm wavelength).

Transient interferograms or beat pulses are readily observed to appear at $\Delta = 83.47$ Hz rate, but the storage and computational limits of the oscilloscope limit the rate of averaging to 19 spectra/s. Although the beat pulses appear with a signal-to-noise ratio of about 15 which suffices for internal triggering, we operate with an external trigger signal obtained as in our former study [7] by a BBO cross-correlator. For this purpose we split off two beams from the periphery of each of the oscillator output beams, again by metallized mirrors with a sharp edge (not shown in Fig. 1). Apart from providing a trigger for averaging we use this signal, as before, [7] also for actively stabilizing Δ to better than ±0.1 Hz. For this we apply the signal to a lock-in amplifier together with an 83.47 Hz external reference signal, and feed the X output directly to the piezotranslator of one of the lasers to compensate a slow thermal drift.

Fig. 2 shows a beat pulse or interferogram, together with its Fourier spectrum computed from a 6.1 μs long time window using Hamming apodization. The frequency axis has
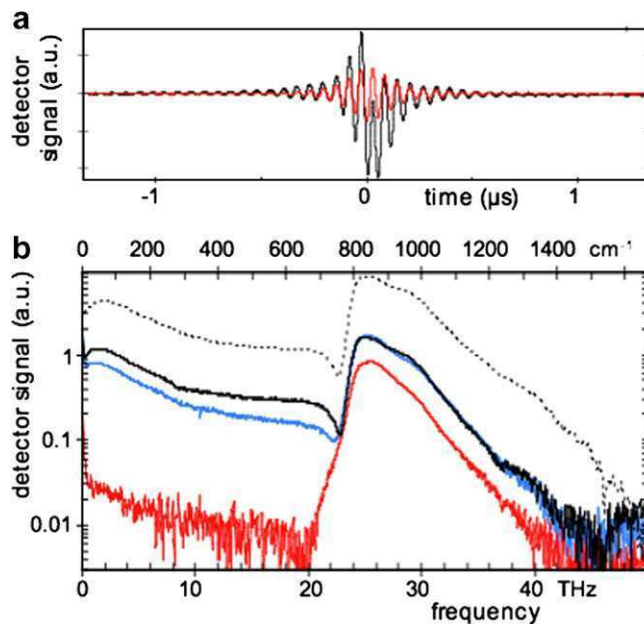

Fig. 2. Interferograms (a, 1000 avg.) and infrared spectra (b) from compact comb-FTIR. Δ was set to 83.47 Hz, equiv. to a frequency scaling factor of 1,500,000 (full curves), and to 25 Hz equiv. to 5,000,000, respectively (dotted). Note that the signal level increases in reciprocal proportion to Δ, as mathematical consequence of having kept the same time window duration. Signals below 20 THz are caused by unwanted cross-comb beating. This effect can be suppressed slightly (blue) or nearly completely (red) by adjusting the visible beams slightly (<1°) non-parallel (see text) (For interpretation of the references to colour in this figure legend, the reader is referred to the web version of this article.).

been scaled by the factor $f_r / \Delta = 1,500,000$, in order to convert from the 0–33.3 MHz beat scale to the 0–50 THz mid-infrared scale. The instrumental resolution is thus $1,500,000/6.1$ μs $= 0.25$ THz [4]. The obtained spectrum (black) has a form as expected for the range 23–40 THz.[5] However, below this range the spectrum exhibits a smooth background of unexpected beat components, to be discussed below. The spectral form stays largely unaffected when Δ is set to 25 Hz (broken curve in Fig. 2b). When placing a test sample in form of a 50 μm sheet of polystyrene in the collimated mid-infrared beam we observe that the spectrum reduces and develops characteristic absorption dips (Fig. 3). The intensity and spectral location of the dips correspond to the transmittance spectrum of the same sample taken by a conventional FTIR spectrometer (dotted).

The extra or background beats are not assignable to infrared modes below 20 THz because the detector cuts off at 20 THz. We rather assign them to modes in the 20–40 THz range whose frequencies are not harmonics of f_r and $f_{r+\Delta}$. Non-harmonic mid-infrared frequencies can only arise from DFG across both laser beams (see Appendix A). They can be suppressed, first of all, by avoiding the spatial overlap of the visible laser beams in the GaSe crystal. We tested this experimentally by adjusting the beams slightly non-parallel, using the mirror in Fig. 1. A drastic change is seen. The extra beats quickly disappear whereas
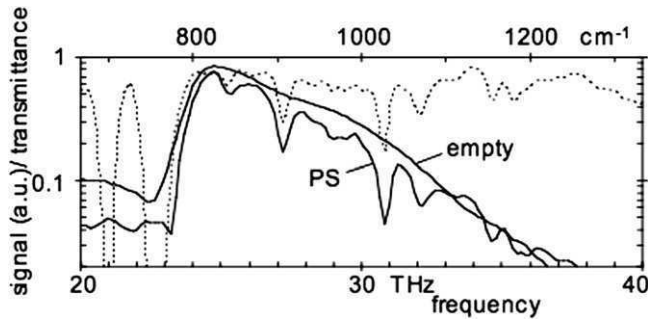
Fig. 3. Infrared spectra (1000 avg.) from compact comb-FTIR (parallel beams) with (PS) and without (empty) a 50 μm polystyrene sample. The absorption features compare well with the transmittance obtained in conventional FTIR (dotted), and show that cross-comb beating does not compromise the main features but rather contributes a smooth background.

the form of the beat spectrum in the 20–40 THz region persists. An example is shown in Fig. 2b where the red curve[1] corresponds to an angle of 0.4° between both beams, from which we calculate that the foci are separated by 125 μm. A drawback of this alignment is that the collimated mid-infrared beams are no longer exactly parallel. This means that interference stripes across their cross-sectional overlap region diminish the interferogram amplitude. Yet the observed signal reduction in the 20–40 THz region (red vs black in Fig. 2b) seems quite acceptable, especially when we realize that a sizable reduction probably stems from the suppression of background beats which are expected also in this frequency region (Appendix A). A smaller angle of 0.2° or 0.1° would theoretically fully suffice to suppress background in a future, refined setup where the visible beams are spatially filtered to approach TEM$_{00}$ mode distribution, and therefore, the nominal beam widths are no larger than about 12 μm (FWHM) in the crystal. A second way to eliminate non-harmonic modes is offered by phase matching [14]. While phase matching determines that DFG within each beam results in a forward-centered mid-infrared cone (approximately 80° FWHM in our setup), the cross-beam mid-infrared modes emerge in a cone that is directed about 80° off-axis, and thus could be partially eliminated by a suitable beam stop. While not explicitly mentioned this mechanism could have provided nearly artifact-free spectra in a recent spectral analysis using mechanical delay [16].

In summary, we have demonstrated a compact comb-FTS which uses a single nonlinear crystal. Alignment of this comb-FTS requires a mere single-mirror adjustment of the visible beams. These can serve to pilot the mid-infrared beams even over large distance. A compact comb-FTS can be as broad banded as allowed by constraints of the nonlinear crystal or the detector because it avoids the dielectric beam combiner used in most classical FTIR and comb-FTS instruments. The particular advantages

are that no broad-band transmitting material needs to be designated and processed, no compensation of induced dispersion has to be implemented, and no worries arise of how to suppress optical effects due to the second dielectric surface, especially multiple reflections both for the interferometer and the pilot beams. The essential part of the spectrometer—a nonlinear crystal between two lenses—could be placed remotely from the lasers and also from the detector. It could be placed next to a hard-to-access object, for example, near a plasma vessel or inside a cryostat. The visible input beams could be guided in glass fibers. Also, the lasers could be conveniently packaged in a compact, pre-aligned emitter module. This could be used with an independent, compact receiver module for remote detection and imaging. Applications in environmental monitoring, in standoff chemical recognition, and in tele-detection of chemicals are suggested.

Acknowledgement

Appendix A

A.1. Cross-comb frequencies

To find all frequency components of the beat spectrum of our experiment we write for the field amplitudes E_1 and E_2 of both visible beams [17]

$$E_1(t) = \sum_{k=K}^{L} E_{1,k} \cos(2\pi(f_{1,0} + kf_r)t + \varphi_{1,k})$$

$$E_2(t) = \sum_{k=K}^{L} E_{2,k} \cos(2\pi(f_{2,0} + k(f_r + \Delta))t + \varphi_{2,k})$$

where k is a large ($\approx 10^6$–10^7) integer designating the mode number of each frequency comb component with amplitude $E_{1,k}$ and $E_{2,k}$, and phase $\varphi_{1,k}$ and $\varphi_{2,k}$, respectively. Note the existence of a non-zero carrier-envelope offset (ceo) frequency, $f_{1,0}$ and $f_{2,0}$ (both $<f_r$) in both comb spectra. It is just these terms which can give rise to background beats.

As long as two mid-infrared beams arise from separate difference-frequency generators as in Refs. [1–7,9], the result is two mid-infrared combs, with $n \approx 10^5$–10^6,

$$E_1(t) = \sum_{n=M}^{N} E_{1,n} \cos(2\pi n f_r t + \varphi_{1,n})$$

$$E_2(t) = \sum_{n=M}^{N} E_{2,n} \cos(2\pi n(f_r + \Delta)t + \varphi_{2,n})$$

which are harmonic combs because the ceo frequencies cancel out exactly. When superimposing these beams in a FTS without moving part, the desired harmonic beat comb arises

---
[1] For interpretation to color in Fig. 2, the reader is referred to the web version of this article.

$$E_b(t) \propto \sum_{n=M}^{N} E_{1,n} E_{2,n} \cos(2\pi n \Delta t + \varphi_{1,n} - \varphi_{2,n}).$$

When however both visible beams are superimposed in a single difference-frequency generator extra infrared modes are generated in addition

$$E_3(t) \propto \sum_{k'=K}^{L} \sum_{k=K}^{L} E_{2,k} E_{1,k'} \cos(2\pi(f_{2,0} + k(f_r + \Delta)t + \varphi_{2,k})$$
$$- 2\pi(f_{1,0} + k'f_r)t + \varphi_{1,k'})$$

$$E_4(t) \propto \sum_{k'=K}^{L} \sum_{k=K}^{L} E_{1,k} E_{2,k'} \cos(2\pi(f_{1,0} + k(f_r)t + \varphi_{1,k})$$
$$- 2\pi(f_{2,0} + k'(f_r + \Delta))t + \varphi_{2,k'})$$

with cross-comb frequencies

$$f_{2,0} - f_{1,0} + (k - k')f_r - k'\Delta$$
$$f_{1,0} - f_{2,0} + (k - k')f_r - k\Delta$$

where $N < k - k' < M$. These are offset from the harmonic comb frequencies nf_r by

$$f_{1,0} - f_{2,0} - k\Delta$$
$$f_{2,0} - f_{1,0} - k\Delta.$$

In the practical example of our experiment the range of visible modes extends between 750 and 850 nm (FWHM), equiv. to 353 and 400 THz, so $K \approx 2{,}800{,}000$ and $L \approx 3{,}200{,}000$. The mid-infrared region 20–40 THz corresponds to $N \approx 160{,}000$ and $M \approx 320{,}000$. Thus two combs of extra beats stretch over $(K-L)\Delta \approx 400{,}000 \times 83.4$ Hz $= 33$ MHz wide bands centered at the difference in ceo frequencies. The latter is unknown and may not stay constant with time.

References

[1] D. van der Weide, F. Keilmann, Coherent Periodically Pulsed Radiation Spectrometer, Patent US5748309 (1998) filed 20 October 1994.

[2] D. van der Weide, F. Keilmann, Picosecond dual-source interferometer extending Fourier-transform spectrometer to microwave range, IEEE MTT-S Digest (1996) 1731.

[3] D. van der Weide, J. Murakowski, F. Keilmann, Gas-absorption spectroscopy with electronic Terahertz techniques, IEEE Transactions on Microwave Theory and Techniques 48 (2000) 740.

[4] F. Keilmann, C. Gohle, R. Holzwarth, Time-domain mid-infrared frequency-comb spectrometer, Optics Letters 29 (2004) 1542.

[5] A. Schliesser et al., Frequency-comb infrared spectrometer for rapid, remote chemical sensing, Optics Express 13 (2005) 9029.

[6] F. Keilmann et al., Verfahren und Vorrichtung zur Abtastung von sich periodisch wiederholenden Ereignissen, Patent DE102005050151 (2006) filed 19 October 2005.

[7] M. Brehm, A. Schliesser, F. Keilmann, Spectroscopic near-field microscopy using frequency combs in the mid-infrared, Optics Express 14 (2006) 11222.

[8] S. Schiller, Spectrometry with frequency combs, Optics Letters 27 (2002) 766.

[9] I. Coddington, W.C. Swann, N.R. Newbury, Coherent, multi-heterodyne spectroscopy using stabilized optical frequency combs, Physical Review Letters 100 (2007), 13901, 13902, 13904.

[10] T. Yasui et al., Terahertz frequency comb by multifrequency heterodyning photoconductive detection for high-accuracy, high-resolution tetrahertz spectroscopy, Applied Phys. Letters 88 (2006), 241101, 241103, 241104.

[11] T. Yasui, E. Saneyoshi, T. Araki, Asynchronous optical sampling terahertz time-domain spectroscopy for ultrahigh spectral resolution and rapid data acquisition, Applied Physics Letters 87 (2005), 61101, 61103.

[12] A. Bartels et al., High-resolution THz spectrometer with kHz scan rates, Optics Express 14 (2006) 430.

[13] A. Bartels et al., Ultrafast time-domain spectroscopy based on high-speed asynchronuous optical sampling, Review of Scientific Instruments 78 (2007) 351071.

[14] M. Joffre et al., Femtosecond diffractive Fourier-transform infrared interferometer, Optics Letters 21 (1996) 964.

[15] J. Strong, G.A. Vanasse, Lamellar grating far-infrared interferometer, Journal of the Optical Society of America 50 (1960) 113.

[16] T. Zentgraf et al., Ultrabroadband 50–130 THz pulses generated via phase-matched difference frequency mixing in LiTiO$_3$, Optics Express 15 (2007) 5775.

[17] T. Udem, R. Holzwarth, T.W. Hänsch, Optical Frequency Metrology, Nature 416 (2002) 233.